The Role of Substrate Stiffness on the Dynamics of Actin Rich Structures and Cell Behavior

Yukai Zeng
July 24, 2013

Department of Mechanical Engineering
Carnegie Mellon University
5000 Forbes Avenue
Pittsburgh, PA 15213

Thesis Committee:
Carmel Majidi
Keng-Hwee Chiam
Yu-Li Wang
Philip R. LeDuc

Carnegie Mellon University

CARNEGIE INSTITUTE OF TECHNOLOGY

THESIS

SUBMITTED IN PARTIAL FULFILLMENT OF THE REQUIREMENTS

FOR THE DEGREE OF Doctor of Philosophy

TITLE The Role of Substrate Stiffness on the Dynamics of Actin Rich Structures and Cell Behavior

PRESENTED BY Yukai Zeng

ACCEPTED BY THE DEPARTMENT OF

Mechanical Engineering

_____ _____
ADVISOR, MAJOR PROFESSOR DATE

_____ _____
DEPARTMENT HEAD DATE

APPROVED BY THE COLLEGE COUNCIL

_____ _____
DEAN DATE

The Role of Substrate Stiffness on the Dynamics of Actin Rich Structures and Cell Behavior

Submitted in partial fulfillment of the requirements for

the degree of

Doctor of Philosophy

in

Mechanical Engineering

Yukai Zeng

B.S., Bioengineering, Nanyang Technological University, Singapore

Carnegie Mellon University

Pittsburgh, PA

August, 2013

Acknowledgments

I would like to thank Hiong Yap for giving me my first taste of research back in 2006 during my undergraduate years. His true impact on my life and career was not felt by me until many years later: he truly did start it all. My appreciation to Keng Hwee for giving me my first shot at a research career, as well as the constant much needed guidance and supervision. A big thank you to Phil for his supervision and brainstorming techniques as well as ideas: He has been so kind and motivation since the beginning. I would also like to thank Cheng Gee for her guidance and for allowing me the freedom to work her lab, and to Evelyn and her post-doc Sang Joon for the initial lab training, and my thesis committee at Carnegie Mellon for their time, guidance and comments. I am extremely grateful to all of them for my research development.

My special thanks go to Robert for being my mentor and friend during my Ph.D. journey, as well as to Si Yen, Elmer and Shu Ying for helping me get used to my surroundings when I first got to Pittsburgh. My appreciation goes to May and Yan Ru for their help during this time as well. I managed to get my first research work breakthrough because of the hard work, insight and dedication of Tanny: Many thanks to her.

I would like to thank my colleagues at the LeDuc lab in the mechanical engineering department at Carnegie Mellon for their insights and critical discussions, they were all really engaging. My appreciation goes to Chris and Ginny of the mechanical engineering department for helping my patiently and thoroughly with all my queries that I had (and I had a lot).

I would like to thank A*STAR Singapore for their funding and support throughout my Ph.D. journey and beyond. Last but not least, my family has always been there for me: They have my sincerest of gratitude.

Keywords: Cell-substrate Interactions; Stiffness; Circular Dorsal Ruffles; NIH-3T3 fibroblasts; Actin Dynamics; Motility; Lamellipodia; Poly(dimethylsiloxane); Polyacrylamide; Dynamic Substrate Stiffness; Morphology; Mesenchymal Stem Cells

Abstract

Cell-substrate interactions influence various cellular processes such as morphology, motility, proliferation and differentiation. Actin dynamics within cells have been shown to be influenced by substrate stiffness, as NIH 3T3 fibroblasts grown on stiffer substrates tend to exhibit more prominent actin stress fiber formation. Circular dorsal ruffles (CDRs) are transient actin-rich ring-like structures within cells, induced by various growth factors, such as the platelet-derived growth factor (PDGF). CDRs grow and shrink in size after cells are stimulated with PDGF, eventually disappearing ten of minutes after stimulation. As substrate stiffness affect actin structures and cell motility, and CDRs are actin structures which have been previously linked to cell motility and macropinocytosis, the role of substrate stiffness on the properties of CDRs in NIH 3T3 fibroblasts and how they proceed to affect cell behavior is investigated. Cells were seeded on Poly-dimethylsiloxane (PDMS) substrates of various stiffnesses and stimulated with PDGF to induce CDR formation. It was found that an increase in substrate stiffness increases the lifetime of CDRs, but did not affect their size. A mathematical model of the signaling pathways involved in CDR formation is developed to provide insight into this lifetime and size dependence, and is linked to substrate stiffness via Rac-Rho antagonism. CDR formation did not affect the motility of cells seeded on 10 kPa stiff substrates, but is shown to increase localized lamellipodia formation in the cell via the diffusion of actin from the CDRs to the lamellipodia. To further probe the influence of cell-substrate interactions on cell behavior and actin dynamics, a two dimensional system which introduces a dynamically changing, reversible and localized substrate stiffness environment is constructed. Cells are seeded on top of thin PDMS nano-membranes, and are capable of feeling through the thin layer, experiencing the stiffness of the polyacrylamide substrates below the nano-membrane. The membranes are carefully re-transplanted on top of other polyacrylamide substrates with differing stiffnesses. This reversible dynamic stiffness system is a novel approach which would help in the investigation of the influence of reversible dynamic stiffness environments on cell morphology, motility, proliferation and differentiation in various cells types.

Table of Contents

List of Figures

Chapter 1

Introduction

The importance of cell-substrate interactions is evident in many cellular processes such as cell morphology, motility, proliferation and differentiation. An important property of the extracellular environment surrounding cells is the stiffness of the underlying substrate of cells in 2-dimensions (2-D), which has been shown to affect cell spread area and cytoskeletal structures (1), in particular, the actin rich structures such as stress fibers. Moreover, cell motility has been shown to be guided by the stiffness of the underlying substrates (2), highlighting the role that extracellular stiffness plays in the movement of normal and pathological cells, such as cancerous cells involved in metastasis. This is due to the ability of cells to sense, respond, and generate mechanical forces in response to substrate stiffness.

Cells are able to sense their environment through various cell-environment protein connections, such as integrin complexes linking the extracellular environment to the internal structure of the cell, and cadherins, which link cells to one another. The process by which cells integrate their external mechanical signals into a biochemical response, which bring about intracellular changes such as cytoskeletal reorganization and differential protein expression, is

known as mechanotransduction (3, 4). Even the process of stem cell differentiation is known to be controlled by substrate stiffness: Mesenchymal stem cells (MSCs) have been shown to differentiate into various lineages based on the elasticity of their underlying substrate (5). On softer substrates mimicking brain tissue, MSCs have been shown to differentiate into neural cells. On stiffer substrates, MSCs differentiate into osteoblasts, which are found in bone tissue. Therefore, how substrate stiffness affects cell behavior in various cell types (normal and pathological) continues to be an intensive area of study.

In this chapter, we look in detail at how cells interact with their environment. Specifically, how protein connections such as integrins and cadherins link the extracellular environment and other cells respectively to the internal structure of the cell is discussed. A major component of the internal cell structure is the cytoskeleton, which is composed in part by the protein actin. The various actin-rich structures in cells are looked at, as well as how cell behavior can be controlled by tuning the stiffness of their extracellular environment. Lastly, we focus on the structure and functions of the actin-rich intracellular structure known as the circular dorsal ruffle (CDR), which has been implicated in cell motility and macropinocytosis.

1.1. Interactions between Cells and their Environment

Cells in various tissues of the body are exposed to a wide variety of extracellular environmental stiffnesses. **Fig. 1.1** illustrates the different environmental stiffnesses for cells in various tissues. This figure is referenced from Butcher et al. (6). The figure shows the elastic modulus of the extracellular tissue environment that various cell types in the human body are

exposed to, increasing in stiffness from the left to the right of the figure. The various cell niche environments include that of the lung, breast, skeletal muscle and bone in order of increasing stiffness. It can be seen that the environmental stiffness in which cells are exposed to in the body vary by many orders of magnitude, from the Pascal to the Giga-Pascal range. Consequently, cells within the body are exposed to a large variation in extracellular environmental stiffness. For example, the stiffness of the brain in which neural cells reside in is in the order of Pascals, which is four orders of magnitude softer than the environment in which osteoblasts are found in the body. Since cell growth, survival and differentiation are supported by the interactions between the cells and their environment (6), understanding how cells interact with their environment is critical in elucidating how environmental cues bring about changes in cell behavior.

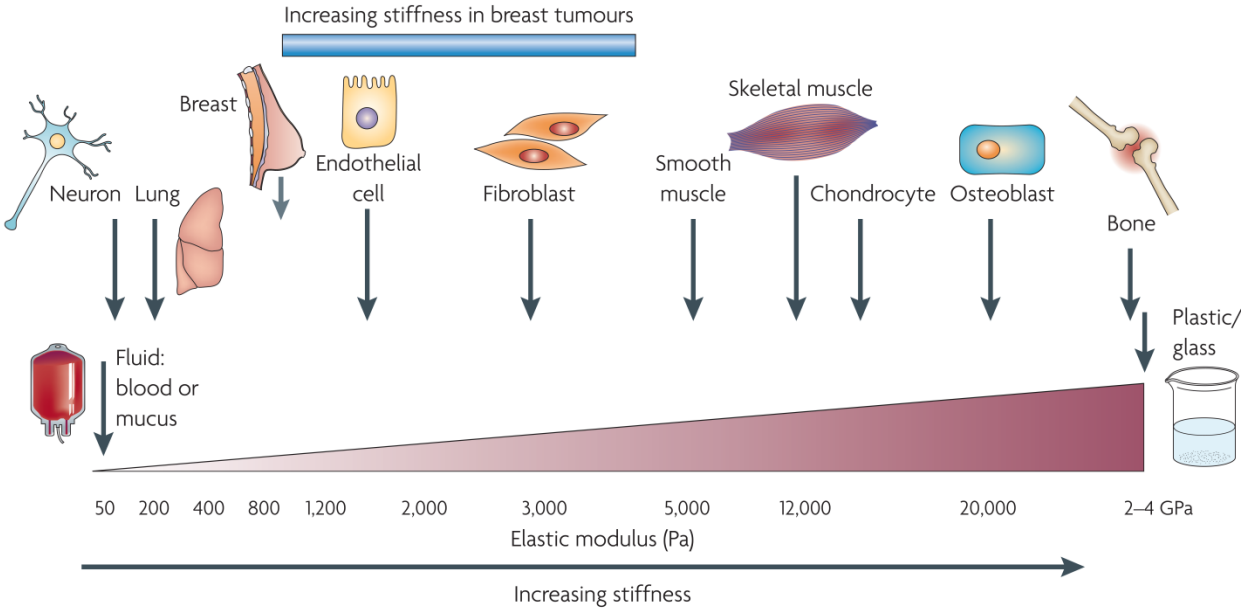

FIGURE 1.1: Different environment stiffnesses for cells in various tissues. Cells in different parts of the body, such as in the muscle, bone and brain, are exposed to mechanical forces through the connections between them and the environment as well as to other cells in their surroundings. The stiffness of the mechanical

environment creates a niche in which each cell in different parts of the body resides. The stiffness of these environments can vary greatly. For example, brain tissue is much softer than bone tissue and neural cell survival and differentiation is determined by a very compliant mechanical environment. The differentiation of osteoblasts is determined by a relatively stiffer matrix around the cells, as compared to those found in muscles and in brain tissue. These examples show the important link between tissue phenotype and matrix rigidity. Figure referenced from (6).

Cells interact with the surrounding extracellular matrix (ECM) by moving through, modifying and at times degrading it. In turn, forces can be transmitted from the ECM to the cell interior via mechanotransduction. These forces are exerted mainly via transmembrane cell adhesion proteins that span through the entire cell membrane and consist of separate domains which attach to the ECM and to cytosolic proteins and structures within the cell. An example of these transmembrane cell adhesion proteins is the integrins, which is the major receptor on mammalian cells for binding most ECM to the cell. Consisting of two major subunits, the α and β subunits, the large family of homologous integrins exist in activated and inactivated configurations, and allows the transmission of signals in both directions across the cell membrane.

A schematic of how integrin connects the ECM to the cell interior is shown in **Fig. 1.2**. Activated integrin molecules which span through the entire cell membrane have their head component attached to extracellular ECM proteins. Examples of these ECM proteins include fibronectin and collagen. The cytosolic tail components of the integrin molecules attach to intracellular anchor proteins within the cell cytosol, such as vinculin and talin, which is bounded to other components of the cell such as actin filaments. As such, the ECM is structurally linked to the internal structure of the cell via the integrins. This figure is referenced from

Alberts et al. (7). Examples in which integrins are of particular importance are in the mediation of epithelial cell interactions with the underlying basal lamina, and in connective tissues.

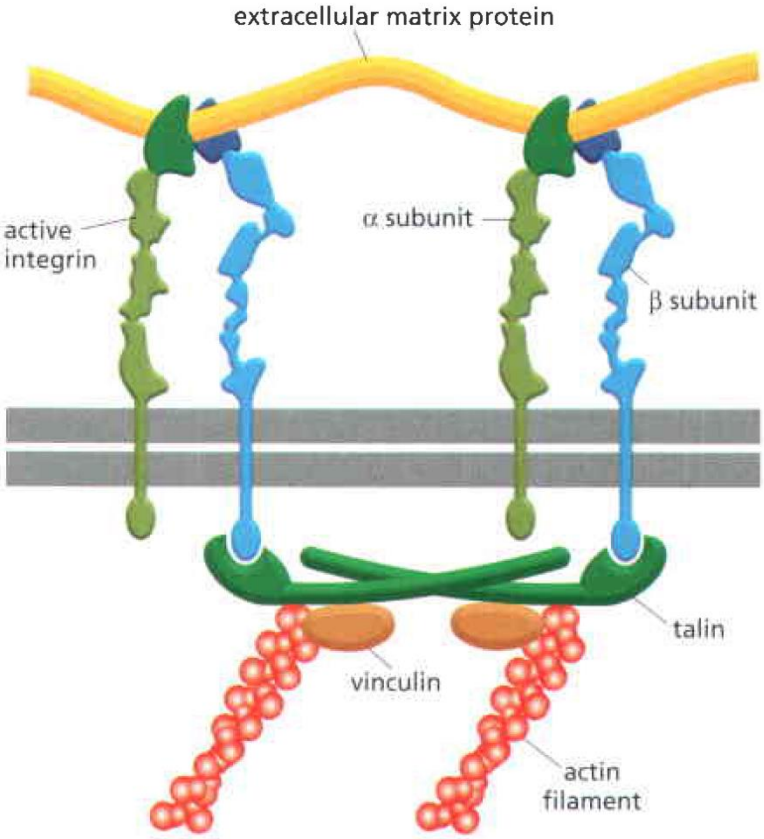

FIGURE 1.2: Schematic of molecular linkages between the ECM and the cell cytoskeleton. Activated cell membrane proteins such as integrin molecules have their heads attached to ECM proteins such as fibronectin. The cytosolic tail components of the integrin molecules attach to intracellular anchor proteins such as talin and vinculin, which in turn binds to the cytoskeletal components of the cell, such as actin filaments. Referenced from Alberts et al. (7).

1.2. Actin-rich Structures Within Mammalian Cells

The cytoskeleton of the cell is important in maintaining cellular shape and structure. Recent studies have shown the importance of the cytoskeleton in the process of mechanotransduction (3, 4). The cytoskeleton is highly dynamic and comprises of three main cytoskeletal proteins: Microtubules, intermediate filaments and actin microfilaments.

The actin globular proteins (G-actin) are the monomeric components of the filamentous actin (F-actin) structures which constitute the cytoskeleton. This polymerization process is made possible by the addition of ATP, with other nucleating factors and actin binding proteins (8). The ability of F-actin structures to polymerize and depolymerize into their constituent G-actin monomers makes the microfilaments a dynamic and responsive cytoskeletal structure within the cell. This rapid polymerization and depolymerization of F-actin filaments is known as thread milling. When polymerized, the F-actin filaments have a diameter of about 6 nm and are structurally able to resist tension but not compression, as compared to the microtubules, which are able to resist compression. These F-actin filaments are responsible for maintaining cell shape within the cell and have been linked to numerous important cellular processes. Being a highly conserved cytoskeletal protein, actin has four major functions: Cell motility, contraction of muscles via myosin in muscle cells, intracellular cargo transport and signal transduction within cells (9, 10).

The structural integrity of F-actin filamentous macrostructures enables them to participate in various cellular processes such as cell motility and proliferation (11), depending on which filamentous macrostructures the F-actin filaments form. The two main groups of F-actin

macrostructures which can form within mammalian cells are the cross-linked network and the bundled network. These two different network structures are formed by the presence of distinct nucleating proteins, whereby in the presence of the proteins, formins, result in F-actin bundles and the actin-related proteins (ARP) complexes result in web-like cross-linked structures (8). Depending on the cell processes that are involved, the rapid association and dissociation of the filaments allows for F-actin structures to form either cross-linked structures or bundles rapidly and dynamically at different parts in the cell.

In **Fig. 1.3**, an illustration of how the components of an actin filament changes dynamically via actin nucleation and turnover is shown. This figure is referenced from (12). The kinetics of actin polymerization are favored at certain ends of a filament more than others. The more favourable the kinetic rates in the figure, the thicker the arrows shown. Polymerization is greatly favored at one end (denoted the plus end) of the filament, while depolymerization is favoured at the other (the minus end). Actin adenosine 5'-triphosphatase (ATPase) activity is greatly increased when incorporated into the actin filament, and the spontaneous hydrolysis of ATP and phosphate dissociation causes the destabilization of filaments, increasing the likelihood of them being acted upon by severing proteins, such as the members of the actin depolymerizing factor (ADF)/cofilin family. Adenosine 5'-diphosphatase-actin (ADP-actin) which have been dissociated undergo an exchange of nucleotide. Profilin, an actin binding protein, aids in this exchange and interacts with formins for filament assembly regulation. The binding of capping proteins such as gelsolin at the plus end of the filament prevents them from elongating from the plus end. This dynamic change in actin filament components is known as treadmilling, as the overall length of the actin filament might not change, although components are being added at one end of the filament and removed from the other.

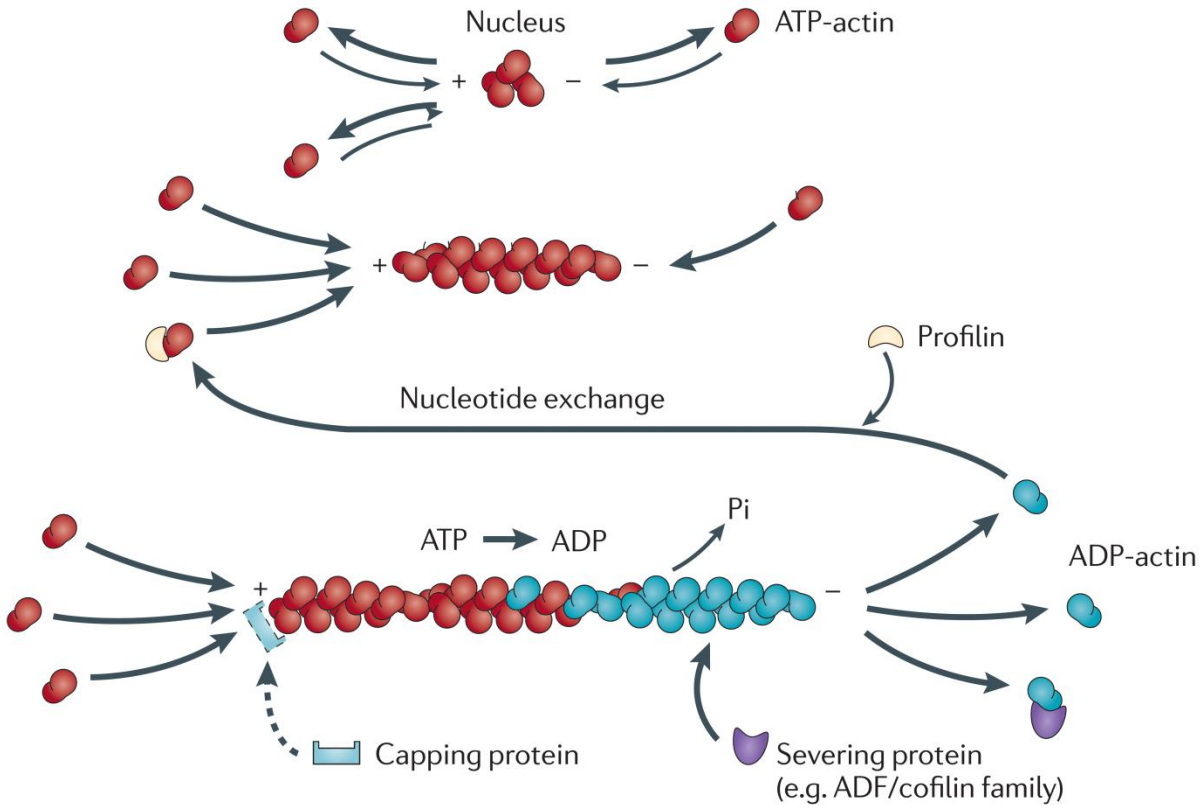

FIGURE 1.3: Schematic of actin filament tread milling arising from nucleation and turnover. Actin polymerization kinetics are favoured at some ends of the filament more than others (denoted by the thick and thin arrows). Polymerization is greatly favored at one end (denoted the plus end) of the filament, while depolymerization is favoured at the other (the minus end). Upon incorporation into the filaments, actin ATPase activity is greatly increased. The spontaneous hydrolysis of ATP and phosphate dissociation causes the destabilization of filaments and increases the chance of it being acted upon by severing proteins, which include the members of the ADF/cofilin family. ADP-actin which has been dissociated undergo an exchange of nucleotide which is aided by profilin, an actin binding protein which in turn interacts with formins to regulate filament assembly. Filament elongation at the plus end can be suppressed by the binding of capping proteins such as gelsolin. Referenced from (12).

In addition to the formation of individual actin filaments mentioned in **Fig. 1.3**, how the actin filaments are nucleated influences the large-scale filament organization within cells. Examples of how actin filaments are nucleated are shown in **Fig. 1.4**. Actin filaments in mammalian cells are organized into two main types of networks: the bundled and the web-like or gel-like networks. The formation of these networks is determined by the associated actin-binding and linking proteins between the actin filaments, which are shown in **Fig. 1.4**. This figure is referenced from (7).

Many structures within the cell cytoskeleton require the bundling of parallel actin filaments together to form parallel bundles. This is carried out by actin filament binding proteins such as fimbrin and α-actinin, while the actin nucleation is supported by formins as shown in **Fig. 1.4**. The formins are a family of dimeric proteins which bind to G-actin and associate with the plus ends of actin filaments, allowing the rapid binding of new G-actin subunits to the plus end and the subsequent elongation of the actin filaments. This allows other actin bundling proteins such as fimbrin and α-actinin to bind and link adjacent actin filaments in a parallel manner (**Fig. 1.4**), causing them to form parallel bundles. The difference between the different actin bundling proteins is the spacing in between the parallel actin filaments which are linked. For example, fimbrins are smaller molecules as compared to α-actinin, causing parallel actin filaments to bind much closer to one another than that in α-actinin. The importance of this difference in parallel actin filament bundle spacing is that this allows the bundled networks to exclude certain proteins such as myosin from entering within their structure. Myosins, when linked to adjacent actin filaments, bring about the contraction and movement of actin filaments, thus forming contractile bundles in the bundled actin networks. As fimbrin causes the formation of an actin bundled network in which the spacing in between filaments are too small for myosin

to enter the network, bundled actin filament networks formed by fimbrin cannot become contractile bundles, as opposed to that of α-actinin, which allows myosin to enter the spacing in between the actin filaments.

As opposed to formin, fimbrin and α-actinin, which have stiff and straight connections between their two actin filaments in which they bind to and causing the actin filaments to align in parallel bundles (**Fig. 1.4**), another group of actin nucleating proteins causes the cross-linking of actin filaments. These are used to form other actin-rich cytoskeletal structures within the cell, such as the lamellipodia, which would be discussed later.

An example of a group of major actin filament cross-linking protein is the filamins. Filamins are long and bent actin-crosslinking proteins which have two actin-binding domains, enabling the formation of 3-dimensional (3-D) actin gels. Filamins bind two adjacent actin filaments by linking them together at roughly right angles, as shown in **Fig. 1.4**. As opposed to linking actin filaments at right angles, another group of actin nucleating proteins, the ARP complexes, bring about actin nucleation and actin web formation by linking adjacent actin filaments at 70° angles. Consisting of two subunits, the Arp 2 and Arp 3 components, the ARP complex nucleates actin filaments by binding to the side of an actin filament (**Fig. 1.4**). An activating factor causes the Arp 2 and Arp 3 complexes to come together to form the active ARP complex, which resembles the plus end of an actin filament, enabling free G-actin subunits to bind to them. The new actin filament forms at a 70° angle with respect to the existing actin filament this way.

In addition to the actin filament bundling and cross-linking proteins, there are some actin-associating proteins which link the web of actin filaments to other structures, such as the plasma membrane. A large portion of the actin cytoskeleton network found in cells is found at the cell

cortex, just underneath the cell membrane. A family of proteins known as the ERM proteins (named as such due to the first three members of the family being ezrin, radixin and moesin) binds the actin cytoskeleton network at the cell cortex found underneath the cell membrane, to the cell membrane. These proteins achieve this by the binding of the C-terminal of an ERM protein to the sides of actin filaments, while the N-terminal of the ERM protein binds to transmembrane proteins found in the cell membrane as shown in **Fig. 1.4**. Another example is the protein spectrin is concentrated just beneath the cell membrane in red blood cells and links the cross-linked network of actin filaments to the cell membrane (**Fig. 1.4**). This enables the cell membrane to increase its overall mechanical stiffness by linking it to the underlying actin cortex, enabling the cells to maintain their structural integrity.

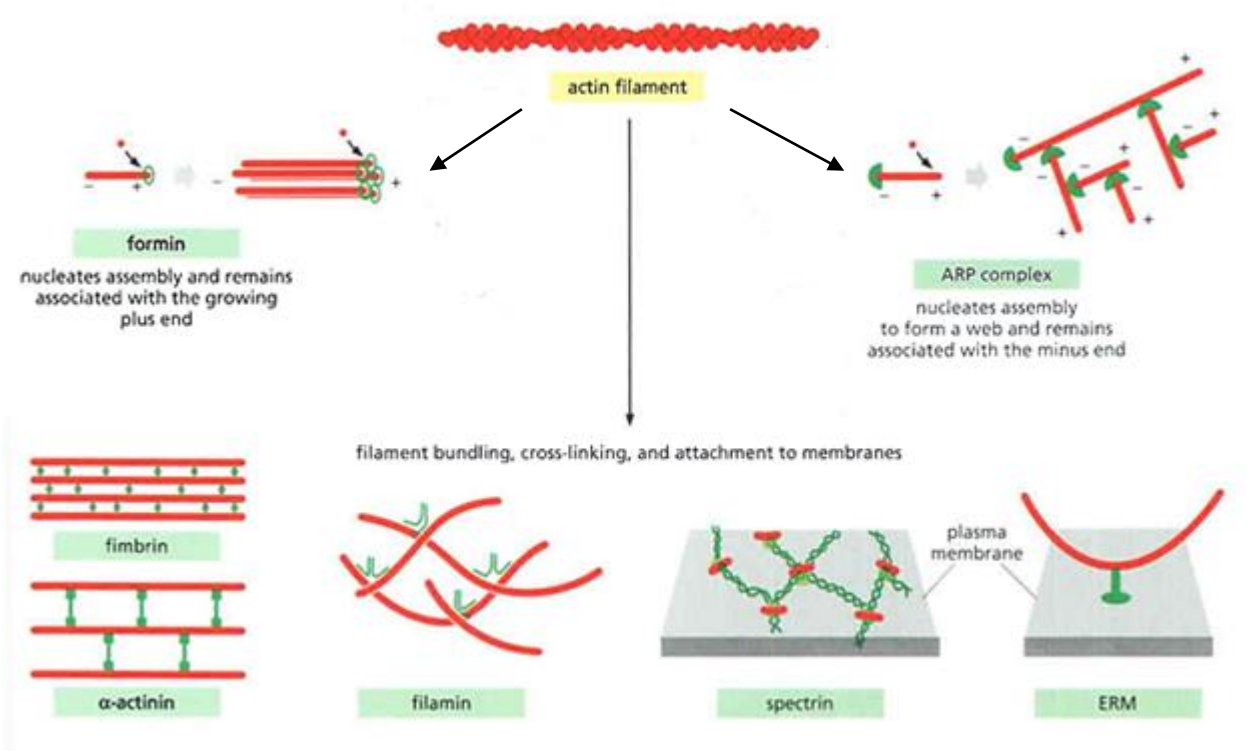

FIGURE 1.4: Schematic of the major actin-binding proteins and their roles in forming the various forms of actin filament networks in the cell. Referenced from (7).

As mentioned in **Fig. 1.4**, many of the major actin-rich structures that form within cells can be classified into cross-linked structures or bundled structures. Examples of cross-linked F-actin structures are CDRs, lamellipodia, podosomes and invadopodia (13). Examples of bundled F-actin structures include stress fibers and filopodia (14, 15). Each of these individual structures plays a specific role within the cell. The G-actin monomeric components of these structures can be recycled and rapidly transported within the cells, resulting in the assembly and disassembly of these various structures. This mechanism is known to be governed by the Rac-Rho protein antagonistic pathways (14), which allows G-actin monomers to be cycled between cross-linked structures and bundled structures within the cell.

Lamellipodia are flat, sheet-like protrusions normally found at the leading edge of a cell. These lamellipodia protrusions enable the cell to extend its leading edge forward on a flat 2-D substrate, allowing it to explore its surrounding environment and crawl forward (16). This forward protrusion of the cell is coupled with the retraction of the cell membrane at the rear to enable to cell to move forward. The inability of a cell to form lamellipodia protrusions would render them unable to move to explore their surrounding environment. As such, the lamellipodia of pathological cells such as cancer cells have been targeted in possible therapeutic treatments (17).

Podosomes are cross-linked F-actin structures which appear as dot-shaped actin patches on the ventral surface of the cell membrane when cells are seeded on 2-D substrates. The size of these podosomes range from 1-2 μm in diameter and 200-400 nm in height (18, 19). Each

podosome consists of a core of cross-linked F-actin which is enclosed by F-actin accessory proteins such as vinculin and talin (20, 21). Although little is known about the role of podosomes in most cells, they have been implicated in the adhesion of monocytes and directed chemotaxis (22).

Cells derived from tumors that are grown on 2-D substrates extrude F-actin rich invadopodia structures into the ventral surface of the surrounding matrix. Much like the podosome structures, invadopodia result in degradation of the substrate at the areas in which they form (23). The invadopodia can reach a width of 8 μm wide and 2 μm deep, and degrade the underlying matrix through the secretion of metalloproteinases (24).

Stress fibers are structures formed from bundled F-actin filaments (14). These filaments are loosely packed by proteins such as α-actinin and can be found in muscles, which allow for myosin to enter the structure and bring about contraction of the fibers by the sliding of adjacent F-actin fibers relative to one another in a stress fiber. Prominent stress fiber formation occurs in cells grown on stiff 2-D substrates as well, and these stress fibers are similarly contractile in nature.

Filopodia are tightly bundled F-actin structures formed by proteins such as fimbrin. In these tightly bundled filaments, myosin cannot enter the structure and therefore these filaments are not contractile in nature (14). Under the microscope, filopodia have been described as spikey protrusions which the cell uses to explore its environment, much like the lamellipodia. The difference between lamellipodia and filopodia protrusions is that the lamellipodia protrusions consist of cross-linked F-actin structures which are broad and sheet-like, while the filopodia protrusions consist of tightly bundled F-actin filaments which assume a spikey like appearance.

A figure illustrating the localization of various actin-rich structures found in mammalian cells is shown in **Fig. 1.5**. This figure is referenced from (26). In **Fig. 1.5A,** the top view of an upward migrating cell which is attached to another cell to its right is shown, along with the localization of various actin-rich structures within the cell. For example, at the leading edge, actin-rich filopodia and lamellipodia can be found, while cortical actin is found around the entire edge of the cell. Further away from the cell edge, actin-rich podosomes can be found, as well as stress fibers, which span across a large portion of the cell. Actin is also associated with internal structures of the cell, including the golgi apparatus and the nucleus. **Fig. 1.5B** shows the side view of a migrating cell, illustrating the localization of various actin-rich structures with respect to the face of the cell which is in contact with the underlying substratum. Actin-rich ruffles in cells are located on the dorsal surface, away from the underlying substratum. Also, peripheral and dorsal ruffles are distinguished as two different structures. On the ventral surface of the cell in contact with the substratum, actin-rich podosomes and invadopodia are found. Lamellipodia are adhered to the substratum at the ventral surface of the cell.

So far, the major F-actin structures composed of cross-linked filaments and bundled filaments have been summarized, and it has been shown that two of the major antagonistic proteins governing the formation of these structures are the Rac and Rho GTPases (14, 25). The Rac GTPases are responsible for the formation of cross-linked structures such as the CDRs and the Rho GRPases participate in the formation of bundled structures such as the stress fibers in a cell. This Rac-Rho antagonism plays a major role in this thesis with regards to how F-actin rich structures are formed within the cell, mainly, CDRs and stress fibers.

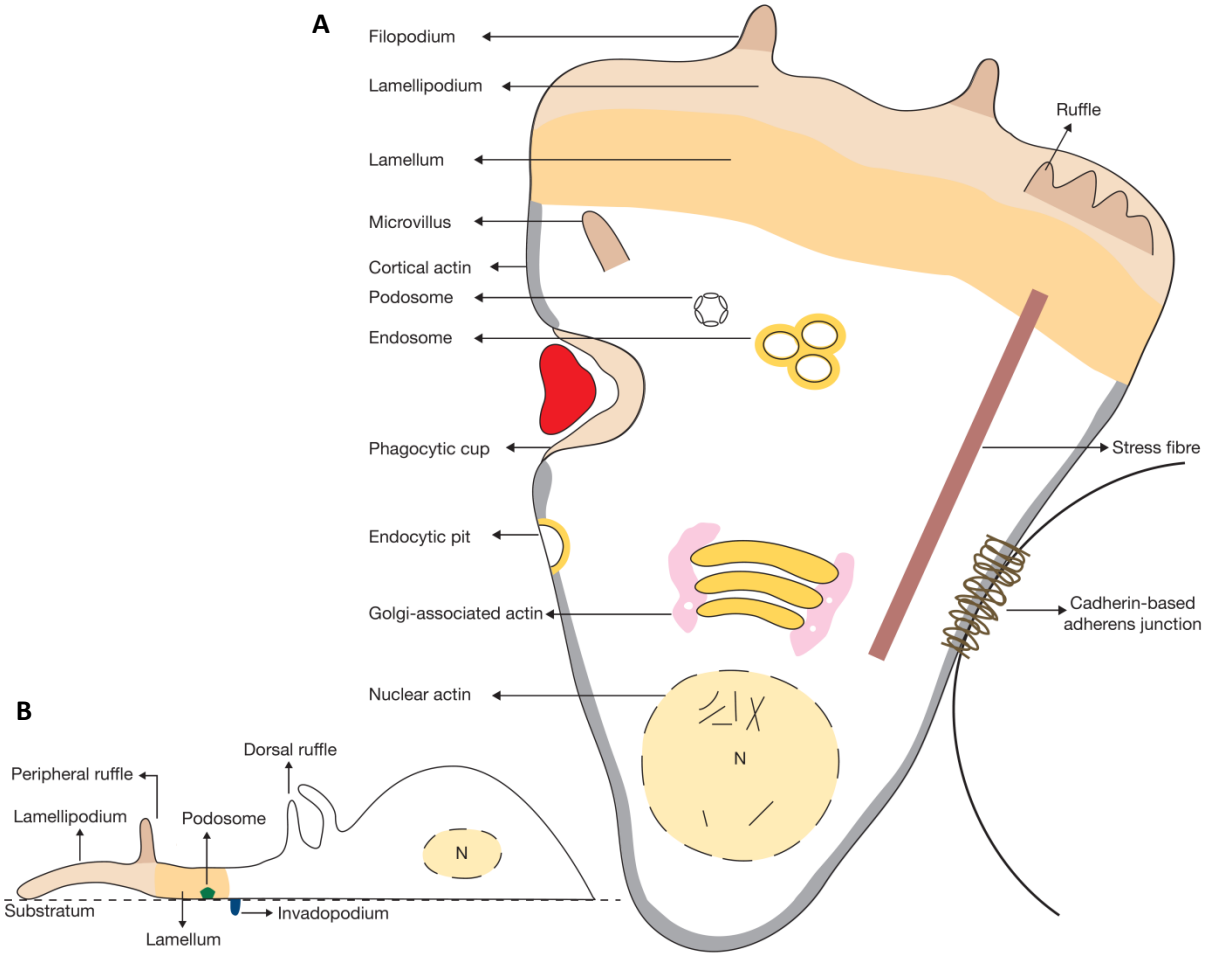

FIGURE 1.5: Various actin-rich structures found within cells. (A) A top view of a cell which is migrating upwards, attached to another cell to its right, exhibiting various actin-rich structures. Some examples include the actin-rich filopodium and lamellipodium structures are found at the leading edge of the cell, and the stress fibers which span through a large part of the cell. (B) A side view of a cell, showing the proximity and localization of various actin-rich structures. For example, ruffles are structures which are found on the dorsal side of the cell while podosome and invadopodia are found on the ventral side of the cell. Peripheral ruffles and dorsal ruffles are also two distinct structures, while lamellipodia are in contact with the substratum. N denotes the nucleus. Figure referenced from (26).

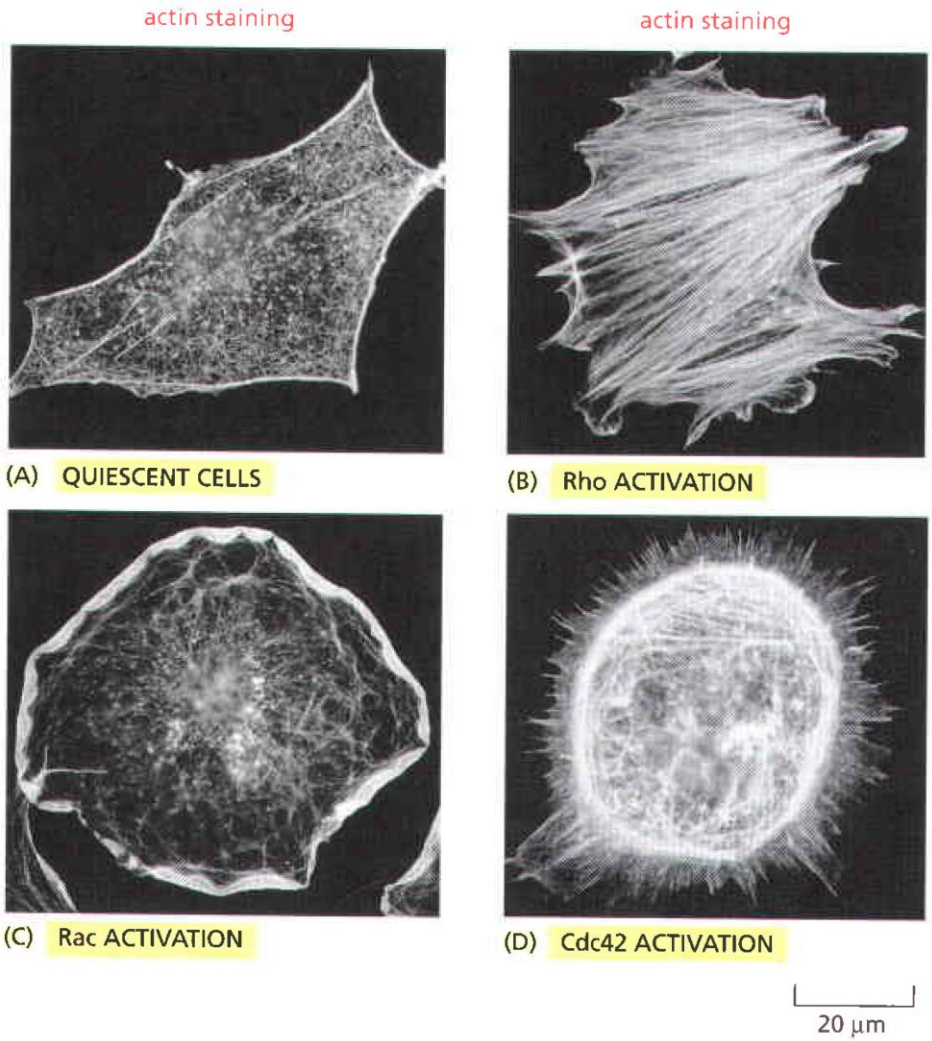

FIGURE 1.6: The effects of Rac, Rho, and Cdc42 on the organization of actin in fibroblasts. The cells are labelled with fluorescent phalloidin to show the F-actin distribution within the cells. (A) Control cells have F-actin concentrated at the cell edge at the cortex, and exhibiting a few stress fibers. (B) The microinjection of constitutively active Rho causes an abundance of stress fibers to be formed. (C) Microinjection of constitutively active Rac causes the formation of lamellipodium around all edges of the cell. (D) Microinjection of constitutively active Cdc42 causes numerous filopodia spikes to form all around the edges of the cell. This figure illustrates how the different concentrations of proteins upstream of F-actin expression influences the type of actin-rich structure formed. Referenced from (7).

An example of how Rac and Rho GTPases bring about changes in the major F-actin structures formed in cells in shown in **Fig. 1.6**. This figure is referenced from (7). In this figure, the cells are labelled with fluorescent phalloidin. This causes the F-actin within the cells to be visible when seen under the fluorescent microscope. The effects of Rac, Rho, and Cdc42 on the organization of actin in fibroblasts are then investigated by the microinjection of constitutively active forms of Rac, Rho and Cdc42, increasing the levels of these GTPases within the cells. In **Fig. 1.6A**, control cells have their F-actin concentrated at the cortex near the cell periphery, and the cells exhibit few stress fibers. In **Fig. 1.6B**, constitutively active Rho is microinjected into the cells. This causes numerous stress fibers to be formed, much more than when compared to that in the control case. In **Fig. 1.6C**, the microinjection of constitutively active Rac causes the lamellipodia to form all around the cell periphery. The absence of any clear stress fibers is in contrast to the case where constitutively active Rho is microinjected into the cell. In **Fig. 1.6D**, the microinjection of constitutively active Cdc42 causes an abundance of filopodia spikes to form all around the edges of the cell. This figure shows how the various concentrations of protein GTPases upstream of F-actin expression causes different F-actin structures to form within cells.

1.3. Role of Extracellular Stiffness on Cell Behavior

At the interface of cell-substrates, it has been shown that cells can feel extracellular cues such as substrate stiffness and topography, bringing about cell behavorial responses to the extracellular cues (27). These responses are in relation to connections between the ECM and the other molecular complexes of the cell, which include integrins and focal adhesions (FAs) located

on the cell membrane surface. This interface provides a physical linkage between the ECM and the cytoskeleton within the cell, and is the basis by which extracellular forces can be transmitted to structures within the cell (28).

At the proximity of the cell-substrate interface, cell-based FA complexes are formed. These complexes are composed of various adhesion and transmembrane proteins such as integrins, talin, vinculin and focal adhesion kinases (FAK). The FA complex provides a connection between the ECM and the cytoskeleton within the cell, as the stress fibers and other cytoskeletal structures are connected directly to the FA complexes. These are important structures which transmit mechanical force into living cells, allowing mechanotransduction to occur. The extracellular forces can then affect downstream responses in the cells. These responses include differential gene expression and downstream protein signal transduction (28, 29).

A well-documented cell response to substrate stiffness is the change in cell morphology and cytoskeletal structure within the cells. It has been shown that cells are well-spread on stiffer substrates, with more stress fibers being formed as compared to cells being spread on softer substrates (1). Although this is true in single cells, when cells come into contact with one other (as is the case of a confluent sheet of cells grown on a substrate), this stiffness-dependence of cell morphology and stress fiber formation is no longer evident.

The effect of substrate stiffness on cell migration speed follows a biphasic relationship (30). On very soft and very hard substrates, cell migration speed on a 2-D substrate is significantly lower than that of cells on a substrate on intermediate stiffness. This behaviour could be attributed to the increase in cell traction forces exhibited within cells as substrate

stiffness increases (31). In addition, cell movement has been shown to be guided by substrate rigidity in durotaxis (2). On a substrate with an interface between a soft and hard region, single cells migrating along the substrate show the ability to move from the soft region into the hard region, but not from the hard to the soft region. As a result of this durotactic study, many other groups have come up with studies to elucidate the effects of differential localized stiffnesses on 2-D substrates on cell behaviour (32).

Since FAs and FA complexes are at the interface of cells, it is to be expected that substrate stiffness would somehow affect the physical properties of these structures during cell migration (33). Larger FA complexes are found in cells on stiffer substrates, and the formation of new FAs is followed by external propulsive mechanical forces by the cell at the leading edge, resulting in the movement of the cell forward. Mature FA complexes play a role in anchoring the cell to the substrate, rather than in the forward movement of the cell.

Extracellular stiffness is also known to affect stem cell differentiation. MSCs have been shown to differentiate into various lineages based on the stiffness of their underlying substrate (5), which has possible implications for stem cell therapies. This is illustrated in **Fig. 1.7**, which has been referenced from (5). On substrates with stiffnesses of 1, 10 and 40 kPa, MSCs commit to the neurogenic, myogenic and osteogenic lineages respectively. **Fig. 1.7A** shows how the stiffness of tissues is characterized by the elastic modulus, E. The stiffness of brain, muscle and collagenous bone tissues range from 1, 10 and 100 kPa respectively. In **Fig. 1.7B**, MSCs are grown in vitro on gels with three main groups of varying elasticities; from 0.1-1 kPa, from 8-17 kPa and from 25-40 kPa. At the start of the experiment, the MSCs are rounded. After 4, 24 and 96 hours, the morphologies of MSCs increasingly change to resemble branched, spindle, or

polygonal shapes, when grown on respective gels in the range typical of brain (0.1–1 kPa), muscle (8–17 kPa), or collagenous bone (25–40 kPa) tissues.

In addition to the results shown in **Fig. 1.7** which shows that the elasticity of the extracellular environment can determine stem cell differentiation fate, studies have also shown that the appropriate mechanical preconditioning of stem cells with respect to their *in vivo* environment improved their transplantation outcome in their respective targeted tissue environments. For example, the mechanical loading of stem cells has been shown to improve the transplantation outcome in acute myocardial infarction (34), when compared to the direct transplantation of nascent stem cells into the affected area of the heart. This could be a result of the natural heart tissue environment being under cyclic stretching as the heart pumps blood to the rest of the body, and by subjecting the stem cells to this mechanical loading stimulus before implantation into the affected area of the heart, the chances of stem cell differentiation into heart tissue cells are greatly increased.

It is worth mentioning that while substrate stiffness does have a major role in dictating cell behavior, other physical properties of the substrate do contribute to cell behaviour as well. An example is the localized topography of the substrate, such as grooves and wells. These localized topographies alter cell morphology, alignment and the distribution of structural molecules within the cell (35-37). Substrate grooves ranging from sizes of 20-200 nm have been shown to alter cell migration direction and bring about actin reorganization within cells (38, 39). Although the sizes of cells when spread-out on 2-D substrates is in the order of ten of microns, cells exhibit the ability to sense topographical size variations in the order of nanometers (40-44).

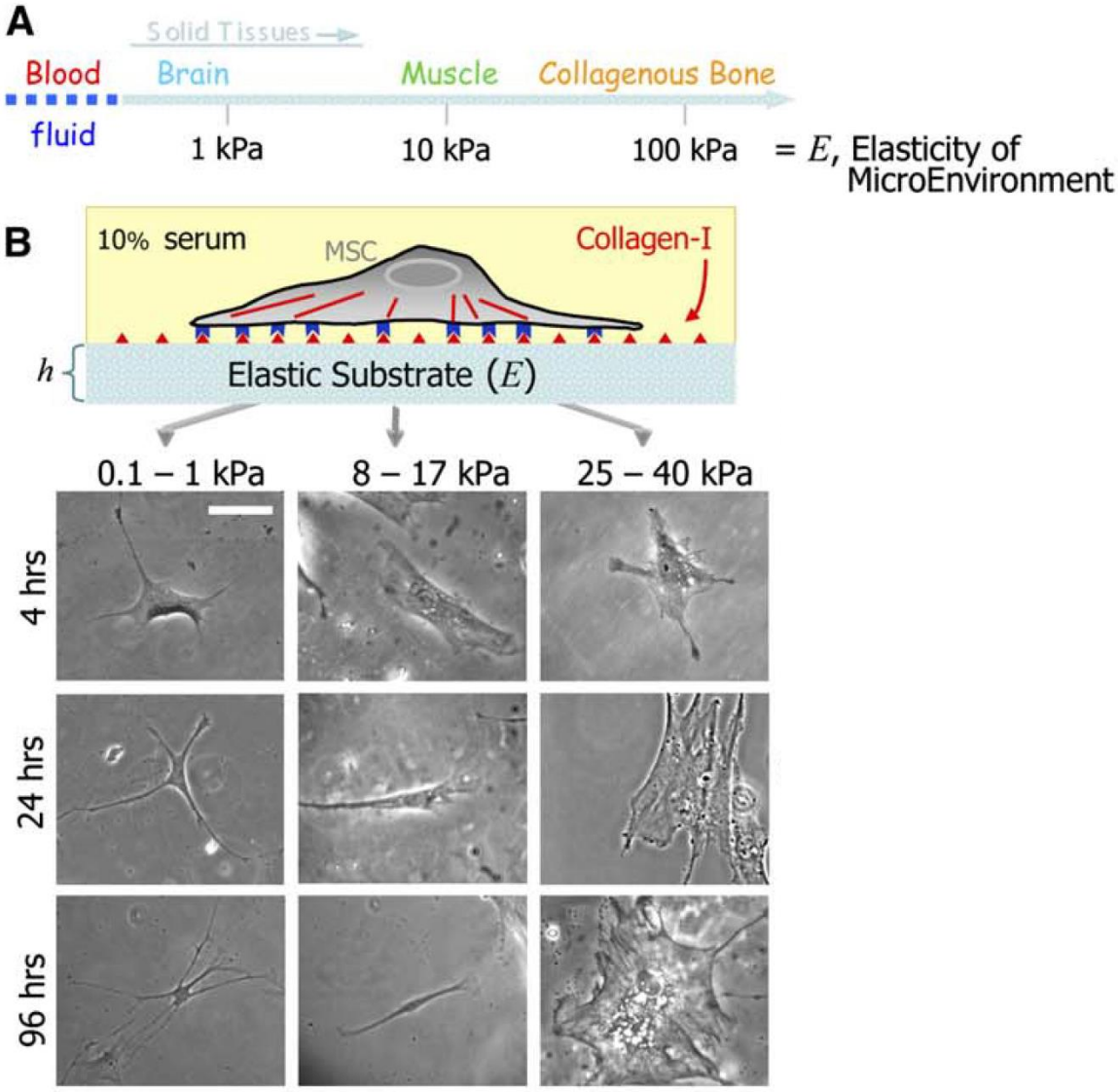

FIGURE 1.7: The influence of tissue elasticity on the differentiation of MSCs. (A) The stiffness of tissues is characterized by the elastic modulus, E. These range from brain (1 kPa) to muscle (10 kPa) and collagenous bone (100 kPa). (B) MSCs are grown *in vitro* on gels with three main groups of varying elasticities; from 0.1-1 kPa, from 8-17 kPa and from 25-40 kPa. Initially, the morphology of the MSCs are small and round. After 96 hours, the morphologies of MSCs change to resemble branched, spindle, or polygonal shapes when grown on matrices respectively in the

range typical of brain (0.1–1 kPa), muscle (8–17 kPa), or collagenous bone (25–40 kPa) tissues. Scale bar denotes 20 mm. Referenced from Engler et al. (5).

1.3.1 Spatial substrate stiffness control of elastic substrates in vitro

Studies of how spatial differences in substrates which cells are cultured on *in vitro* affect cell behaviour have been done extensively over the last decade. Lo et al. (2) conducted the first study of durotaxis, whereby cell migration is guided by gradients in substrate stiffness. An example of their work on durotaxis is shown in **Fig. 1.8**. 3T3 fibroblasts were cultured on polyacrylamide (PA) gels with two distinct stiffnesses, which will be denoted as the stiff and soft sides. A distinct boundary on the substrate between the stiff and the soft sides is visible (**Fig. 1.8**). When cells migrate from the stiff side of the substrate towards the soft side, they are able to cross the boundary between the two stiffnesses effortlessly, as shown in **Fig. 1.8a**. However, when cells on the soft side move towards the boundary (**Fig. 1.8b**), they do not cross the boundary into the stiff side. Rather, they migrate along the boundary, on the soft side of the substrate, or turn back towards the stiff side and migrate further in. Therefore, in a cell culture with cells migrating on a substrate with both stiff and soft sides, eventually most of the single migrating cells would end up on the stiff side of the substrate. This shows that spatial gradients in substrate stiffness can guide cell motility, and hence play an important role in cell migration.

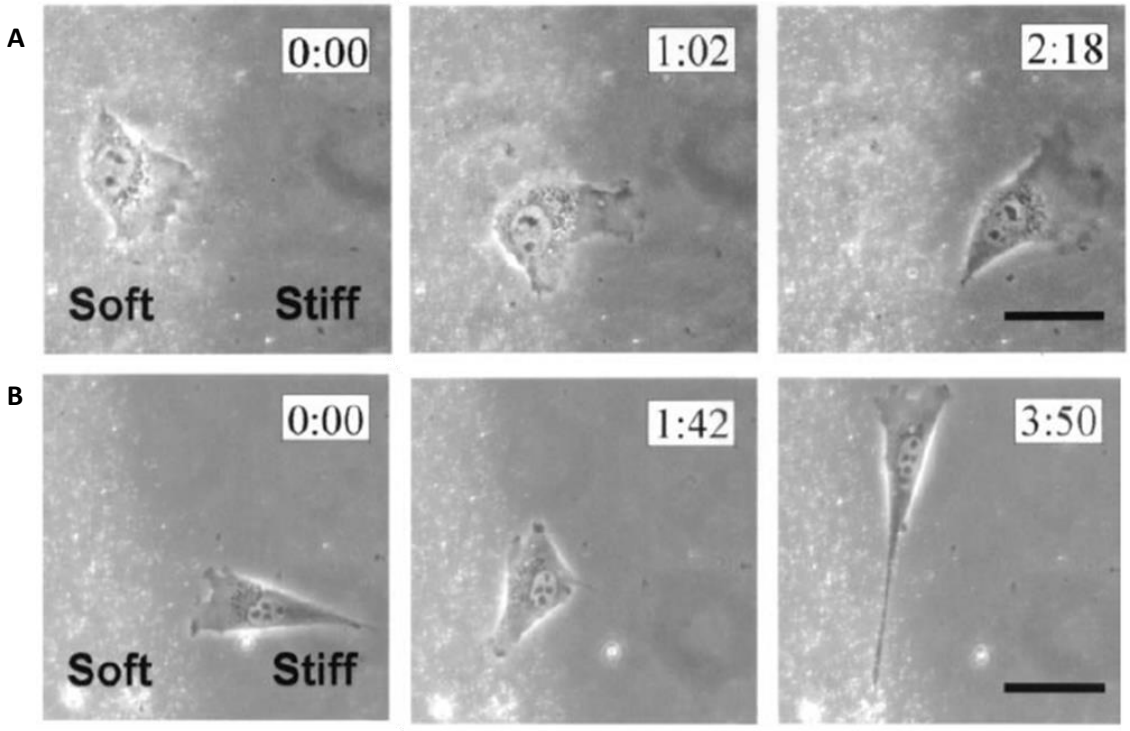

FIGURE 1.8: Phase contrast images of 3T3 cells moving on substrates with a rigidity gradient. (A) A cell moving towards the stiffness boundary from the soft side of the substrate. The cell is able to cross directly the stiffness boundary from the soft to the stiff side. (B) A cell moving towards the stiffness boundary from the stiff side of the substrate. The cell does not cross the stiffness boundary to the stiff side, migrating instead along the stiffness boundary. Referenced from (2).

In addition to using two different stiffnesses of PA gels to study durotaxis of cells in 2-D substrates, techniques used in soft lithography have been used to create PA gels with uniform stiffness gradients (45) as shown in **Fig. 1.9A**. A photoinitiator is used to polymerize the PA gels in this setup, and the polymerization of the PA gel is carried out by exposing the surface of the gel to UV light using a UV lamp. The degree of polymerization of the PA gel is dependent on the intensity and amount of UV light reaching the gel. The higher the degree of polymerization,

the stiffer the PA gel becomes. As such, a photomask filter is used which allows a gradient intensity of UV light to pass through it before reaching the PA gel and polymerizing it (**Fig. 1.9A**). The advantage of the soft lithography method is that it creates a PA gel with different spatial degrees of polymerization and hence PA gels with uniform gradients of stiffness, which can then be used to study cell durotaxis.

Another method for creating 2-D substrates with spatial variations in gradient to study durotaxis in cells is by using techniques in microfluidics (32) shown in **Fig. 1.9B**. This method utilizes polydimethylsiloxane (PDMS) of different stiffnesses (soft and hard) to create spatial differences in stiffnesses. From a micropatterned silicon wafer with protruding patterns of strips with different thicknesses, such as 30 and 100 μm, uncured stiff PDMS is poured onto the wafer and cured to allow it to solidify. The PDMS mold is then slowly peeled away from the surface of the silicon wafer. This creates a solidified stiff PDMS mold with depressed strips or channels, which is shown by the blue portion of the substrate in **Fig. 1.9B**. Next, uncured soft PDMS is poured into the channels present in the hard PDMS and left to cure, forming strips of soft PDMS (orange) embedded in hard PDMS (blue) as shown in **Fig. 1.9B**. This creates a spatial gradient of substrate stiffness in which cells can be seeded on. A major advantage of this method is that it can be fabricated with minimal effort, and the length of the soft substrate strips can be varied within the same 2-D substrate to study the effects of different lengths of spatial stiffnesses on cell behavior.

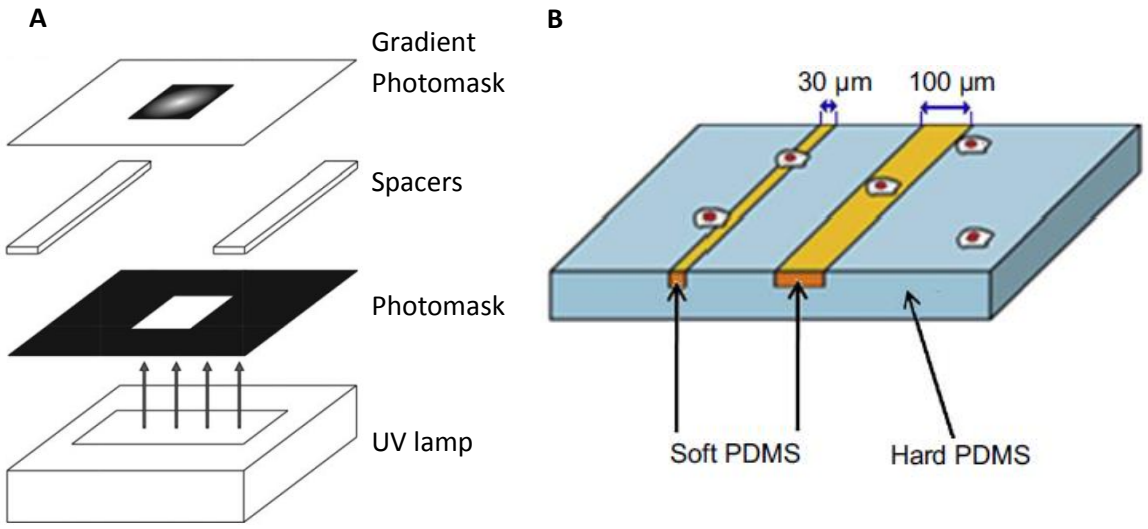

FIGURE 1.9: Different methods for creating 2-D substrates with spatial differences in stiffnesses. (A) The soft lithography method utilizes a photomask filter, which creates a gradient of UV light impinging on unpolymerized PA gels containing a photoinitiator, resulting in a PA gel with varying degrees of polymerization and a gradient in spatial stiffness. (B) Soft PDMS (orange) with varying widths patterned on hard PDMS (blue) using microfluidic techniques for cell durotactic studies. Referenced from (45) and (32) respectively.

1.3.2 Importance of dynamically changing environmental stiffness on cells and tissues in vivo

The stiffness of environments in tissues of the body often shows variations both spatially and temporally. For example, during wound healing, fibroblasts can differentiate into myofibroblasts at the site of the wound (46), as shown in **Fig. 1.10**. Under normal conditions, fibroblasts are exposed to the stiffness of the surround ECM at the pre-wound site. When the

wound occurs, inflammatory signals and profibrotic cytokines cause the fibroblasts to migrate to the site of injury and differentiate into proto-myofibroblasts. These cells secrete transforming growth factor β1 (TGFβ1), and together with ED-A fibronectin sites which are exposed in the ECM by the increased cell tension applied by these cells, causes the proto-myofibroblasts to express α-smooth muscle actin (α-SMA), resulting in increased stress fiber and larger focal adhesion formations and further increasing the cell-generated tension and ECM fiber remodelling (**Fig. 1.10**). These result in the stiffening of the ECM environment. Eventually, differentiation of proto-myofibroblasts into fully differentiated myofibroblasts occurs, whereby the extracellular stiffness of the wound area is greater than that of the original intact tissue. The myofibroblasts eventually undergo apoptosis once the ECM at the wound site is reconstituted, and the stiffness of the tissue around the wound site is restored to that of the original intact tissue.

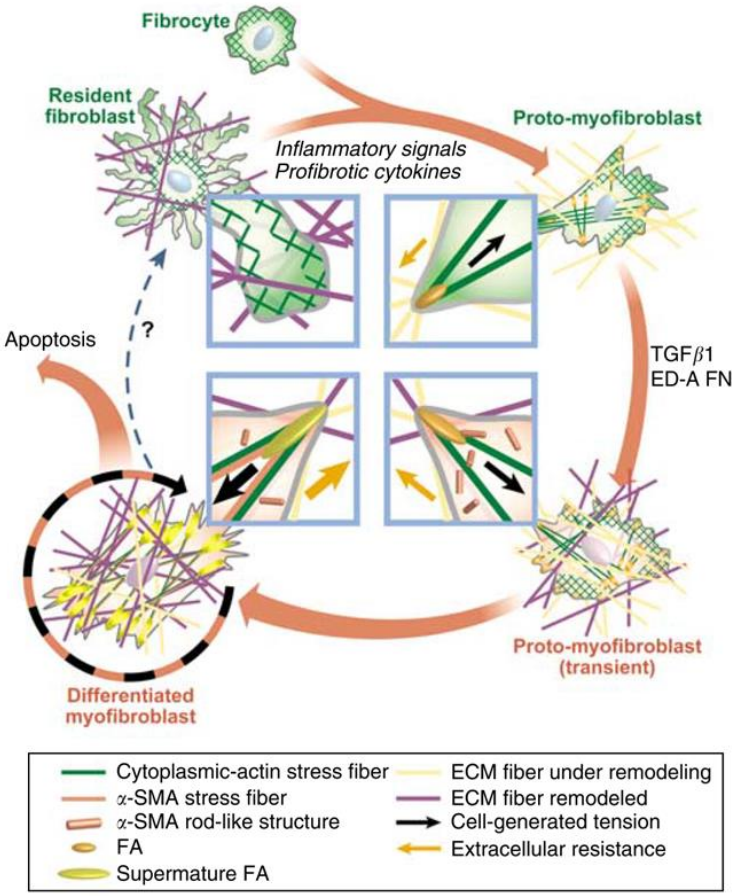

FIGURE 1.10: The stiffening of the extracellular tissue at the wound healing site. Fibroblasts are recruited to the site of the wound by inflammatory signals and cytokines, resulting in the formation of proto-myofibroblasts. The expression of α-SMA by the cells, stimulated by TGFβ1 in the presence of ED-A fibronectin, causes increased stress fiber and focal adhesion formation, resulting in increased cell-tension and ECM remodelling. This causes increased ECM stiffness and the differentiation of proto-myofibroblasts to myofibroblasts. The wound tissue is thus stiffer than the normal intact tissue. When the wound tissue stiffness has reverted back to that of the original tissue, these myofibroblasts undergo apoptosis. Referenced from (46).

Another example of how the surrounding stiffness of the tissue in the body changes dynamically is that of the breast tissue during cancer development, as shown in **Fig. 1.11**. This figure is referenced from (6). Here, the blue cells represent the transformation which stem from the accumulation of genetic changes in the epithelium together with a stiffened stromal matrix, resulting in rampant proliferation and increased survival of luminal epithelial cells within the ductal tree, which results in an abnormal ductal architecture. After some time, the abnormal luminal mammary epithelial cells proliferate and growth enough to fill the breast ducts. These proliferating cells form an expanding mass that exerts and outward compressing force on the basement membrane as well as the adjacent myoepithelium, which results in an inward resistance force from the surrounding tissue. The damaged tissues secrete many soluble factors which result in the infiltration of immune cells, as well as the activation of nearby fibroblasts to cause the growth of fibrous and connective tissue in the breast stroma, which stiffens over time. This stiffened tissue applies an increasingly larger inward resistance force on the expanding abnormal cell mass in the duct. Increased matrix metalloproteinase activity results in the thinning of the basement membrane and the decrease in the number of myoepithelial cells surrounding the duct. There is also increased interstitial fluid pressure due to a leaky vasculature and faulty lymphatic drainage in the breast tissue. The abnormal luminal epithelial cells apply an increasingly outward force to counter the increasingly forces applied on them by the surrounding stiff tissue, and eventually invade into the surrounding breast tissue.

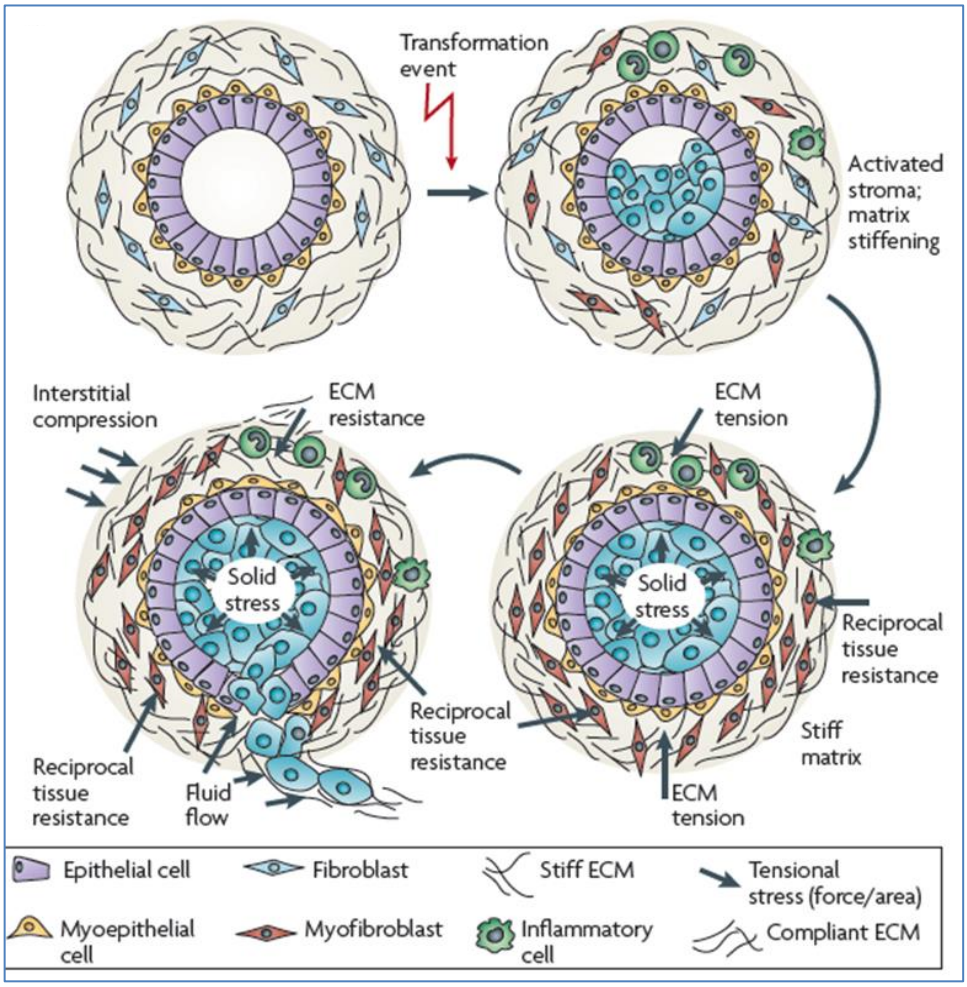

FIGURE 1.11: The stiffening of the extracellular tissue during breast cancer development. The blue cells denote the transformation which comes from the buildup of genetic changes in the epithelium and a stiffened stromal matrix, causing proliferation and survival of luminal epithelial cells residing within the ductal tree. Then, the abnormal luminal mammary epithelial cells proliferate and growth, filling the breast ducts. The proliferating cells result in a growing mass of cells that exert and outward force on the basement membrane and adjacent myoepithelium. The damaged tissues secrete soluble factors, causing the infiltration of immune cells, as well as the activation of nearby fibroblasts resulting in the growth of fibrous and connective tissue in the breast stroma which increases in stiffness over time, which in turn applies an increasing inward resistance force on the expanding abnormal cell mass in the duct. Matrix metalloproteinase activity is increased, causing the thinning of the basement membrane and reducing the number of myoepithelial cells

surrounding the duct. Increased interstitial fluid pressure due to a leaky vasculature and faulty lymphatic drainage in the breast tissue occurs. Abnormal luminal epithelial cells apply an increasing outward force to counter the increasing forces applied on them by the surrounding stiff tissue, and they eventually invade into the breast tissue. Referenced from (6).

1.3.3 Existing methods used to study the effects of dynamically changing substrate stiffness on cell behavior

Many of the existing methods used to study the effects of substrates stiffness on cell behaviour as mention previously are static systems, which mean that the stiffness of the substrates do not change in time. As mentioned in the previous section, many of the tissue environment surrounding cells in the body experience dynamically changing stiffnesses. As such, a few substrate systems with dynamically changing stiffnesses have been produced. An example of such a system was made by Frey and Wang (47). In this system, a photodegradable PA gel is used, whereby the stiffness of the gel can be reduced by the application of UV light. This system was then used to look at the behaviour of 3T3 cells as shown in **Fig. 1.12**. The substrate underlying the posterior and anterior region of the cells were softened with UV (white circles) respectively, and the cell spread area was observed. It was found that softening of the posterior regions of the cell substrate causes the cell to migrate away from the softened substrate, but does not decrease the cell spread area. Softening of the anterior regions of the cell substrate however produced a decreased in cell spread area as well as a change in cell polarity, as shown in **Fig. 1.12**.

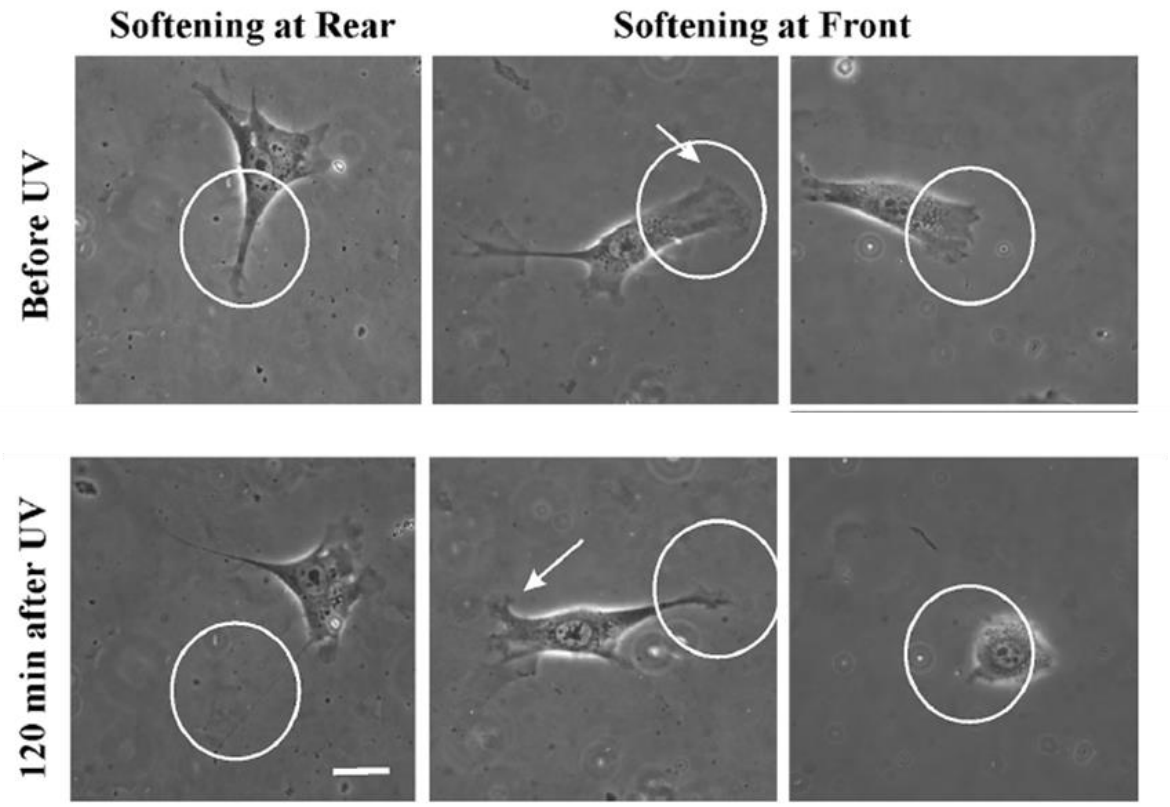

FIGURE 1.12: Softening of PA substrate underlying the anterior and posterior regions of 3T3 cells using UV light. White circles denote region of application of UV light either at the anterior or posterior region of the cell substrates. Cell spread area changes with softening of substrate at the anterior region of the cell, but does not change with softening of substrate at the posterior region of the cell. In both cases, the cell moves away from the region of softened substrate. Referenced from (47).

Another method of creating substrates of dynamically changing stiffnesses to study cell behaviour was created by Guvendiren et al. (48), as shown in **Fig. 1.13**. These hydrogel substrates where obtained by a Michael-type addition reaction where dithiothreitol (DTT) is mixed into methacrylated hyaluronic acid (MeHA). In this initial gelation phase, the number of methacrylate groups that takes part in the crosslinking reaction can be adjusted by the

concentration of DTT, in a process known as addition-only polymerization. A photoinitiator is then introduced into the hydrogel, which can then be stiffened over time by the exposure of the gel to UV light via radical polymerization as shown in **Fig. 1.13A**. The storage and loss modulus (*G'* and *G''*) of the polymers represented by closed and open circles respectively undergoing the UV independent addition-only polymerization as well as the UV dependent radical polymerization is shown in **Fig. 1.13B**. It can be seen that the introduction of UV light at the 25 min mark causes the rapid stiffening of the polymer via radical polymerization, which is larger in magnitude to the stiffening achieved by addition-only polymerization. In **Fig. 1.13C**, how the initial amount of DTT added to the hydrogel affects the stiffness of the gel is shown. It can be seen that increasing the DTT fraction in the gels increases the gel stiffness in all cases, and that the addition + radical polymerization of the gels is always higher than the addition-only polymerization of the gels across all DTT fractions.

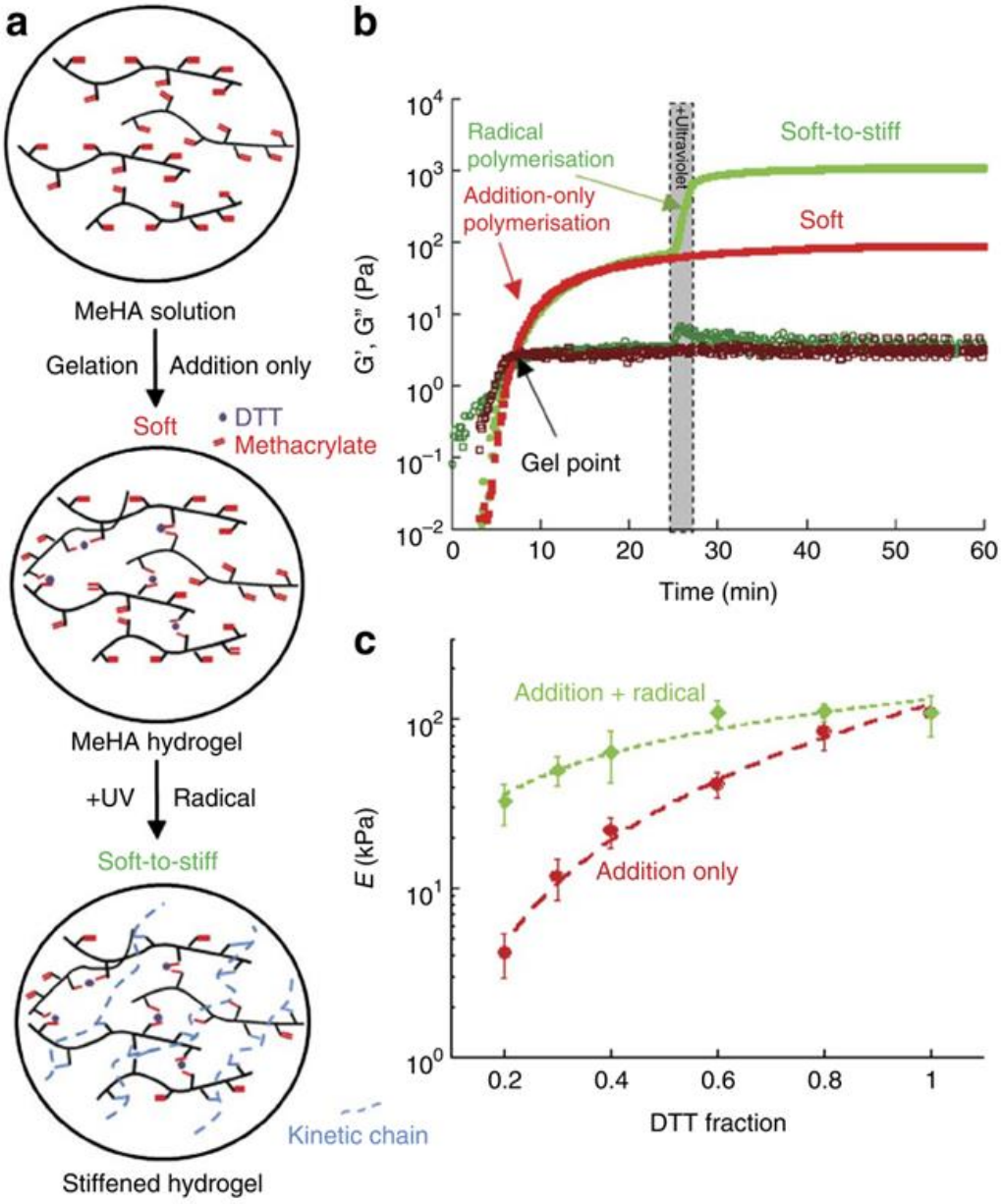

FIGURE 1.13: Stiffening of MeHA gels using UV light. (A) MeHA can be stiffened initially using DTT (addition-only polymerization), and subsequently by the addition of a photoinitiator and exposure to UV light (radical polymerization). (B) The storage and loss modulus, *G'* and *G''*, denoted by closed and open circles respectively, is shown as a function of polymerization time. It can be seen that in the radical polymerization curve, stiffening of the substrate is greatly increased by the

exposure to UV light at 25 min. (C) The effects of DTT fraction on the Young's. Increased DTT fraction increases the stiffness in all cases of polymerization. The case of addition + radical polymerization is always stiffer than the addition-only polymerization case across all DTT fractions. Referenced from (48).

The previous two cases have shown examples of dynamic stiffness systems controlled using the application of UV light. Another method of stiffness control is that of temperature, in which Krekhova et al. (49) used to tune the mechanical properties of their gel. In their setup, thermoreversible hydroferrogels were made via gelation of aqueous maghemite ferrofluids using the triblock copolymer Pluronic P123 as a gelator. This allows the control of the storage and loss modulus (*G'* and *G''*) by using temperature as shown in **Fig. 1.14**. As shown in the figure, the application of increasing temperature from 5 °C onwards causes an initial increase of *G'* and *G''*. Further increasing temperature causes the decrease of *G'* and *G''*. Hence, the hydroferrogels show a biphasic relationship between stiffness and temperature. However, for the practical usages of these gels in cell culture, the range in which these gels can be tuned using temperature is only around the 37 °C mark, as denoted by the red dotted line in **Fig. 1.14**.

A major disadvantage of the UV light and temperature induced dynamic change in stiffness substrate systems for use in cell culture studies is that these stimulates are detrimental to cells at high doses. For example, the prolonged application of UV light to cells, especially sensitive cells such as stem cells, causes them to undergo unfavourable genetic changes and even apoptosis (50). Mammalian cells also survive under a very narrow temperature change around 37 °C, which makes the usage of temperature as a means of controlling substrate stiffness in which cells are seeded on very limited in its effectiveness.

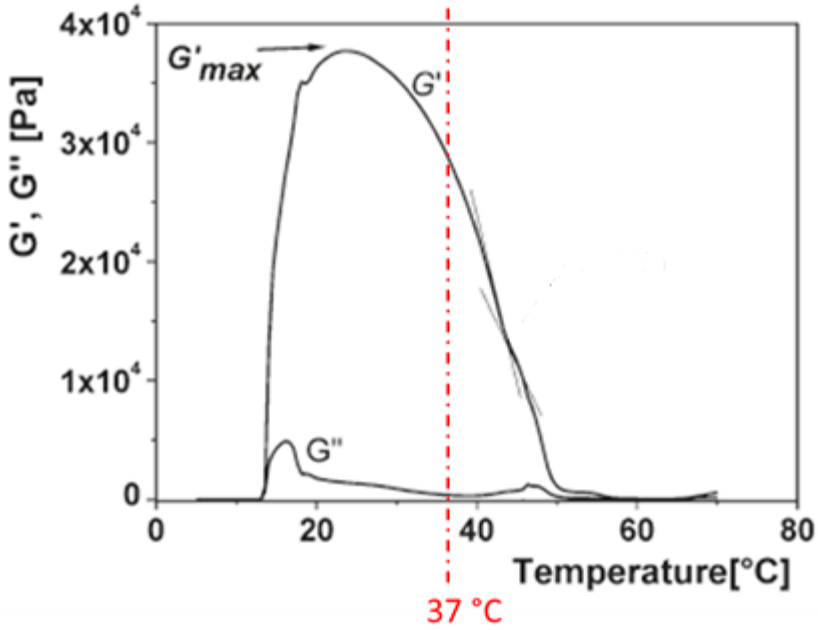

FIGURE 1.14: Controlling the storage and loss modulus of thermoreversible hydroferrogels using temperature. As temperature is increased from 5 °C, the storage and bulk modulus of the gel, *G'* and *G''*, increases to a maximum, whereby the further increase of temperature would cause them to decrease. The vertical red dotted line denotes the temperature of 37 °C, which is the optimum temperature for mammalian cell cultures. Referenced from (49).

1.4. Circular Dorsal Ruffles

CDRs are actin-rich structures formed on the dorsal surface of many mammalian cells after stimulation with various growth factors such as the PDGF (51–53). CDRs form in a ring-like manner on the dorsal surface of stimulated cells (thus the term ‘‘circular dorsal ruffles’’ or ‘‘circular membrane ruffles’’) (51, 54, 55). Furthermore, protrusion of the dorsal surface of the

plasma membrane has been observed at CDRs, and is thought to be driven by polymerization of the branched actin filament network (56). CDRs are dynamic and transient in nature, transversing along the dorsal membrane and disappearing within tens of minutes after growth factor stimulation (57). Less frequent occurrences of CDRs in tumor cells as compared to normal cells suggest that these structures might play an important role in cancer progression (54). In addition to actin, other proteins such as WAVE1, WAVE2, N-WASP and the ARP 2/3 complex are also localized to CDRs (13).

Experimental images of CDRs are shown in **Fig. 1.8**. This figure is referenced from (13). In **Fig. 1.8A**, a scanning electron micrograph (SEM) of a human foreskin fibroblast (HF) that was stimulated with PDGF for 5 minutes is shown. In the boxed out region at the cell membrane, a protruding ridge of the CDR can be seen. The inset image taken at a higher magnification shows that the CDR consists of many tiny bumps that protrude from the dorsal surface (arrowheads). **Fig. 1.8B** shows a fixed 3T3 fibroblast 5 min after stimulation with PDGF. The cell is stained for F-actin (blue), cortactin (green) and dynamin (red). Colocalized (white regions) of all three cytoskeletal proteins occurs at the CDRs (arrowheads), showing that all three proteins are likely found in the proximity of CDRs. A significant amount of stress fibers (blue) extend through the cell interior, but are absent in the vicinity of the CDR.

Although the functions of CDRs have not been conclusively established, they are generally believed to be involved in aiding cell motility (58–60) by providing large-scale reorganization of the actin cytoskeleton (57, 61, 62). In particular, cells that exhibit CDRs after PDGF stimulation have been observed to possess a higher degree of lamellipodial protrusions compared to cells that do not (57). In addition, it has been suggested that CDRs aid in the process of macropinocytosis (63), which allows the cell to internalize extracellular material including

molecules and other particles such as cell fragments (64) efficiently. Cells that exhibit CDRs show an increase in macropinocytosis activity (65, 66), and macropinosomes form at the site where CDRs disappear on the membrane surface.

A third function of CDRs is the sequestration and internalization of receptor tyrosine kinases (RTK) after cell stimulation with ligands. This plays an important role in the modulation of growth factor initiated signaling events, which govern various cellular processes such as cell invasion, motility, and mitosis (63). When cells that express epidermal growth factor (EGF) receptors tagged with green fluorescence proteins are stimulated with EGF, it was observed that the EGF receptors localized within CDRs before being internalized from the cell membrane (67). This suggests that the constriction of CDRs could bring together the RTKs to a singular point on the membrane, facilitating their subsequent internalization into the cell.

An illustration of receptor internalization is shown in **Fig. 1.9**, which is referenced from (68) and shows the formation of a CDR in a PANC-1 pancreatic adenocarcinoma cell expressing epidermal growth factor receptor (EGFP) green fluorescent protein (GFP) being stimulated with EGF. In **Fig. 1.9A** which shows the cell 5 min after EGF stimulation, four separate CDRs denoted by the box and arrows are formed. The boxed region containing the CDR is shown at a higher magnification in **Fig. 1.9B**. EGFR-GFP is found within the CDR (denoted by arrows). In **Fig. 1.9C**, 15 min after EGF stimulation, the size of the CDR has decreased and tubules with vesicles (arrows) can be seen radiating from the CDR, indicating the EGFR is actively being trafficked or internalized away from the CDR. After 25 min of EGF stimulation (**Fig. 1.9D**), the trend of decreasing CDR size and the increased tubule formation (arrows) from the CDRs is seen. In addition, EGFR-GFP spots can now be seen away from the CDRs (arrowheads), suggesting that the EGFR-GFP could have been transported from the CDRs to other regions of the cell.

1.5. Conclusion

In this chapter, how cells interact with their environment was introduced. Mainly, how protein connections, such as integrins, connect the extracellular environment to the internal structure of the cell was discussed. The different environment stiffnesses for cells in various tissues were looked at. A discussion on the major component of the internal cell structure, the cytoskeleton, which is composed in part by the protein actin, and the various actin-rich structures in cells were looked at, as well as how the tuning of extracellular environment stiffness affects cell behavior, such as cell migration speed, spread area and stem cell differentiation. Lastly, we focused on the structure and functions of the actin-rich CDRs within cells. The following paragraphs outline the contents of the other chapters found in this thesis.

The objective of this thesis is to investigate the role of substrate stiffness on actin-rich structures in cells, which consequently affects cell behavior. We believe this is important for the reasons stated in this chapter, mainly that the stiffness of the extracellular environment varies for different tissues in the body, such as brain, muscle and bone tissues. As such, cell survival, behavior and differentiation are fine tuned to the niche environment in which the cells reside in, making the stiffness of the extracellular environment an important parameter to study with respect to cell behavior. Specifically, we focus on the actin-rich structure known as the CDR, where little is known about their exact functions and mechanism of formation within cells.

In chapter 2, CDR behavior is investigated through varying substrate stiffness and the construction of a mathematical model as the dynamics and mechanism of CDR formation are

still not known. It has been observed that CDR formation leads to stress fibers disappearing near the CDRs. Because stress fiber formation can be modified by substrate stiffness, we examine how substrate stiffness affects CDR formation. We seed Nation Institute of health (NIH) 3T3 fibroblasts on glass and polydimethylsiloxane substrates of varying stiffnesses, ranging from 20 kPa to 1800 kPa, and develop a mathematical model of the signaling pathways involved in CDR formation to provide insight into the CDR lifetime and size dependence that is linked to stiffness of the underlying cell substrate via the Rac-Rho antagonism.

In chapter 3, we investigate how CDRs increase the persistency of cell migration by the reorganization of actin. We look at the role of CDR formation, specifically in cell motility, for 3T3 fibroblasts cultured on 10 kPa PA substrates. We find that CDR formation increases cell migration directional persistency but does not affect the migration speed. The findings in this chapter adds to the understanding of the complex interplay between actin structures in cell behavior, and have a wide range of implications in various fields including cell motility, actin biophysics, and biological materials.

In chapter 4, we introduce a novel method on how substrate stiffness can be modulated dynamically using thin polymer membranes. To further investigate the effects of cell-substrate interactions on actin dynamics and cell behavior, a 2-D system which enables the tuning of a dynamic, reversible and localized substrate stiffness environment is constructed in this chapter. Cells that are seeded on top of thin PDMS membranes are capable of feeling through the thin membrane and sensing the stiffness of the substrates underneath. These thin membranes are then carefully removed and placed on top of other substrates with different stiffnesses, forming a reversible dynamic stiffness system which can be used in the investigation of how reversible

dynamic stiffness environments affect cell, motility, proliferation, differentiation and morphology in different cells.

In chapter 5, the conclusion of the thesis is presented, summarizing the main findings and their significance from the research work done here. This is followed by a discussion on the future work and studies which can be done from the findings of this thesis.

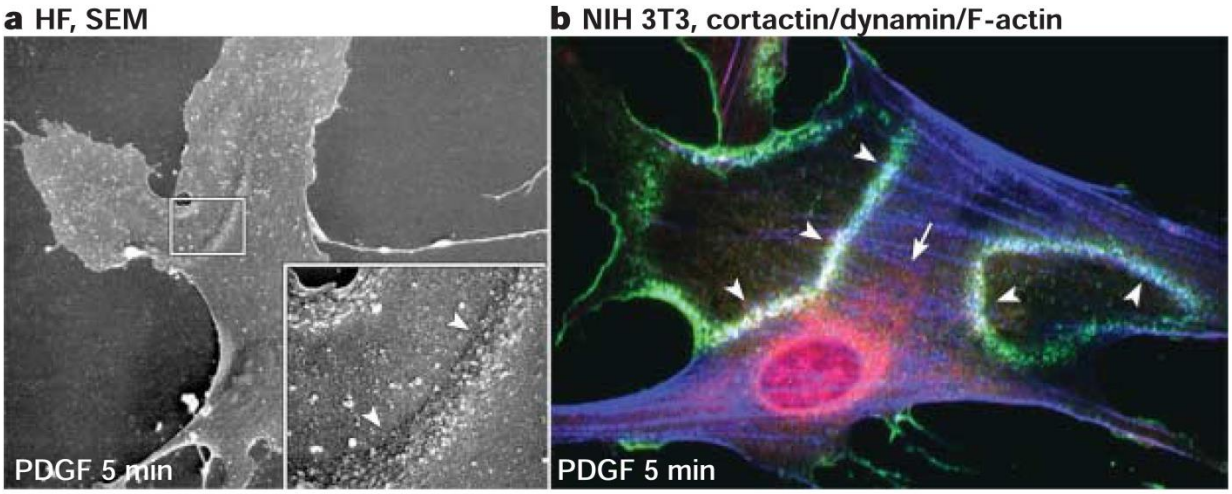

FIGURE 1.15: Experimental images of CDRs. (A) SEM image of a cultured human HF that was stimulated with PDGF for 5 min. A protruding CDR at the dorsal plasma membrane can be seen (small box). The inset shows a magnified region of the box, and the CDR is seen to consist of bumps that protrude from the dorsal surface (denoted by the arrowheads) across the cell surface. (B) A 3T3 fibroblast fixed after PDGF stimulation for 5 min, and stained for dynamin (red), cortactin (green) and F-actin (blue). Colocalization (white) of the three cytoskeletal proteins is shown at the CDRs (arrowheads). Stress fibers (blue) that span through most of the

cell are missing within the CDR region. The arrow points to dynamin, which is also present on the Golgi. Referenced from (13).

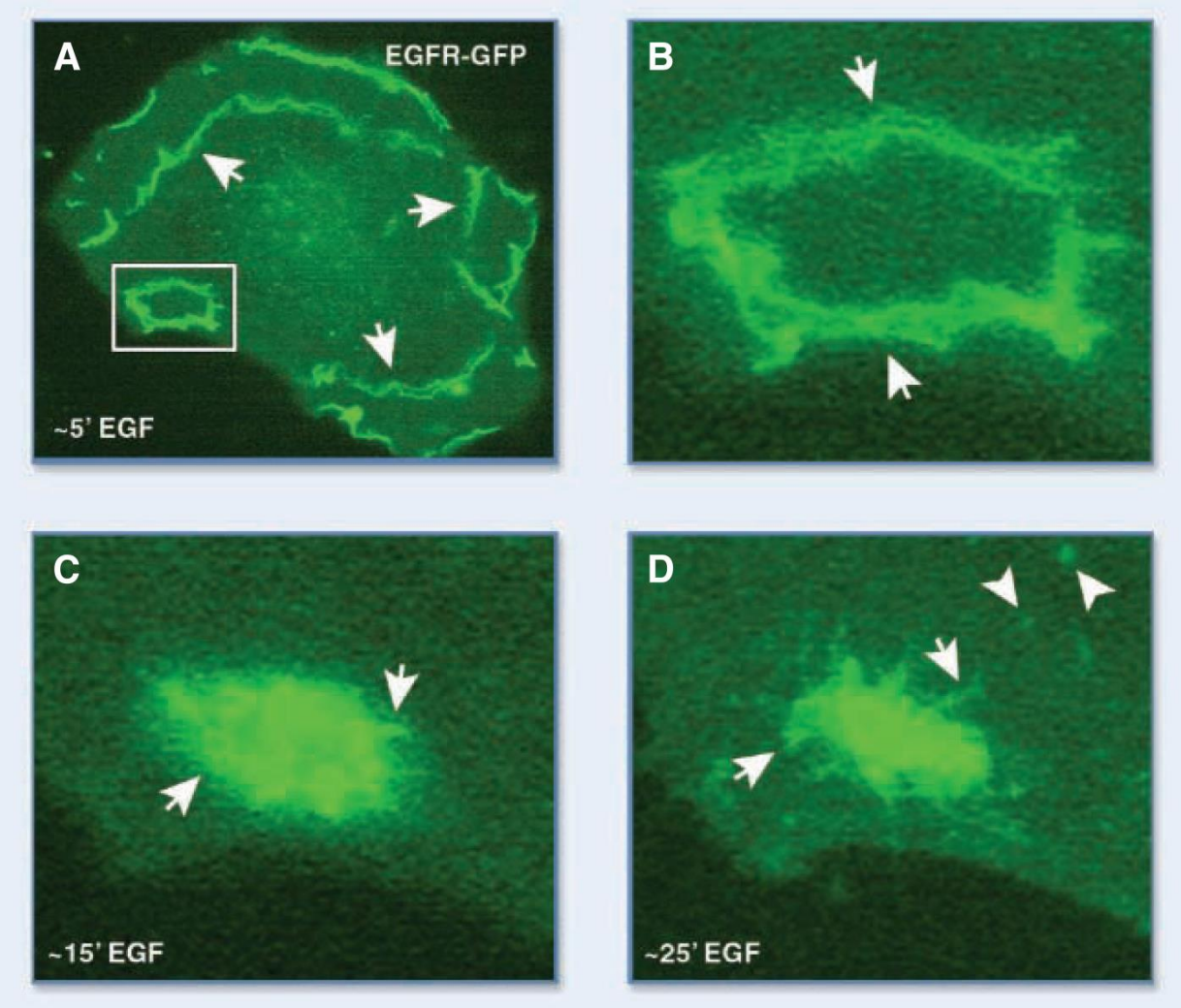

FIGURE 1.16: Fluorescence image showing the formation of CDRs in a PANC-1 pancreatic adenocarcinoma cell expressing EGFP-GFP, after being stimulated with EGF for up to 25 min. (A) The cell 5 min after EGF stimulation, with a boxed region and arrows showing four separate CDRs formed. (B) The boxed region containing the CDR is shown at high magnification. EGFR-GFP is found within the CDR (arrows). (C) The cell 15 min after EGF stimulation. CDR size has decreased and

tubules (arrows) extend from the CDR with vesicles dynamically moving away from them, indicating the EGFR may be actively trafficked or internalized away from the CDR. (D) The cell after 25 min of EGF stimulation. CDR size has decreased further, and increased tubule formation (arrows) from the CDRs is seen. EGFR-GFP spots away from the CDRs (arrowheads) appear. This indicates that EGFR-GFP could be moving from the CDRs to other cell regions. Referenced from (68).

Chapter 2

Investigating Circular Dorsal Ruffles through Varying Substrate Stiffness and Mathematical Modeling

The findings in this work have been published in the Biophysical Journal (105).

2.1 Introduction

Although CDRs have been long observed in cells (63, 69, 70), little is known about the mechanism of their formation. It has been observed that stress fibers that formed in fibroblasts seeded on fibronectin substrates disappeared in the vicinity of CDR formation (13, 71). This suggests an antagonistic relationship between stress fibers and CDRs that could be a result of interactions among signaling proteins known to be involved in growth factor stimulated motility and stress fiber formation, such as Rac and Rho (72, 73).

Because stress fibers formation has been shown to be modulated by substrate stiffness (74, 75), the apparent involvement of stress fibers in the generation of CDRs suggests that

substrate stiffness could be a mode of control of CDR dynamics. However, in most of the studies on CDRs, cells are cultured on glass substrates (57). In this article, we quantitatively investigate the effect of varying stiffnesses on the dynamic properties of CDRs, such as their lifetimes and sizes. In addition, we examine the mechanisms of formation of CDRs through the use of mathematical models to explain the changes in the CDR dynamics, both numerically and analytically.

We found that increasing substrate stiffness increased the lifetime of the CDRs. We developed a mathematical model of the signaling pathways involved in CDR formation to provide insight into this lifetime and size dependence that is linked to substrate stiffness via Rac-Rho antagonism. From the model, increasing stiffness raised mDia1-nucleated stress fiber formation due to Rho activation. The increased stress fibers present increased replenishment of the G-actin pool, therefore prolonging Arp2/3-nucleated CDR formation due to Rac activation. Negative feedback by WAVE-related RacGAP on Rac explained how CDR actin propagates as an excitable wave, much like wave propagation in other excitable medium, e.g., nerve signal transmission.

2.2 Materials and Methods

2.2.1 Preparation and characterization of elastic substrates

By varying the base/curing agent ratio in PDMS (Sylgard 184; Dow Corning, Midland, MI), the resulting elastic modulus (76, 77) can be modified by changing the ratio of the cross-linking chains. Young's modulus values of 20, 50, 250, and 1800 kPa were obtained using ratios

of 60:1, 50:1, 30:1, and 10:1 silicone elastomer base/curing agent, respectively. The mixtures were cultured in tissue culture plates and degassed under vacuum to remove any bubbles before curing overnight at 60 ºC. Cells were seeded on these three different elastomeric substrates as well as on glass substrates as a control. Characterization of the PDMS substrates was done using a tensile test (78–80). The flexibility of PDMS substrates with different base/curing agent ratios was determined by stretching sheets with dimensions of 100 mm × 20 mm × 1 mm with a known force F. The elastic modulus was subsequently calculated according to $E = (F/A)/(\Delta l/l)$, where A is the cross-sectional area of the sheet, l and Δl are the original length and change in length of the sheet in the direction of the applied force, respectively.

2.2.2 Cell Culture

To prepare PDMS substrates for cell culture, the surfaces were first sterilized using ethyl alcohol (190 proof, 95%, ACS/USP grade, No. 111USP190; PHARMCO-AAPER, Brookfield, CT). Phosphate-buffered saline (PBS, No. BP399-500; Fisher Scientific International, Hampton, NH) at a 10× solution was diluted to 1× with deionized water, filtered, and used as a buffer solution. The PDMS substrates were coated with fibronectin (10 mg/mL PBS, No. 39410; BD Biosciences, San Jose, CA) for 60 min. NIH 3T3 fibroblasts (National Institutes of Health, Bethesda, MD) were washed once with PBS and then exposed to trypsin-ethylenediamine-tetraacetate (0.05%, No. 25300; Invitrogen, Carlsbad, CA) for 5 min to dissociate them from the tissue culture plates. The cells were then seeded onto the PDMS substrates and cultured at 37 ºC and 5% carbon dioxide in growth media consisting of Dulbecco's modified Eagle's medium supplemented with 10% calf serum, glutamine (0.3 mg/mL), streptomycin (100 mg/mL),

penicillin (100 U/mL), and 20 mM n-2-hydroxyethylpiperazine-n0-2-ethanesulfonic acid at a pH of 7.4. Cells were incubated for 24 h to allow them to attach and spread. The cell culture media was replaced with media supplemented with 0.2% calf serum to allow the cells to be serum-starved. A quantity of 30 ng/mL of recombinant PDGF-BB (Peprotec; Invitrogen) was added to each sample. A sample was prepared for each of the PDGF-BB stimulation time intervals (2.5 min, then 5–50 min at 5-min intervals), and for each of the four PDMS substrate stiffness values (20 kPa, 50 kPa, 250 kPa, and 1800 kPa), as well as on glass, before immediately fixing and staining them.

2.2.3 Fluorescent Staining and Visualization

To visualize the cytoskeletal structure of the cells using fluorescent immunostaining, the cells were fixed with 4% paraformaldehyde and treated with 0.1% Triton-X, followed by staining with 6 mM phalloidin-tetramethylrhodamine- mine B isothiocyanate (No. P1951; Sigma-Aldrich, St. Louis, MO) and DAPI (40,6-diamidino-2-phenylindole, dihydrochloride; 2 mg in 1 mL PBS, No. D21490; Invitrogen), which labeled the actin filaments and the nucleus, respectively. After incubating the cells with phalloidin and DAPI, they were mounted on glass coverslips with Fluoromount-G (No. 0100-01; Southern Biotech, Birmingham, AL). By using an inverted fluorescent microscope (Axiovert 200; Carl Zeiss, Oberkochen, Germany) with a 63× (1.4 NA) objective, the actin filaments and nucleus of the NIH 3T3 fibroblasts were imaged.

2.2.4 Data Analysis

The surface area of the plasma membrane enclosed by a CDR in the images was calculated using ImageJ software (National Institutes of Health). We traced the perimeter of a CDR in the images that were captured with our charge-coupled device camera, and determined the area by the pixels within the traced region. Through this approach, we also calculated the perimeter of the CDR, as well as the major and minor axis values of the best fit ellipsoid to the CDR, which is a function of ImageJ (National Institutes of Health). The persistence time of CDRs in cells cultured on a given substrate was based on the time interval after PDGF stimulation whereby the sample had no visible CDRs that could be identified.

2.3 Results and Discussion

2.3.1 CDR size is independent of substrate stiffness but CDR lifetime increases with substrate stiffness

The actin distribution in the cells before and after PDGF stimulation on different substrates is shown in **Fig. 2.1**. In the left column (**Fig. 2.1, A–E**), cells before PDGF stimulation contained stress fibers and do not appear to contain CDRs. However, the right column (**Fig. 2.1, F–J**) shows cells with CDRs forming 5 min after PDGF stimulation. The CDRs are actin ringlike structures, which cover a significant percentage of the projected area in an image of the entire cell. Along with the effects of substrate stiffness on the percentage of cells expressing CDRs (see the Supporting Material), we also examined the time dependence of CDR characteristics, and if this was affected by substrate stiffness. To quantify the dynamics of CDRs, their geometries

were monitored over time for substrates with controlled stiffnesses. A representative response is shown in **Fig. 2.2** for cells seeded on glass **(Fig. 2.2, A–C**) and 50 kPa substrate (**Fig. 2.2, D–F**) for times 10, 20, and 30 min after PDGF stimulation.

To quantify average CDR size, four parameters were used: 1) The average projected area enclosed by the CDRs (**Fig. 2.3A**); 2), the average ring perimeter (**Fig. 2.3B**); and 3) and 4), the average length of the major and the minor axes (**Fig. 2.3, C and D**, respectively), which was accomplished through fitting the shapes of the CDRs to an ellipsoid. A total of 30 CDRs were observed for each of three cell populations, for each substrate, and at each time interval. For all cases of cells seeded on substrates with different stiffnesses, including on glass, the average size of the CDRs quantified by the four parameters mentioned above increased quickly from 0 to 2.5 min. Between 2.5 and 20 min, the average size of the CDR rings showed no discernable differences between the cell populations on all four substrates with differing stiffnesses. After 20 min, the observed CDR size for all cell populations started to decline. No CDRs were detected for cell populations on the 20, 50, 250, and 1800 kPa substrates after 25, 35, 40, and 45 min, respectively. In addition, no CDRs were found in any of the cell populations seeded on glass substrates after 45 min. Although the maximum size of CDRs was not affected by substrate stiffness (as shown in **Fig. 2.3**), the lifetime of CDRs appeared to increase with increasing substrate stiffness.

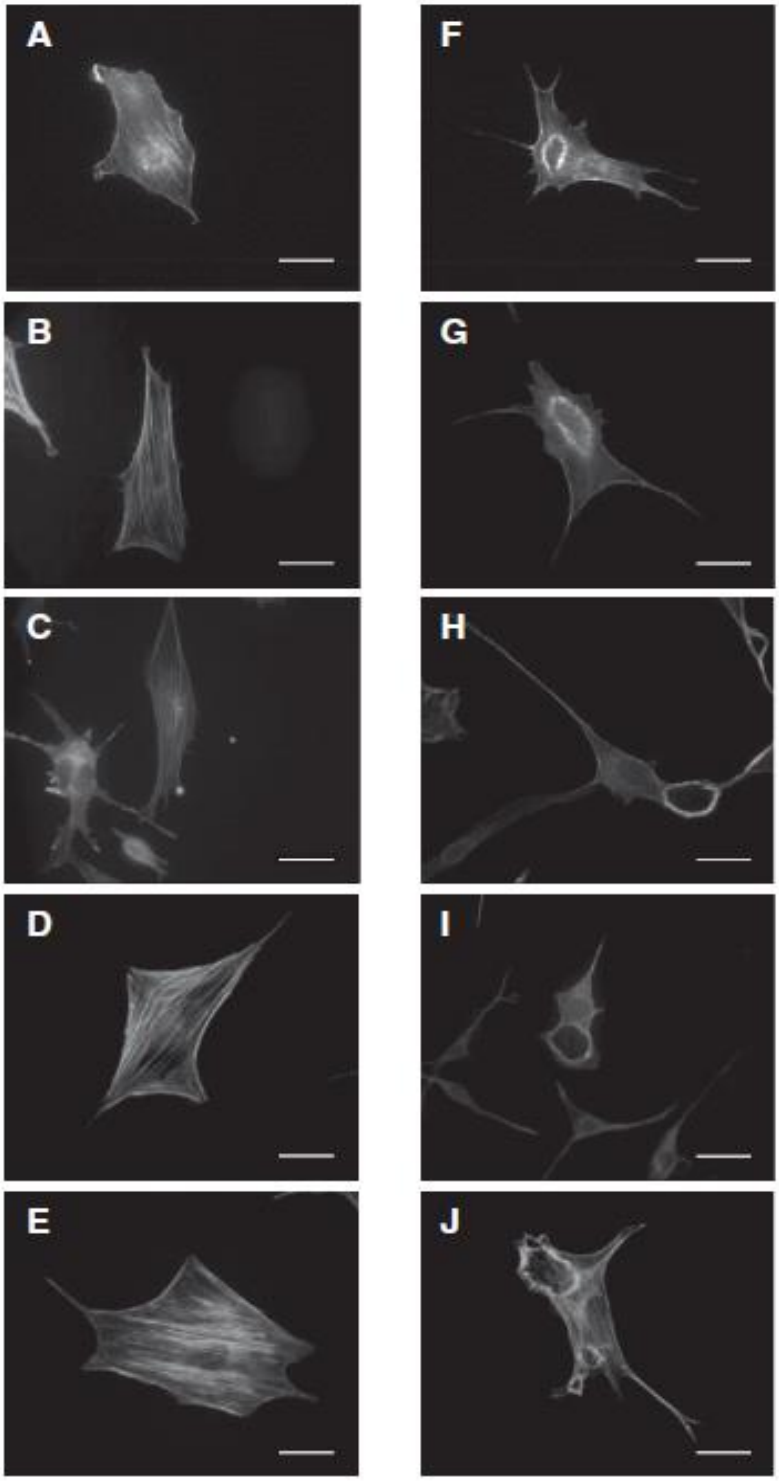

FIGURE 2.1: Stiffness-based comparison of CDRs formed in cells. Cells stained for F-actin before (A–E) and after (F–J) 5 min of PDGF stimulation.

Cells were seeded on substrates with stiffnesses of (A and F) 20 kPa, (B and G) 50 kPa, (C and H) 250 kPa, (D and I) 1800 kPa, and on (E and J) glass. (Bars) 10 µm.

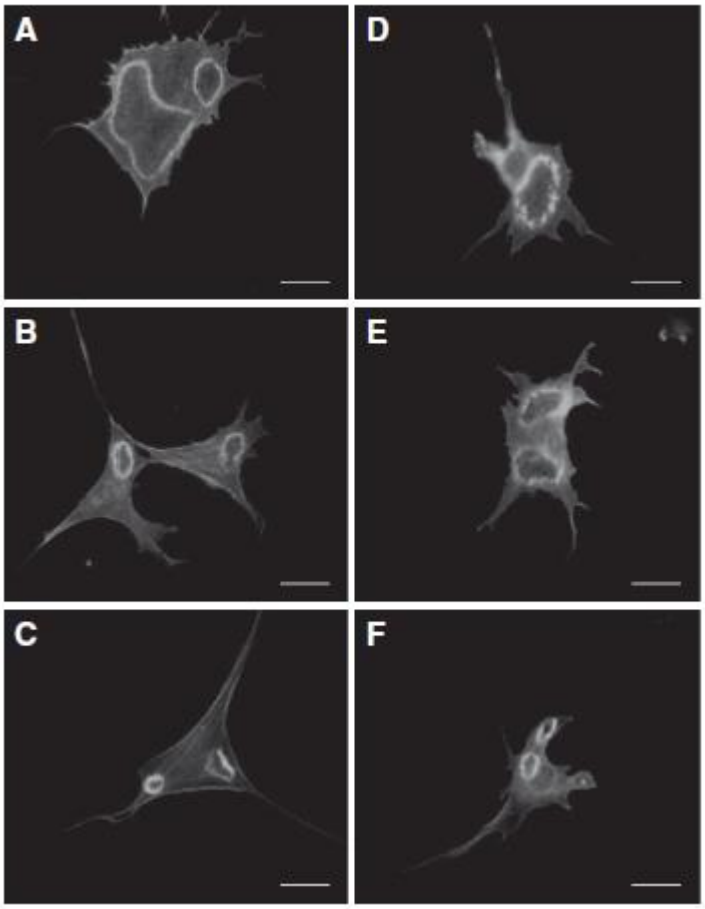

FIGURE 2.2: Time-based comparison of CDRs formed in cells seeded on (A–C) glass and on (D–F) 50 kPa PDMS substrates. The CDRs shown were taken of cells that had undergone (A and D) 10, (B and E) 20, and (C and F) 30 min of PDGF stimulation. (Bars) 10 µm.

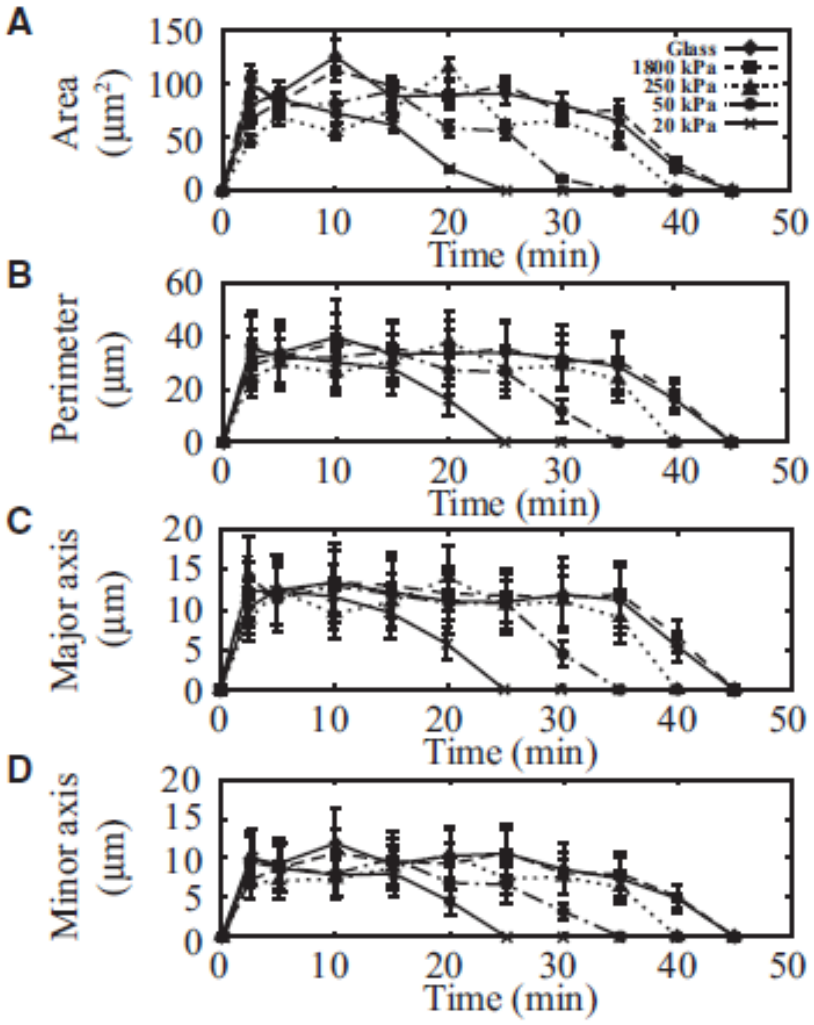

FIGURE 2.3: Quantification of the size of CDRs observed in cells. The (A) area, (B) perimeter and (C) major and as well as (D) minor axes of the best fit ellipsoid to the CDRs are shown. (n = 3.) (Bars) One standard error.

To understand the dependence of the size and lifetime of CDRs on substrate stiffness, we constructed a mathematical model of the signaling cascade that has been suggested to be involved in CDR formation under PDGF stimulation. This signaling cascade is summarized in **Fig. 2.4**. Past literature shows that upon PDGF stimulation, the phosphatidylinositol 3-kinase is activated that phosphorylates phosphatidylinositol (4,5)-bisphosphate on the plasma membrane,

thus forming phosphatidylinositol (3,4,5)-trisphosphate (PIP3) (81). This causes the Rac guanine nucleotide exchange factor (RacGEF) to localize to the membrane, which promotes the activation of the small GTPase Rac (82). Excessive PIP3 formation is checked by PTEN formation (83). Activated Rac binds to the WAVE1 complex, resulting in the dissociation of theWAVE1 complex (84, 85), rendering the WAVE1 protein available for binding with Arp2/3 (86), which promotes the nucleation of actin filaments, leading to generation of actin filaments close to the membrane. The activation of Rac can be regulated by RacGAPs. Studies have demonstrated the existence of RacGAPs that can bind to WAVE associated proteins, such as the 3BP-1 (which can bind to Abl, a protein in the WAVE1 complex) (87, 88).

Therefore, we suggest that the activation of a RacGAP that can bind toWAVE1, which we will refer to as ‘‘WGAP’’ in this article, provides a feedback mechanism to prevent the overactivation of Rac, which we will show later is required for the ringlike structure of CDRs. A specific example of WGAP is the WAVE-associated RacGAP found in neurons (89). Rac can also be regulated by and, in turn, regulates the stress fiber promoting small GTPase, Rho. Activated Rac binds and activates p190B Rho GTPase-activating protein (RhoGAP), leading to a reduction in Rho activity (90). Activated Rho, on the other hand, can be an antagonist to Rac by activation of the Rho-associated protein kinase (ROCK), which causes the activation of the RacGAP, FilGAP (91). Activated Rho is also known to encourage the formation of stress fibers at focal adhesions by 1), the activation of the Rho-associated protein kinase (ROCK), which increases phosphorylation of myosin light chains by the inactivation of myosin light chain phosphatase, and reduces levels of activated cofilin, both of which preserves the stress fibers formed at focal adhesions, and 2), the activation of mDia1, which is required for the nucleation of stress fibers (72, 92). Increased activation of Rho can be a result of increased phosphorylation

of the focal adhesion kinase (FAK), which activates the RhoGEF, p190RhoGEF (93), which has been observed in cells seeded on stiffer substrates (94, 95). This would also result in an increase in the initial amount of stress fibers before PDGF stimulation. This suggests that increasing the substrate stiffness would result in an increase in the amount of stress fibers before the cells were subjected to PDGF stimulation. An analysis of the ratio of F-actin to the total amount of F-actin and G-actin in the cells before PDGF stimulation showed that there was indeed an increase in the ratio of F-actin as the substrate stiffness was increased.

These interactions can be written in the form of mass action and Michaelis-Menten kinetics to form a set of coupled ordinary differential equations. In addition, we assume that these interactions occur in three separate noninteracting compartments: extracellular, membrane, and cytosolic. Within each compartment, the individual protein species can diffuse. Certain proteins, when activated, become bound/unbound from the membrane and take on the diffusive behavior of proteins in the membrane compartment (namely, phosphatidylinositol-3 kinase, PTEN, Rac- GEF, Rac, WAVE1, WGAP, RhoGAP, Arp2/3, and F-actin that make up the stress fibers and CDR actin). Therefore, with the inclusion of compartments and protein diffusion, our mathematical model comprises a set of coupled partial differential equations. Because the CDRs tend to take on a circular shape, we assume azimuthal symmetry and solve our system in the radial dimension only, using the region of PDGF receptor activation as the origin. The equations were solved in MATLAB (The MathWorks, Natick, MA) using the PDE solver pdepe, which discretizes the equations and evolves the functions explicitly.

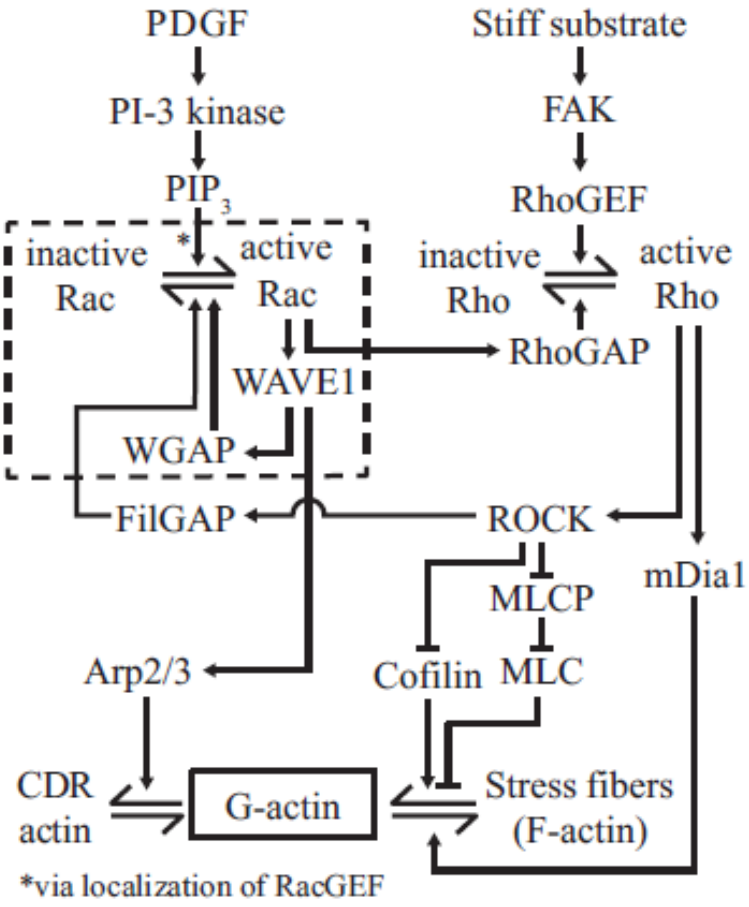

FIGURE 2.4: Summary of events leading up to CDR formation from PDGF stimulation for generation of the complete model. The reduced model is constructed from the events (enclosed within the dashes). References for these events are provided in the text.

2.3.2 Rac-Rho antagonism tunes the level of actin available for stress fibers and CDRs

There is evidence that increasing substrate stiffness can raise the amount of active FAK (94, 95). Because FAK is involved in the formation of stress fibers that are composed of actin, we propose that the modulation of CDR lifetimes by the substrate stiffness occurs through alteration of FAK concentration in the cell. Before PDGF stimulation, the spreading of the cell and thus FAK activation results in the activation of Rho that, via the activation of ROCK, leads to the activation of RacGAP. Therefore, activated Rho generates the inactivation of Rac. Because active Rho leads to downstream activation of mDia1 and active Rac leads to downstream activation of Arp2/3, we see the presence of mDia1-nucleated stress fiber formation and absence of Arp2/3-nucleated CDR before stimulation, as shown in **Fig. 2.1**, **A–E**. However, upon addition of PDGF, Rac gets activated and causes the downstream activation of RhoGAP, leading to the inactivation of Rho. This causes the loss of mDia1-nucleated stress fibers formation and increase in Arp2/3-nucleated CDR formation. By increasing the substrate stiffness, there is heightened FAK activation, causing increased stress fiber formation before PDGF stimulation.

Once stimulated by PDGF, the stress fibers dissociate and the high amount of stress fibers initially present leads to increased replenishing of the G-actin pool, therefore effectively increasing the lifetime of the CDR that draws actin from the G-actin pool. The results from solving the mathematical model using different amounts of FAK are shown in **Fig. 2.5**. In **Fig. 2.5A**, the size and lifetime of CDRs are shown for different concentrations of activated focal adhesion kinase (FAK), whereas **Fig. 2.5, B and C**, depicts the distribution of CDR versus time for two different concentrations of FAK. As mentioned previously, because activated FAK has been shown to increase with substrate stiffness (90) that leads to increased stress fiber formation before PDGF stimulation, the increase in lifetime of CDRs as the FAK concentration is raised (as

shown in **Fig. 2.5A**) is representative of increased CDR lifetime as substrate stiffness is raised. This also agrees with the experimental results. This suggests that CDRs and stress fibers can be used as markers to observe the antagonism between Rac and Rho that governs the competition between the two types of actin: Arp2/3-nucleated actin and mDia1-nucleated actin.

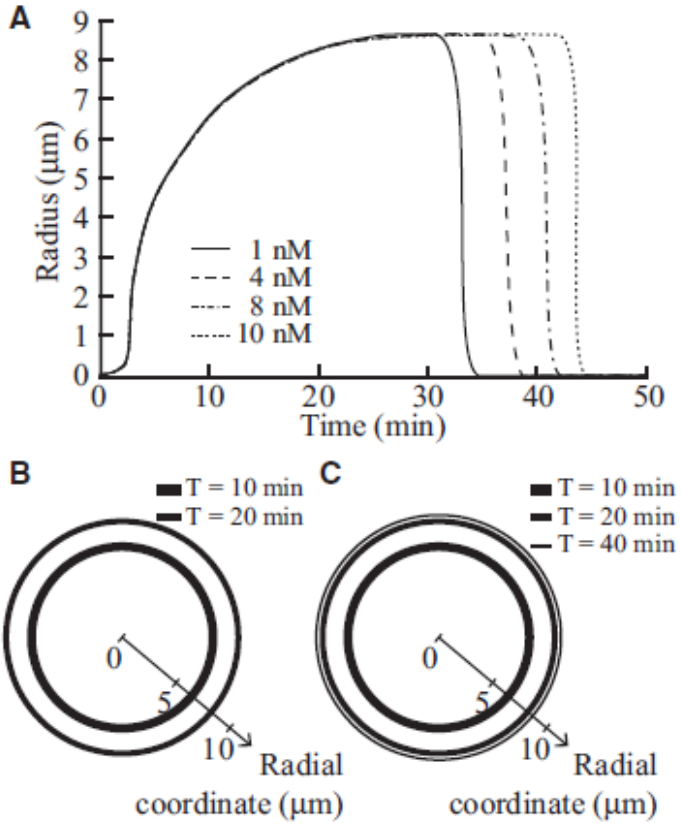

FIGURE 2.5: Simulations results for the effect of FAK concentration on CDRs. (A) Variation of radius of CDRs with time for different FAK concentrations. (B) CDR formation at T = 10 min and 20 min for [FAK] = 1 nM. Note that no CDR is observed at T = 40 min. (C) CDR formation at T = 10 min, 20 min, and 40 min for [FAK] = 10 nM.

2.3.3 Negative feedback by WGAP results in actin ring instead of actin patch formation

Our simulations, with the initial condition of PDGF being introduced uniformly throughout but that the PDGF receptors are assumed to occupy a small localized patch at the origin, led to rapid phosphorylation of PIP_2 to PIP_3 that propagated away from the point of stimulation gradually, due to the low diffusivity of membrane elements, while maintaining the location of its peak at the origin. The localization of PIP_3 close to the front of a cell subjected to a uniform PDGF stimulation has been shown experimentally (96), which agrees with our simulation results. Activated Rac that localized to PIP_3, however, formed a peak that traveled away from the origin quickly and attained a stable spatial location before moving toward the origin again while decaying at the same time, which led to CDR actin behaving in the same manner. This would resemble the generation of a CDR from a point into its ringlike structure. The mathematical model revealed that formation of the ringlike structure was a result of the negative feedback provided by WGAP. The high amounts of WAVE1 activated by the locally stimulated PDGF receptor is likely to have caused a spike in activated WGAP, resulting in a decrease in activated Rac at the site of stimulation. This can be observed in **Fig. 2.6, E–H**, which showed a growing region of actin centered at the origin that decreased in height at later times, in contrast with the ring generation in the presence of WGAP, represented in **Fig. 2.6, A–C**, as single peaks centered away from the origin (note that in **Fig. 2.6D**, no peak is seen because the CDR has completely decayed).

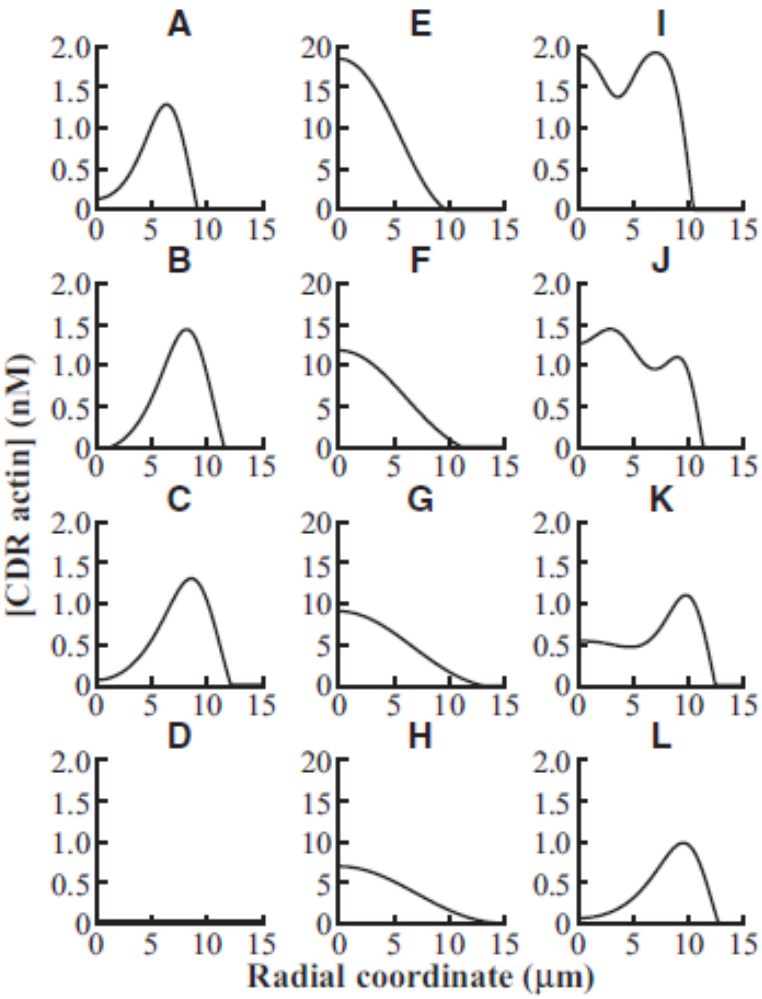

FIGURE 2.6: Simulation results for the effect of WGAP and multiple PDGF receptor aggregates on CDRs. The variations of [CDR actin] in radial space in the presence of WGAP at (A) T = 10 min, (B) T = 20 min, (C) T = 30 min, and (D) T = 40 min after PDGF receptor activation at the origin are shown. The single peak in [CDR actin] is seen to travel away from the origin, illustrating a growing ring of CDR actin. In the absence of WGAP, similar plots are shown in panels E–H. Note that without WGAP, the peak amount of [CDR actin] is elevated and centered at the origin, which translates to a patch of CDR actin that grows in size. Lastly, the variations of [CDR actin] after PDGF receptor activation at the origin and at radial coordinate of 7.5 mm is shown at (I) T = 2 min, (J) T = 4 min, (K) T = 8 min, and (L) T = 20 min. Note that only one peak is seen at later times, indicating that only one CDR actin ring is formed.

2.3.4 Multiple CDRs spread and merge into a single CDR

To study the scenario when two or more CDRs interact, we repeated the simulations but now with two localized patches of PDGF receptors to initiate two CDRs. The individual CDRs grow rapidly and merge to form a single CDR. A representative response is shown in **Fig. 2.6, I–L**. This can be understood as a phenomenon in excitable media (see below), where the passing wave leaves behind a refractory region in which a subsequent activation is not possible (91). Thus, as two distinct CDRs approach each other, they annihilate each other because neither one can cross the refractory region behind the leading edge of the approaching wave, where the Rac recently became inactive and cannot yet activate. Thus, multiple CDRs would converge to form one large CDR instead of forming a chain of intersecting CDRs. In fact, our imaging results presented no occurrences of intersecting CDRs found.

2.3.5 CDR actin propagates as an excitable wave

Finally, we propose that Rac and WGAP play key roles in the formation of CDRs and thus, we can write down a reduced model to describe the interaction between Rac and WGAP. The inactivation of Rac by WGAP is paralleled to an enzymatic reaction that requires the activation of WAVE1 and is in turn activated by Rac. Close examination of the results of the complex model shows us that the concentration of activated WAVE1 changes proportionately with activated Rac. Because the inactivation of Rac by WGAP requires both active Rac and active WAVE1, this reaction can be simplified to be a cooperative enzymatic reaction with a Hill coefficient of two by substituting WAVE1 with active Rac. Here, we use the Hill's equation to

phenomenologically represent the inactivation of Rac by WGAP. The activation of WGAP can be simplified to a Michaelis- Menten-type reaction. At the same time, Rac and WGAP can diffuse as membrane-bound proteins. Therefore,

$$\frac{\partial X}{\partial T} = D\frac{1}{R}\frac{\partial}{\partial R}\left(R\frac{\partial X}{\partial R}\right) + \frac{V_1(X_t - X)}{K_{m1} + X_t - X} - \frac{V_2 X^2 Y}{K_{m2}^2 + X^2},$$

$$\frac{\partial Y}{\partial T} = D\frac{1}{R}\frac{\partial}{\partial R}\left(R\frac{\partial Y}{\partial R}\right) + \frac{V_3 X(Y_t - Y)}{K_{m3} + Y_t - Y},$$

where T and R represent the time and radial dimensions, and X and Y represent active Rac and WGAP, respectively. The parameters V_1 and K_{m1} characterize the enzymatic activation of Rac after PDGF stimulation, V_2 and K_{m2} characterize the enzymatic deactivation of Rac by WGAP, V_3 and K_{m3} characterize the enzymatic activation of WGAP after Rac activation, X_t and Y_t denote the total Rac and WGAP present, and D represents the diffusion coefficients of Rac and WGAP, taken to be the same in this study. By introducing nondimensional quantities

$$x = \frac{X}{X_t},\ y = \frac{Y}{X_t},\ t = V_3 T,$$

$$r = \sqrt{\frac{V_3}{D}}R,$$

we obtain

$$\frac{\partial x}{\partial t} = \frac{1}{r}\frac{\partial}{\partial r}\left(r\frac{\partial x}{\partial r}\right) + \frac{1}{V_3}F(x, y), \tag{1}$$

$$\frac{\partial y}{\partial t} = \frac{1}{r}\frac{\partial}{\partial r}\left(r\frac{\partial y}{\partial r}\right) + G(x, y), \tag{2}$$

where

$$F(x,y) = \frac{v_1(1-x)}{k_{m1}+1-x} - \frac{v_2 x^2 y}{k_{m2}^2 + x^2},$$

$$G(x,y) = \frac{x(y_t - y)}{k_{m3} + y_t - y}.$$

Here,

$$k_{m1} = \frac{K_{m1}}{X_t}, \; k_{m2} = \frac{K_{m2}}{X_t}, \quad k_{m3} = \frac{K_{m3}}{X_t},$$
$$v_1 = \frac{V_1}{X_t}, \quad v_2 = V_2, \text{ and } y_t = \frac{Y_t}{X_t}.$$

In this reduced model, we assume that actin concentration will be proportional to Rac concentration and hence to *x*. Numerical analysis of this reduced model shows that *x* forms a ring that grows and shrinks in time, observed as a single peak in CDR actin concentration that moves radially away from the origin then toward the origin. This justifies the choice of Rac and WGAP as key proteins responsible for the ringlike structure and the dynamics of CDRs.

A phase diagram depicting the kinetics of the reduced model with equal values for X_t and Y_t (such that $y_t = 1$) and suitable parameters in a homogenous solution such that diffusion can be neglected is shown in **Fig. 2.7A**. Using standard linear stability analysis of the system, we were able to show that the only steady state of the system ($x \approx 0$ and $y = y_t$) is stable to perturbations. This can also be observed in **Fig. 2.7A**, where all possible paths lead back to the steady state. Using a small value of V_3, we can create an excitable system that displays two types of behavior depending on the magnitude of the deviation of WGAP from its steady-state value, as explained in the following paragraphs.

Firstly, when WGAP deviates slightly from its steady-state value regardless of the amount of Rac present, the system quickly returns to its stable steady state as can be observed in **Fig. 2.7A** by the solid path. This indicates that upon attaining a state of high WGAP and low Rac (usually in the later part of PDGF stimulation), disturbances to the system caused by increasing Rac via additional PDGF stimulation would not result in CDR formation because Rac is quickly inactivated.

Secondly, a large deviation in WGAP from its steady state, however, can trigger a rapid growth of Rac whereas WGAP remains almost constant. This is reminiscent of PDGF stimulation, where the cell begins with a low value of WGAP and Rac (achieved by the absence of PDGF, where V_1 is zero, resulting in no formation of Rac or WGAP). The rapid growth of Rac is halted when the amount of Rac approaches the value where $F(x,y)$ is close to zero, therefore starting the slow phase of the kinetics, where Rac remains almost constant whereas WGAP increases slowly. The next fast phase of the kinetics is initiated when WGAP is suitably high, once again causing Rac to evolve much faster than WGAP. The plot of Rac and WGAP versus time is depicted in **Fig. 2.7B** for the path traced out by the dashed curve in **Fig. 2.7A**. This behavior is observed when the initial fraction of activated WGAP is below the ratio v_1/v_2; in this case, the ratio was 0.5. In a heterogeneous solution, however, the presence of diffusion results in the possibility of a traveling pulse solution. To illustrate this, we introduce a moving frame, denoted by $\xi = r - ct$, such that at high values of r, the equations are transformed to

$$\frac{\partial^2 x}{\partial \xi^2} + c\frac{\partial x}{\partial \xi} + \frac{1}{v_3}F(x,y) = 0, \tag{3}$$

$$\frac{\partial^2 y}{\partial \xi^2} + c\frac{\partial y}{\partial \xi} + G(x,y) = 0. \tag{4}$$

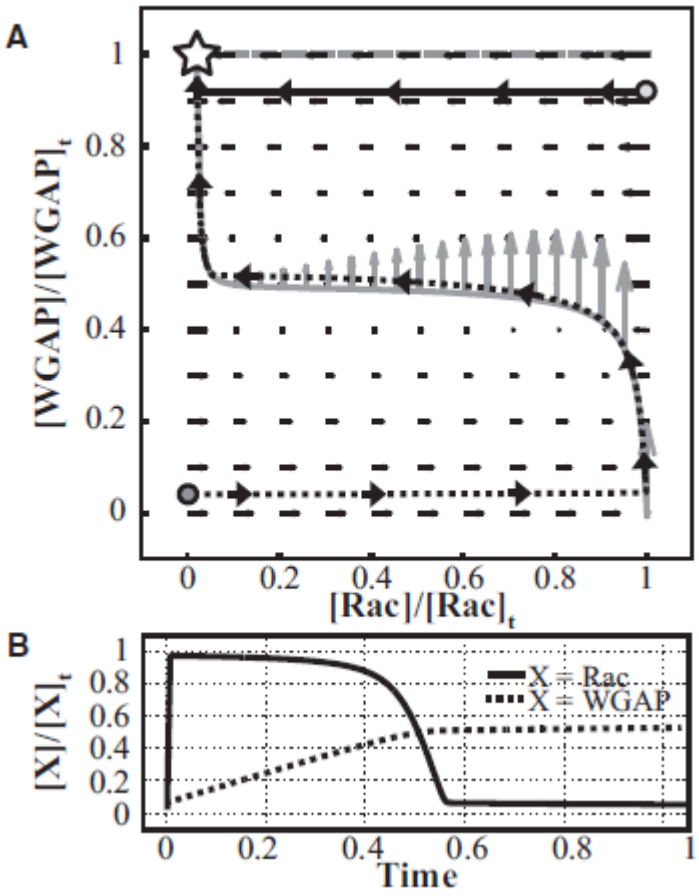

FIGURE 2.7: Phase diagram and time plots for Rac and WGAP, depicting the variation of Rac and WGAP with each other and in time, respectively. (A) Nullclines of $F(x,y) = 0$ (shaded line) and $G(x,y) = 0$ in (dashed line). (Arrows) Dynamics of Rac and WGAP (shaded arrows on the $F(x,y) = 0$ nullcline are scaled to 1000 times of the solid arrows). The stable steady state is indicated (star). (Solid curve) The rapid return of Rac and WGAP (from their values at the light-shaded dot) to their steady-state values when WGAP is only slightly decreased from its steady-state value. (Dashed curve) A typical course of excursion upon PDGF stimulation, where active Rac and active WGAP are both low, as indicated (dark-shaded dot). (B) Variation of Rac and WGAP with dimensionless time (with an initial state equivalent to that represented by the dark-shaded dot in panel A). WGAP attains the value of $[WGAP]_t$ at a much later time due to the slow dynamics of WGAP.

Rac and WGAP are now functions of x, with c denoting the velocity of the moving frame. Therefore, as seen in **Fig. 2.7B**, Rac takes on largely two values during its evolution: $x_+ \approx Rac_t$ and $x_- \approx 0$. This implies that should a nonuniform solution be created for Rac, it would resemble a front that serves as an interface between the two regions. With a suitable choice of c, we can create a moving frame that travels with the moving front such that the front appears stationary in the moving frame. As the value of Rac is almost stationary in the slow regions (which, in these experiments, is most of the time in the evolution of Rac and WGAP), this velocity of the moving frame c, and therefore the moving front, is dependent on the amount of WGAP present. Moving out of the moving frame, this implies that a front/ pulse in Rac created from x_+ and x_- would grow, then shrink, as the value of WGAP changes with time. Thus, the above analysis shows that the growth and decay of CDR actin can be explained as pulse propagation in an excitable media, in which a wave is able to propagate in a nonlinear dynamical system, which is the excitable media. The finding that through the modification of the underlying substrate stiffness of cell populations, CDR kinetics after cell stimulation with PDGF can be controlled, has implications that are related to the functionalities of CDRs within a cell. For example, because it has been hypothesized that CDRs aid in cell migration (61, 62) through large-scale actin network reorganization, reduced CDR kinetics could mean that the actin network is reorganized less quickly, which could affect cell motility potential. Also, because cells that exhibit CDRs might have a role to play in macropinocytosis (65, 66), differing CDR kinetics could affect the rate at which this process occurs. Because CDR formation might aid in RTK sequestration and internalization after cell stimulation with ligands (67), reduced CDR dynamics would likely result in a reduced rate of these processes.

2.3.6 More cells exhibit CDRs when seeded on softer substrates

The percentage of cells in a sample which exhibited CDRs in a cell population was calculated by manually observing at least 500 cells in the given sample and counting the number of cells which had CDRs, and taking it as a percentage of the total number of observed cells in the sample. We found that by changing the substrate stiffness, we were able to modify the percentage of cells exhibiting CDRs, with more cells showing CDRs when seeded on less stiff substrates. This is quantified in **Fig. 2.8** with a maximum of cells expressing CDRs within 5 min of stimulation and then slowly returning back to no CDR expression within 45 min. Based on observation of the signalling pathway depicted in **Fig. 2.4**, we postulate that increasing the substrate stiffness leads to an increase in FAK concentration which might hinder the initial dissociation of stress fibers which have been shown to accompany CDR formation, therefore reducing the chance of CDR formation in cells. Yet, once CDR formation is achieved, the lifetime of CDR is prolonged by the increased replenishing of actin monomers resulting from heightened stress fiber formation on stiffer substrates prior to PDGF stimulation.

2.3.7 More cells exhibit CDRs when seeded on softer substrates

Cells were costained for G-actin and F-actin with DNase I (Alexa Fluor 488; 2 μM) and phalloidin (Alexa Fluor 568; 6 μM) respectively for 60 min and imaged using an inverted fluorescent microscope (Zeiss, Axiovert 200) with a 63x (1.4 Numerical Aperture) objective. Using ImageJ, the ratio of the F-actin fluorescence intensity to the total actin fluorescence

intensity (F-actin and G-actin combined) in each cell was calculated. This ratio was averaged over 50 cells seeded on each substrate stiffness and the results are plotted in **Fig. 2.9**. The results show that increasing the substrate stiffness increases the ratio of actin incorporated in F-actin before PDGF stimulation.

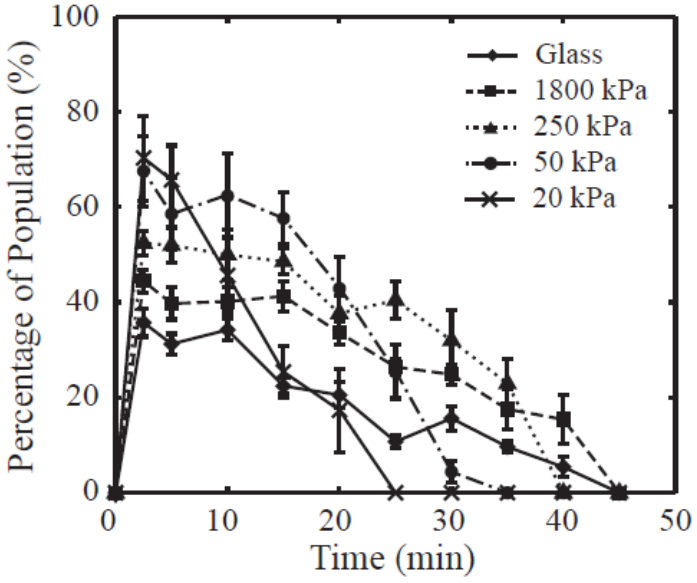

FIGURE 2.8: Percentage of cell population exhibiting CDRs versus time for PDMS substrates of different elasticities and glass substrates. (n=3). The bars denote one standard error.

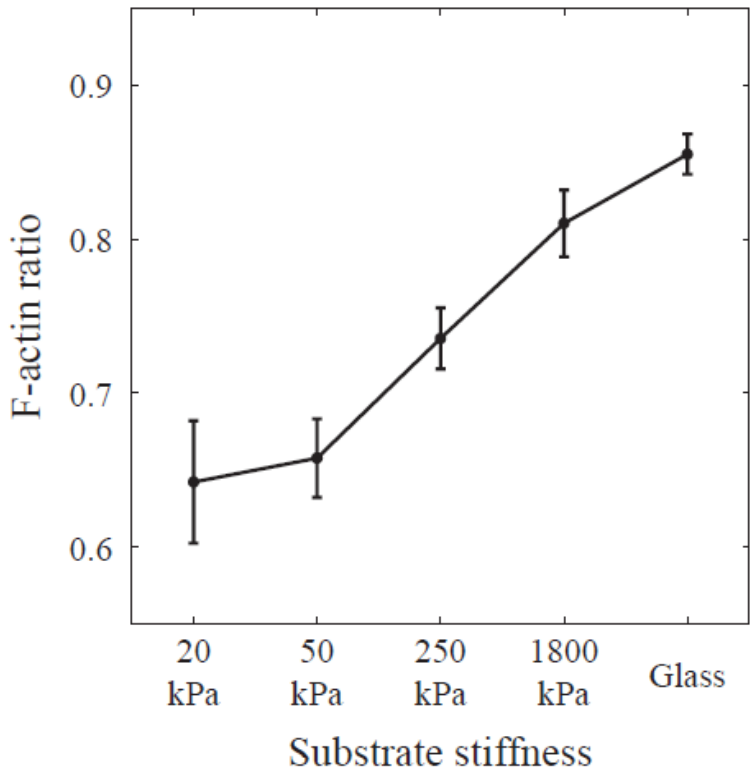

FIGURE 2.9: F-actin ratio for varying substrate stiffnesses. The bars denote one standard error.

2.3.8 Full mathematical model of proteins/lipids

This section documents the reactions between the different protein and lipid species involved in a potential pathway activated by the PDGF. The reactions are then converted into mathematical equations (referred to as reaction terms). The species are evolved under the effects of diffusion and the reaction terms in MATLAB (The Mathworks, Inc., Natick, MA). Cpt : Compartment; Rxn : Reaction. The subscripts a, c, and d refer to the active, cytosolic (inactive) and dorsal ruffle associated forms of the proteins respectively. Note that k_{-8} is a function of active myosin light chain and coflin concentrations.

Table 1: Abbreviations for protein and lipid species involved in the mathematical model.

Abbreviation	Definition
PDGF	Platelet-derived growth factor
PDGFR	Platelet-derived growth factor receptor
PI-3K	Phosphatidylinositol 3-kinase
PIP_2	Phosphatidylinositol (4,5)-bisphosphate
PIP_3	Phosphatidylinositol (3,4,5)-bisphosphate
RacGEF	Rac guanine exchange factor
RacGAP	Rac GTPase activating protein
RhoGEF	Rho guanine exchange factor
RhoGAP	Rho GTPase activating protein
ROCK	Rho-associated protein kinase
LIMK	LIM kinase
Cof	Cofilin
MLC	Myosin light chain
MLCP	Myosin light chain phosphatase
MLCP-P	Phosphorylated (inactive) myosin light chain phosphatase
MLCK	Myosin light chain kinase
F-actin	Stress fiber actin
G-actin	Monomeric actin
D-actin	Dorsal ruffle actin

Table 2: Reactions for protein and lipid species involved in the mathematical model.

$$PDGF_2 + PDGFR \underset{k_{-1}}{\overset{k_1}{\rightleftharpoons}} PDGF_2\text{–}PDGFR \quad (1)$$

$$2PDGF_2\text{–}PDGFR \underset{k_{-2}}{\overset{k_2}{\rightleftharpoons}} PDGFR_a \quad (2)$$

$$PDGFR_a + PI\text{–}3K_c \xrightarrow{1} PDGFR_a + PI\text{–}3K_a \quad (3)$$

$$PI\text{–}3K_a + PIP_2 \xrightarrow{2} PI\text{–}3K_a + PIP_3 \quad (4)$$

$$PIP_2 + PTEN_c \underset{k_{-3}}{\overset{k_3}{\rightleftharpoons}} PTEN_a \quad (5)$$

$$PTEN_a + PIP_3 \xrightarrow{3} PTEN_a + PIP_2 \quad (6)$$

$$PIP_3 + RacGEF_c \underset{k_{-4}}{\overset{k_4}{\rightleftharpoons}} RacGEF_a \quad (7)$$

$$RacGEF_a + Rac_c \xrightarrow{4} RacGEF_a + Rac_a \quad (8)$$

$$WAVE1_c + Rac_a \underset{k_{-5}}{\overset{k_5}{\rightleftharpoons}} WAVE1_a \quad (9)$$

$$WAVE1_a + WGAP_c \xrightarrow{5} WAVE1_a + WGAP_a \quad (10)$$

$$WGAP_a + Rac_a \xrightarrow{6} WGAP_a + Rac_c \quad (11)$$

$$RhoA_a + ROCK \underset{k_{-6}}{\overset{k_6}{\rightleftharpoons}} ROCK_a \quad (12)$$

$$ROCK_a + LIMK_c \xrightarrow{7} ROCK_a + LIMK_a \quad (13)$$

$$LIMK_a + Cof_a \xrightarrow{8} LIMK_a + Cof_c \quad (14)$$

$$RhoA_a + mDia_c \underset{k_{-7}}{\overset{k_7}{\rightleftharpoons}} mDia_a \quad (15)$$

$$G\text{–}actin + mDia_a \underset{k_{-8}}{\overset{k_8}{\rightleftharpoons}} F\text{–}actin \quad (16)$$

$$WAVE1_a + Arp2/3 \underset{k_{-9}}{\overset{k_9}{\rightleftharpoons}} Arp2/3_d \quad (17)$$

$$Arp2/3_d + G\text{–}actin \underset{k_{-10}}{\overset{k_{10}}{\rightleftharpoons}} D\text{–}actin \quad (18)$$

$$ROCK_a + MLCP \xrightarrow{9} ROCK_a + MLCP\text{–}P \quad (19)$$

$$MLCP + MLC_a \xrightarrow{10} MLCP + MLC_c \quad (20)$$

$$MLCK + MLC_c \xrightarrow{11} MLCK + MLC_a \quad (21)$$

$$FAK_{pi} + RhoGEF \underset{k_{-11}}{\overset{k_{11}}{\rightleftharpoons}} RhoGEF_a \quad (22)$$

$$RhoA_c + RhoGEF_a \xrightarrow{12} RhoA_a + RhoGEF_a \quad (23)$$

$$ROCK_a + RacGAP_c \xrightarrow{13} ROCK_a + RacGAP_a \quad (24)$$

$$RacGAP_a + Rac_a \xrightarrow{14} RacGAP_a + Rac_c \quad (25)$$

$$Rac_a + RhoGAP_c \underset{k_{-12}}{\overset{k_{12}}{\rightleftharpoons}} RhoGAP_a \quad (26)$$

$$RhoGAP_a + RhoA_a \xrightarrow{15} RhoGAP_a + RhoA_c \quad (27)$$

Table 3: Equations for protein and lipid species involved in the mathematical model.

No	Cpt	Name	Reaction terms
1	e	$PDGF_2$	$-k_1[PDGF_2][PDGFR] + k_{-1}[PDGF_2\text{–}PDGFR]$
2	m	PDGFR	$-k_1[PDGF_2][PDGFR] + k_{-1}[PDGF_2\text{–}PDGFR]$
3	m	$PDGF_2$–PDGFR	$k_1[PDGF_2][PDGFR] - k_{-1}[PDGF_2\text{–}PDGFR] - k_2[PDGF_2\text{–}PDGFR]^2 + k_{-2}[PDGFR_a]$
4	m	$PDGFR_a$	$k_2[PDGF_2\text{–}PDGFR]^2 - k_{-2}[PDGFR_a]$
5	c	PI–$3K_c$	$-\frac{k_{cat,1}[PDGFR_a][PI\text{–}3K_c]}{k_{m1} + [PI\text{–}3K_c]}$
6	m	PI–$3K_a$	$\frac{k_{cat,1}[PDGFR_a][PI\text{–}3K_c]}{k_{m1} + [PI\text{–}3K_c]}$
7	m	PIP_2	$-\frac{k_{cat,2}[PI\text{–}3K_a][PIP_2]}{k_{m2} + [PIP_2]} + \frac{k_{cat,3}[PTEN_a][PIP_3]}{k_{m3} + [PIP_3]} - k_3[PIP_2][PTEN_c] + k_{-3}[PTEN_a]$

8	m	PIP_3	$\frac{k_{cat,2}[PI\text{–}3K_a][PIP_2]}{k_{m2}+[PIP_2]} - \frac{k_{cat,3}[PTEN_a][PIP_3]}{k_{m3}+[PIP_3]} - k_4[PIP_3][RacGEF_c] + k_{-4}[RacGEF_a]$
9	c	$PTEN_c$	$-k_3[PIP_2][PTEN_c] + k_{-3}[PTEN_a]$
10	m	$PTEN_a$	$k_3[PIP_2][PTEN_c] - k_{-3}[PTEN_a]$
11	c	$RacGEF_c$	$-k_4[RacGEF_c][PIP_3] + k_{-4}[RacGEF_a]$
12	m	$RacGEF_a$	$k_4[RacGEF_c][PIP_3] - k_{-4}[RacGEF_a]$
13	c	Rac_c	$-\frac{k_{cat,4}[RacGEF_a][Rac_c]}{k_{m4}+[Rac_c]} + \frac{k_{cat,6}[WGAP_a][Rac_a]}{k_{m6}+[Rac_a]} + \frac{k_{cat,14}[RacGAP_a][Rac_a]}{k_{m14}+[Rac_a]}$
14	m	Rac_a	$\frac{k_{cat,4}[RacGEF_a][Rac_c]}{k_{m4}+[Rac_c]} - \frac{k_{cat,6}[WGAP_a][Rac_a]}{k_{m6}+[Rac_a]} - \frac{k_{cat,14}[RacGAP_a][Rac_a]}{k_{m14}+[Rac_a]} - k_5[WAVE1_c][Rac_a] + k_{-5}[WAVE1_a] - k_{12}[RhoGAP_c][Rac_a] + k_{-12}[RhoGAP_a]$
15	c	$WAVE1_c$	$-k_5[WAVE1_c][Rac_a] + k_{-5}[WAVE1_a]$
16	m	$WAVE1_a$	$k_5[WAVE1_c][Rac_a] - k_{-5}[WAVE1_a] - k_9[WAVE1_a][Arp2/3] + k_{-9}[Arp2/3_d]$
17	c	$WGAP_c$	$-\frac{k_{cat,5}[WAVE1_a][WGAP_c]}{k_{m5}+[WGAP_c]}$
18	m	$WGAP_a$	$\frac{k_{cat,5}[WAVE1_a][WGAP_c]}{k_{m5}+[WGAP_c]}$

19	c	RhoGAP$_c$	$-k_{12}[RhoGAP_c][Rac_a] + k_{-12}[RhoGAP_a]$
20	m	RhoGAP$_a$	$k_{12}[RhoGAP_c][Rac_a] - k_{-12}[RhoGAP_a]$
21	c	RhoA$_a$	$-\frac{k_{cat,15}[RhoGAP_a][RhoA_a]}{k_{m15}+[RhoA_a]} + \frac{k_{cat,12}[RhoGEF_a][RhoA_c]}{k_{m12}+[RhoA_c]} - k_6[RhoA_a][ROCK] + k_{-6}[ROCK_a] - k_7[RhoA_a][mDia_c] + k_{-7}[mDia_a]$
22	c	RhoA$_c$	$\frac{k_{cat,15}[RhoGAP_a][RhoA_a]}{k_{m15}+[RhoA_a]} - \frac{k_{cat,12}[RhoGEF_a][RhoA_c]}{k_{m12}+[RhoA_c]}$
23	c	ROCK	$-k_6[RhoA_a][ROCK] + k_{-6}[ROCK_a]$
24	c	ROCK$_a$	$k_6[RhoA_a][ROCK] - k_{-6}[ROCK_a]$
25	c	LIMK$_c$	$-\frac{k_{cat,7}[ROCK_a][LIMK_c]}{k_{m7}+[LIMK_c]}$
26	c	LIMK$_a$	$\frac{k_{cat,7}[ROCK_a][LIMK_c]}{k_{m7}+[LIMK_c]}$
27	c	Cof$_a$	$-\frac{k_{cat,8}[LIMK_a][Cof_a]}{k_{m8}+[Cof_a]}$
28	c	Cof$_c$	$\frac{k_{cat,8}[LIMK_a][Cof_a]}{k_{m8}+[Cof_a]}$
29	c	mDia$_c$	$-k_7[RhoA_a][mDia_c] + k_{-7}[mDia_a]$
30	c	mDia$_a$	$k_7[RhoA_a][mDia_c] - k_{-8}[mDia_a] - k_8[G\text{–}actin][mDia_a] + k_{-8}[F\text{–}actin]$
31	c	MLCP	$-\frac{k_{cat,9}[ROCK_a][MLCP]}{k_{m9}+[MLCP]}$

32	c	MLCP–P	$\frac{k_{cat,9}[ROCK_a][MLCP]}{k_{m9}+[MLCP]}$
33	c	MLC_a	$-\frac{k_{cat,10}[MLCP][MLC_a]}{k_{m10}+[MLC_a]}+\frac{k_{cat,11}[MLCK][MLC_c]}{k_{m11}+[MLC_c]}$
34	c	MLC_c	$\frac{k_{cat,10}[MLCP][MLC_a]}{k_{m10}+[MLC_a]}-\frac{k_{cat,11}[MLCK][MLC_c]}{k_{m11}+[MLC_c]}$
35	c	G–actin	$-k_8[G\text{–}actin][mDia_a] + k_{-8}[F\text{–}actin] - k_{10}[Arp2/3_d][G\text{–}actin]+k_{-10}[D\text{–}actin]$
36	m	F–actin	$k_8[G\text{–}actin][mDia_a]-k_{-8}[F\text{–}actin]$
37	m	D–actin	$k_{10}[Arp2/3_d][G\text{–}actin]-k_{-10}[D\text{–}actin]$
38	c	Arp2/3	$-k_9[WAVE1_a][Arp2/3]+k_{-9}[Arp2/3_d]$
39	m	$Arp2/3_d$	$k_9[WAVE1_a][Arp2/3] - k_{-9}[Arp2/3_d] - k_{10}[Arp2/3_d][G\text{–}actin]+k_{-10}[D\text{–}actin]$
40	c	RhoGEF	$-k_{11}[FAK_{pi}][RhoGEF]+k_{-11}[RhoGEF_a]$
41	c	$RhoGEF_a$	$k_{11}[FAK_{pi}][RhoGEF]-k_{-11}[RhoGEF_a]$
42	c	$RacGAP_c$	$-\frac{k_{cat,13}[ROCK_a][RacGAP_c]}{k_{m13}+[RacGAP_c]}$
43	c	$RacGAP_a$	$\frac{k_{cat,13}[ROCK_a][RacGAP_c]}{k_{m13}+[RacGAP_c]}$

Table 4: Parameters for equations involved in the mathematical model.

Rxn	Parameters	Values	References
1	k_1 , k_{-1}	0.7 nM^{-1} s^{-1} , 1.0 s^{-1}	Park et al (98)
2	k_2 , k_{-2}	0.122 μM^{-1} s^{-1} , 0.00122 s^{-1}	Park et al (98)
3	$k_{cat,1}$, k_{m1}	1.0 s^{-1} , 100 nM	Estimated
4	$k_{cat,2}$, k_{m2}	1.0 s^{-1} , 200 nM	Gamba et al (99)
			Naoki et al (100
5	k_3 , k_{-3}	50 μM^{-1} s^{-1} , 0.1 s^{-1}	Gamba et al (99)
6	$k_{cat,3}$, k_{m3}	0.5 s^{-1} , 200 nM	Gamba et al (99)
			Naoki et al (100)
7	k_4 , k_{-4}	5 μM^{-1} s^{-1} , 50 s^{-1}	Naoki et al (100)
8	$k_{cat,4}$, k_{m4}	1.0 s^{-1} , 100 nM	Naoki et al (100)
9	k_5 , k_{-5}	1 μM^{-1} s^{-1} , 1 s^{-1}	Estimated
10	$k_{cat,5}$, k_{m5}	1.0 s^{-1} , 100 nM	Estimated
11	$k_{cat,6}$, k_{m6}	0.1 s^{-1} , 10 nM	Naoki et al (100)
12	k_6 , k_{-6}	1 μM^{-1} s^{-1} , 1 s^{-1}	Estimated
13	$k_{cat,7}$, k_{m7}	2 s^{-1} , 3.1 μM	Turner et al (101)
14	$k_{cat,8}$, k_{m8}	1 s^{-1} , 1 μM	Sakumura et al (102)
15	k_7 , k_{-7}	0.5 μM^{-1} s^{-1} , 0.003 s^{-1}	Lammers et al (103)
16	k_8	1 μM^{-1} s^{-1}	Estimated

17	k_9 , k_{-9}	1 μM^{-1} s^{-1} , 1 s^{-1}	Estimated
18	k_{10} , k_{-10}	1 μM^{-1} s^{-1} , 1 s^{-1}	Estimated
19	$k_{cat,9}$, k_{m9}	2.4 s^{-1} , 0.1 μM	Besser et al (104)
20	$k_{cat,10}$, k_{m10}	21 s^{-1} , 10 μM	Besser et al (104)
21	$k_{cat,11}$, k_{m11}	10 s^{-1} , 20 μM	Besser et al (104)
22	k_{11} , k_{-11}	1 μM^{-1} s^{-1} , 1 s^{-1}	Estimated
23	$k_{cat,12}$, k_{m12}	1 s^{-1} , 1 μM	Estimated
24	$k_{cat,13}$, k_{m13}	1 s^{-1} , 1 μM	Estimated
25	$k_{cat,14}$, k_{m14}	1 s^{-1} , 1 μM	Estimated
26	k_{12} , k_{-12}	1 μM^{-1} s^{-1} , 1 s^{-1}	Estimated
27	$k_{cat,15}$, k_{m15}	1 s^{-1} , 1 μM	Estimated

2.3.8 Full mathematical model of proteins/lipids

The nullclines of active Rac and active WGAP were obtained by solving the steady state solutions of the reduced model. Observation of the phase plane in **Fig. 3.7** tells us clearly that the steady state solution indicated by the star is a stable one. To achieve large excursions in the value of Rac when the system is moved out of its steady state, the value of WGAP must be sufficiently low. This critical value of WGAP is indicated by the largely unchanging portion of the Rac nullcline. Rearranging the terms in the equation $\delta x/\delta t = 0$, we obtain:

$$y = \frac{v_1}{v_2}\left[1 + k_{m2}\frac{-x^2 - x + 1}{x^2(k_{m1} + 1 - x)}\right] \quad (5)$$

Given that the value of k_{m2} is small (note that k_{m2} governs the deactivation rate of Rac due to WGAP), the value of y can be approximated to be v_1/v_2. In the simulations, the ratio used was 0.5.

2.4 Conclusion

This study investigated how varying PDMS substrate stiffness affects CDR properties after PDGF stimulation of NIH 3T3 fibroblasts. To accomplish this, the cells were seeded on three PDMS substrates with differing stiffnesses as well as on glass substrates. We found that an increase in the underlying substrate stiffness of these cells increased the lifetime of CDRs but not their size. Mathematical modeling of the signaling pathways demonstrated that the increase in lifetime of CDRs with increasing substrate stiffness was an effect of the antagonism between Rac and Rho, as Rac activation coupled with increased substrate stiffness led to heightened disassembly of stress fibers as a result of Rac-induced deactivation of Rho. The rise in G-actin available for Rac-induced CDRs formation therefore led to an increase in the lifetime of the CDRs. One future area of interest is to knock down or inhibit Arp2/3, which may reduce the amount of CDRs observed as Rac can no longer effect Arp2/3 nucleation of actin. A knock-down of mDia1, however, may reduce the lifetime of CDRs observed because fewer stress fibers are formed, resulting in diminished replenishing of the G-actin pool during CDR formation. On the other hand, PDGF stimulation followed by the inhibition of mDia1 may lead to prolonged CDR formation because the inhibition of mDia1 is a downstream effect of the inactivation of Rho. It is also noteworthy to mention that the absence of forces in the model suggest that the closing and

disappearance of CDRs can be achieved independently of mechanical pulling on CDR actin, which can result from myosin localization to CDRs. Using the same model, we also show how RacGAP that binds to WAVE1 (which we term ‘‘WGAP’’) negatively regulated Rac and caused a local dip in the amount of Arp2/3-nucleated CDRs. This suggests that in the future, knocking out WGAP or mutating the binding domains between WGAP and WAVE1 may result in actin patch formation on the dorsal surface of migratory cells upon PDGF addition, which grow and disappear with similar dynamics as CDRs. Using a reduced model comprising only Rac and WGAP, we demonstrated that CDR actin growth and decay can be modeled as a pulse propagation in an excitable medium. The velocity of the moving front could be verified through live cell imaging in a future direction of this work. Through the potential effects that substrate stiffness has on CDR functionalities, such as macropinocytosis, cell motility, and RTK receptor internalization, we believe that our results have implications in fields ranging from mechanobiology to cancer research.

Chapter 3

CDRs Increase Persistency of Cell Migration by Reorganization of Actin

The findings in this work have been prepared for submission to suitable journals for peer review.

3.1 Introduction

CDRs play an important role in various cellular processes, including cell motility (58-60), macropinocytosis (63) and cell surface receptor internalization (67). These transient actin-rich structures are brought about by cell stimulation via various growth factors, such as the platelet derived growth factor (PDGF), and persist on the dorsal surface of cells for tens of minutes before disappearing (52-54). This persistence lifetime of CDRs is affected by the stiffness of the underlying substrate (106). CDRs have been linked to cell motility through large-scale actin cytoskeleton reorganization (57, 61, 62), whereby cells exhibiting CDRs show an increase in lamellipodia protrusion (57).

Migration enables cells to move into other surrounding regions of the extracellular environment. This allows them to participate in various important physiological processes such as gastrulation (106), leukocyte extravasation (107) and wound healing (108), as well as pathological processes such as metastasis of cancer cells (109, 110). The migration process in cells adherent to the substrate involves the continuous formation and dissociation of cell-substrate anchorage sites (111), where forces are being transmitted from the cell to the substrate via traction forces (112) as the cell protrudes and retracts its membrane to propel itself forward. As such, the stiffness and pliability of the substrate plays a role in cell migration speed (2).

The persistence in cell migration direction affects how quickly a moving cell reaches its target location. In wound healing assays, cells at the wound edge migrate directly into the wound (108, 113), exhibiting migrational persistence towards the direction of the wound. Cellular migrational persistence is evident in many other cellular processes such as chemotaxis (114), durotaxis (3) and haptotaxis (115), where cells migrate along chemical, stiffness and substrate-bound chemoattractant gradients respectively. One important chemoattractant in which cells respond to via chemotaxis is PDGF, which also bring about the formation of CDRs. This suggests a possible link between CDR formation and cell migrational persistence.

Both lamellipodia and CDRs are actin-rich structures which have been linked to cell migration and influenced by the properties of the underlying substrate (105, 116, 117). Different models of how actin polymerization brings about CDR formation have previously been proposed (105, 118, 119). The globular actin (G-actin) monomeric components of these structures can be recycled and rapidly transported within the cells to disassemble and assemble into other actin-rich structures such as stress fibers. This mechanism is known to be governed by the Rac-Rho protein antagonistic pathways (14, 105), which allows G-actin monomers to be cycled between

bundled actin structures such as stress fibers and cross-linked actin structures such as CDRs within the cell.

In this article, we investigate the role of CDRs in the motility of NIH 3T3 fibroblasts, specifically cell migrational persistence and speed, on 10 kPa PA substrates coated with fibronectin. It has been shown that these cells exhibit optimal migration speeds on PA substrates within this range of stiffness (78). Our results indicate that cells exhibiting CDRs show an increase in migration directional persistence, but not in migrational speed. In addition, a large scale reorganization of lamellipodia from all around the edges of the cell to the edges in close proximity to the site of CDR formation is observed. We show the occurrence of a large scale reorganization of G-actin monomers from CDRs to the lamellipodia protruding at the cell edge close to the site of CDR formation.

3.2 Materials and Methods

3.2.1 Preparation and characterization of elastic substrates

Methods for preparing polyacrylamide substrates for use in cell culture have been described by various groups (78, 120, 45). Briefly, 1 mL of 0.1 M NaOH was placed on each square cover glass (No. 1, 22 mm × 22 mm; Deckgläser) and dried at 80 ºC. 250 µL of 3-aminopropyltrimethoxysilane (Sigma) was placed evenly onto each cover glass for 5 min, before being rinsed thrice with deionized H_2O and air dried. 0.5 mL of 0.5% glutaraldehyde (Polysciences) in PBS was then pipetted evenly onto each cover glass for 30 min before being rinsed with deionized H_2O and air dried. The treated cover glasses were placed in the UV hood

for 1 hr. 0.3 µL of tetramethylethylenediamine (TEMED; Sigma) and 10% (wv) ammonium persulfate (APS; Sigma) were added to 30 µL of an acrylamide/bis-acrylamide mixture, containing 10% acrylamide and a bis concentration of 0.1 %. The mixture was pipetted onto each treated cover glass and covered with another untreated square cover glass. After polymerization, the untreated cover glasses were removed and the PA gels were rinsed with filtered 50 mM Hepes at pH 8.5 (Sigma-Aldrich). 300 µL of 50 mM sulfosuccinimidyl 6 (4'-azido-2'-nitrophenyl-amino) hexanoate (Sulfo- SANPAH; Pierce) in 50 mM Hepes at pH 8.5 was spread evenly onto each cover glass and subjected to UV light at a wavelength of 320 nm from of a UV lamp (Spectroline) at a distance of 10 cm for 10 min. The PA gels were rinsed thrice with 50 mM Hepes at pH 8.5 and covered with 300 µL of a 50 mM Hepes solution at pH 8.5 containing fibronectin (BD Biosciences) at a concentration of 10 µL/mL and stored overnight in a 37 ºC tissue culture incubator. The PA gels are then rinsed and soaked in phosphate-buffered saline (PBS; Fisher Scientific) before being sterilized under the UV hood for 1 hr.

3.2.2 Cell culture

NIH 3T3 fibroblasts (National Institutes of Health) were washed once with PBS and exposed to 0.05% trypsin-ethylenediamine-tetraacetate (Invitrogen) for 5 min to dissociate them from the tissue culture plates. The cells were then seeded onto the PA gels and cultured at 37 ºC and 5% carbon dioxide in growth media consisting of Dulbecco's modified Eagle's medium supplemented with 10% calf serum, glutamine (0.3 mg/mL), streptomycin (100 mg/mL), penicillin (100 U/mL), and 20 mM n-2-hydroxyethylpiperazine-n'-2-ethanesulfonic acid at a pH of 7.4. Cells were incubated for 24 h to allow them to attach and spread. The cell culture media was replaced with media supplemented with 0.2% calf serum to serum-starve the cells. Just

before cell imaging, the cell culture media was replaced with Leibovitz's L-15 no phenol-red media (Gibco; Life Technologies). A quantity of 30 ng/mL of recombinant PDGF-BB (Invitrogen) was added to each sample to stimulate CDR formation.

3.2.3 Visualization and FRAP

NIH 3T3 fibroblasts were imaged to obtain CDR and lamellipodia sizes and cell migration speed and directional persistence using an inverted microscope (Axiovert 200; Carl Zeiss) with a 20X (0.3 NA) objective fitted with a temperature control incubator under phase contrast. Images were captured 1 hr before and after PDGF stimulation of cells, at an interval of 30 s. To visualize actin fluorescence in lamellipodia and CDRs, cells were transfected with actin-GFP (CellLight; Molecular Probes) and incubated overnight at 37 ºC. Immunofluorescence (IF) microscopy and fluorescence recovery after photobleaching (FRAP) were carried out using a laser confocal scanning microscope (LSM 510; Zeiss).

3.2.4 Quantification of cell migration persistence (γ)

The mean squared displacement r^2, where $r^2 = \Delta x^2 + \Delta y^2$, of a tracked cell with coordinates (x, y) at any point in time is characterized as having a diffusivity D. We describe the movement of the cell as $r^2 = Dt^{\gamma}$, where t is the time elapsed since the start of cell tracking and γ is denoted as a cell migration persistence factor. When γ = 1, then $r^2 = Dt$, where the displacement is proportional to the square root of the elapsed time and the cell is said to exhibit a random migrational behaviour. When γ = 2, then $r^2 = Dt^2$, where the displacement is proportional to the elapsed time and the cell exhibits migratory persistence. The value of γ is obtained for each cell

by plotting the log-log graph of r^2 against t and obtaining a linear fit, where γ is the slope of the line. Hence, cell migration persistence can be quantified using γ.

3.2.5 Data Analysis

The cell lamellipodia and CDR areas, cell migration speed and directional persistence were measured using a program written in MATLAB (The MathWorks). Lamellipodia and CDR areas were quantified by observing the darker regions of cells which characterized these structures under phase contrast imaging. Degree of lamellipodia relocalization was quantified using a modified steepest descent method (see Supporting Material). The cell migration speed and persistence were quantified by tracking the movement of the centroid of the cell in time. The FRAP data was analyzed using Zen 2011 (Carl Zeiss) and a program written in MATLAB (The MathWorks)

3.2.6 Quantification of lamellipodia localization around cell edges using the relaxation and steepest descent method

To map and quantify the localization of lamellipodia present around the cell edges from phase contrast images such as that in **Fig. 3.2A** (left panel), the image is first converted into a normalized greyscale image, such as that in **Fig. 3.2A** (center panel). This is done by thresholding the image and setting the pixel values of all darkened regions not in contact with the cell edges to 0.5. Pixels within darkened lamellipodia regions around the cell edges are then set to a value of 1.0, while regions outside of the cell have pixel values set to 0. The resultant image

is plotted in **Fig. 3.2A** (center panel), where pixels with values of 0 and 1.0 are white and black respectively.

To obtain a gradient contour with respect to the pixel values within the cell region, the relaxation method for the solution of the Laplace equation in 2-D is employed (121). First, the centroid of the cell is determined and a circle with a radius of 4 pixels is drawn around it. The pixels within this circle have values set to 1.0. The resulting greyscale cell image is then taken to be a Laplace equation with Dirichlet boundary conditions within the 2-D cell region *S*, with a cell boundary contour of *C*. The sites which the pixels reside are denoted by the integers (*i*, *j*) and $\psi(i, j)$ is the value of the pixel occupying the site (*i*, *j*). The relaxation method is then applied to *S*, where each $\psi(i, j)$ is takes on the average value of the four neighboring sites:

$$\psi(i,j) = \frac{1}{4}[\psi(i-1,j) + \psi(i+1,j) + \psi(i,j-1) + \psi(i,j+1)] \quad (6)$$

The relaxation method is applied iteratively until convergence of $\psi(i, j)$ is achieved.

To map the gradient contour map to a circle, the steepest descent method in 2-D is used (122). The circumference of the circle surrounding the centroid of the cell is discretized into 100 points ranging from $-\pi$ to π. By marching each of these points and constructing a steepest descent gradient path line from each point via:

$$r_k = r_{k-1} - \epsilon \nabla \mathrm{f}(r_{k-1}) \quad (7)$$

Where *k* is current number of steps that the gradient path line has advanced, r_k is the coordinates of the next point that the path line takes, r_{k-1} is the coordinates of the point that the path line is currently at, $\epsilon = 0.1$ and $\nabla f\,(r_{k-1})$ is the gradient of ψ at r_{k-1}. The result is 100 lines which span from the centroid of the cell and terminate at the cell edge obtained using the steepest gradient descent method.

A representative plot of these lines in a cell is shown in **Fig. 3.2A** (right panel). Each of these lines is characterized by their radial coordinate (*RC*), which is the angle in radians that line occupies with respect to the positive x-axis in **Fig. 3.2A** (right panel), where the clockwise direction is denoted as positive. Some of the gradient lines intersect the lamellipodia regions denoted in **Fig. 3.2A** (center panel), and the intersection ratio (*IR*), which is the length of intersection between the lamellipodia regions by each line over the total length of the line, is determined. *IR* is normalized such that $\sum_{i=1}^{100} IR_i = 1$. The weighted mean of all *RC* (weighted with respect to their individual *IR* values) and the weighted variance is determined. The mean-to-variance ratio is plotted to quantify the localization of lamellipodia present around the cell edges. A large value of mean-to-variance ratio implies a specific localization of the lamellipodia at the cell edge, and a low value indicates that the lamellipodia is spread out around the cell edges.

3.3 Results and Discussion

3.3.1 CDRs contribute to cell migration persistence but not speed

When cells seeded on 10 kPa PA gels are stimulated with PDGF, we found that cells that exhibit CDRs show an increase in directional cell migration persistence (**Fig. 3.1A-C**) as compared to cells stimulated with PDGF but not exhibiting CDRs, and the control case where cells are not stimulated with PDGF. The time lapse images of a cell stimulated with PDGF 60 min into the experiment and exhibiting a CDR at 65 min is shown in **Fig. 3.1A**. The cell is monitored for a duration of 120 min. Red arrows in each panel indicate the current direction of migration of the cell and the yellow arrow points to the CDR formed at 65 min. In **Fig. 3.1A**, from 0 min to 65 min before CDR formation the cell migrates in a non-persistent manner, changing its direction of migration several times. After CDR formation from 65 min to 120 min, the cell consistently migrates in the same direction. In **Fig. 3.1B**, three representative plots of cell migration in the x and y direction with respect to time t are shown for all three cases of cells in the control case (left panel), stimulated with PDGF without exhibiting CDRs (center panel) and stimulated with PDGF and exhibiting CDRs (right panel). Three different colors (red, blue and green) in each plot are used to represent the trajectories of three different cells. PDGF stimulation is applied at 60 min into the experiment. The migrational trajectory of the cell in **Fig. 3.1A** is plotted in red in the right panel in **Fig. 3.1B**. Cells exhibiting CDRs appear to move in a more directed and persistent manner after PDGF stimulation as compared to cells which are not exhibiting CDRs.

This persistence in cell migration direction can be quantified using a defined cell migration persistence factor γ where a value of 2 denotes directed motion and a value of 1

denotes random walking (see Materials and Methods). The persistence factor γ for all three cell populations are quantified in **Fig. 3.1C**. Cells exhibiting CDRs show a significantly higher average γ of 1.96 ±0.34 than cell populations which did not exhibit CDRs where γ is 1.39 ±0.33. The cells with CDRs exhibit an increase in migrational persistency, and this suggests that CDRs might play a role in cell migration directional persistence. However, migrational speeds show no significant difference between cells with and without CDRs (**Fig. 3.1D**). How CDR formation brings about an increase in cell migration persistence is investigated by the observation of the lamellipodia protrusions of cell before and after CDR formation (**Fig. 3.2**).

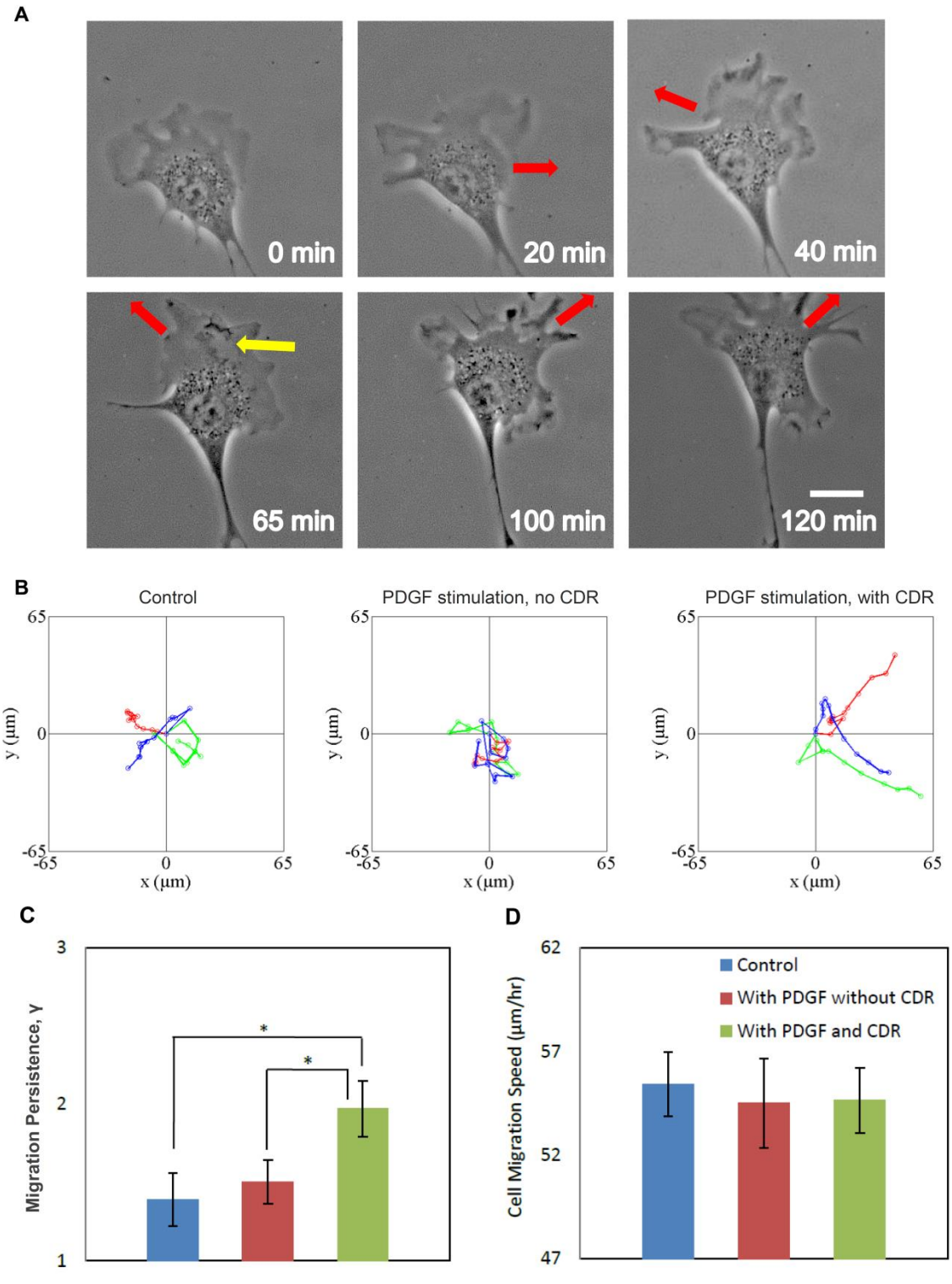

FIGURE 3.1: Cells with CDRs show an increase in the persistence of the direction of migration with no change in the migration speed. (A) Time lapse images of a migrating

cell exhibiting CDRs 65 min into the experiment. The cell exhibits directional migration persistence after CDR formation (red arrows denote current cell migrational direction, yellow arrow points to the CDR). (B) Representative plots of the centroid of cells over time for all three cell populations: control (no stimulation; left panel), the additional of PDGF for cells that do not exhibit CDRs (center panel), and with the addition of PDGF for cells with CDRs (right panel). Red, blue and green colors represent the migrational trajectories of different cells in each panel. The migrational trajectory of the cell shown in Fig. 1A is plotted in red in the right panel. Cells exhibiting CDRs show an increase in persistence in migration direction compared to cells stimulated with PDGF but not exhibiting CDRs, and cells without PDGF stimulation. Each data point represents 10 min in time. PDGF stimulation is applied at 60 min into the experiment so 6 data points are controls prior to PDGF stimulation. (C) A plot of γ, which quantifies cell migration persistency for cells with CDRs, for all three cell populations. γ for cells exhibiting CDRs is significantly higher than the other cell populations. (D) A plot of the cell migration speed of all three cell populations. Cells with CDRs did not show a difference in migration speed compared to the other cell populations. (* $p<0.005$, n=30, bars denote standard error, scale bar = 20 μm)

3.3.2 CDR formation relocalizes lamellipodia from all edges of the cell to the edge in the vicinity of the CDR

The localization of lamellipodia from phase contrast images around the cell edges is quantified using a modified steepest descent method (see Materials and Methods), which maps the cell edges to the perimeter of a circle with a coordinate system having a range of $-\pi$ to π (**Fig. 3.2A**). This enables quantification of how distributed or localized the lamellipodia protrusions are around the cell edges at any given point in time. **Fig. 3.2B** shows phase contrast images of cells at 0 min and 20 min after the start of the experiment for a cell exhibiting a CDR, a cell stimulated with PDGF but not exhibiting CDRs, and a control cell without PDGF

stimulation. PDGF is added to the cells 10 min in to the experiment, except for the control case. For the cell exhibiting a CDR, there is visible relocalization of lamellipodia from various parts of the cell before PDGF stimulation to the leading edge after stimulation (Yellow arrows denote lamellipodia in the case of a cell exhibiting a CDR). This relocalization of lamellipodia is not visible in the other cases where CDRs are not exhibited.

To quantify the relocalization of lamellipodia throughout the experiment, we plotted the mean-to-variance ratio (see Materials and methods) of the lamellipodia protrusions around the cell edges after mapping them using the steepest descent method at each point in time (**Fig. 3.2C**). A high mean-to-variance ratio indicates that lamellipodia protrusions around the cell edge are localized and concentrated in one area, while a low mean-to-variance ratio shows that lamellipodia protrusions are spread out evenly around the cell edges. For the cell population exhibiting CDRs after PDGF stimulation, there is a significant increase in the mean-to-variance ratio of lamellipodia localization after PDGF stimulation, when compared to the other cases with no CDR formation. This indicates that lamellipodia protrusion goes from non-localized before CDR formation to localized after PDGF stimulation, and that CDR formation could play a role in this larger scale relocalization of lamellipodia from all edges of the cell to the leading edge. Since lamellipodia protrusions contribute to cell migration directional persistence as the cell tends to move in the direction of lamellipodia protrusion (74), this localization of lamellipodia to the leading edge after CDR formation could provide an explanation as to how CDR formation brings about an increase in cell migration directional persistence.

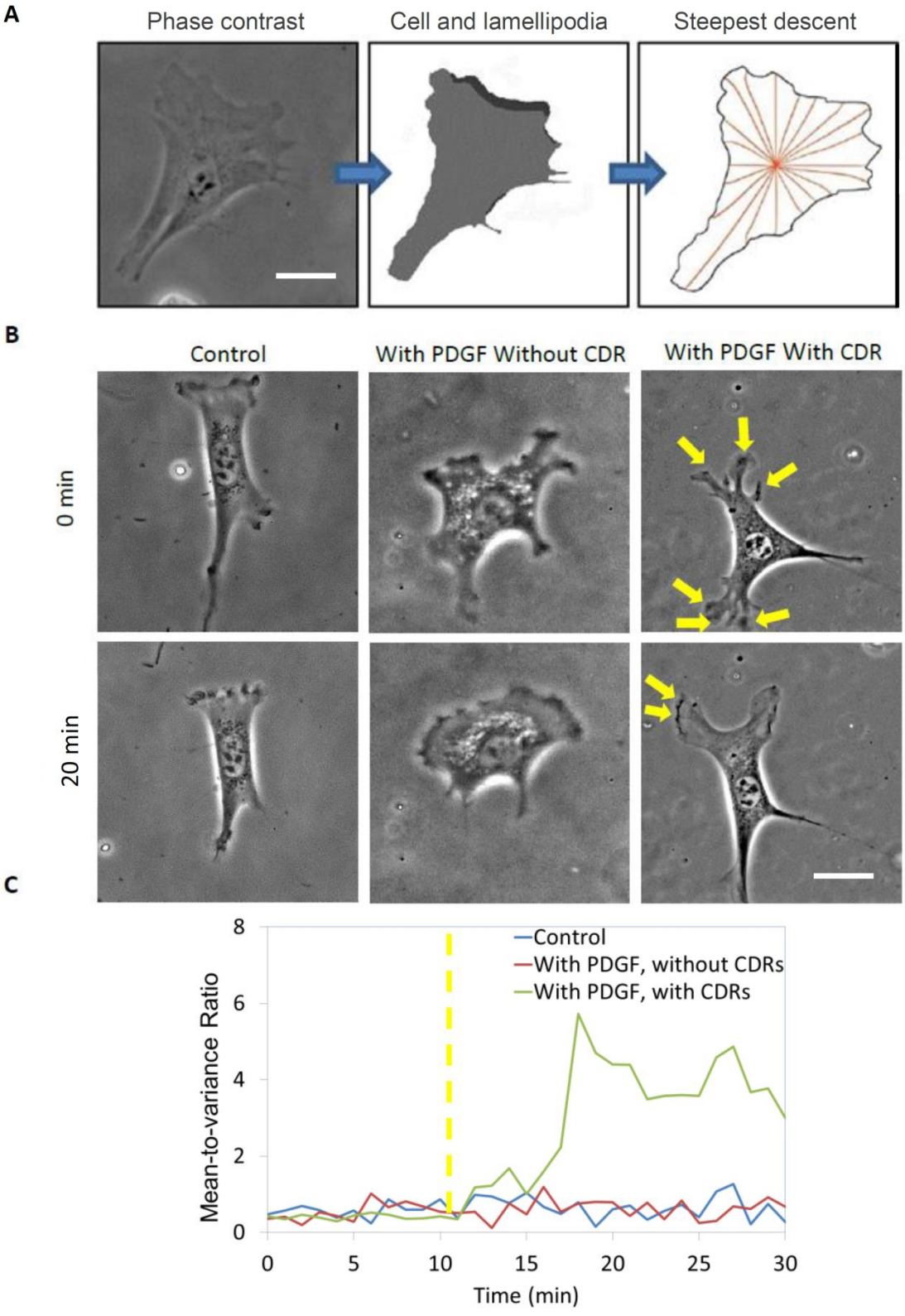
A
Phase contrast
Cell and lamellipodia
Steepest descent
B
Control
With PDGF Without CDR
With PDGF With CDR
0 min
20 min
C
Control
With PDGF, without CDRs
With PDGF, with CDRs
Mean-to-variance Ratio
Time (min)
0
2
4
6
8
0
5
10
15
20
25
30

FIGURE 3.2**:** CDR formation results in the relocalization of lamellipodia from all edges of the cell to the edge in the vicinity of the CDR. (A) Mapping of cell edges from phase contrast images to a the perimeter of a circle using the deepest descent method allows quantification of the localization of lamellipodia area around cell edges with a coordinate system ranging from $-\pi$ to π. (B) Phase contrast images taken at 20X of cells at 0 min and 20 min during the experiment showing lamellipodia (dark edges) formed at the cell edges for a control cell (no PGDF stimulation), a cell stimulated with PDGF but did not exhibit CDRs, and a cell which exhibited CDRs. Yellow arrows indicate lamellipodia forming in the case where a cell exhibited CDRs, showing a relocalization of lamellipodia after CDR formation. (C) Quantification of the extent of lamellipodia localization around the cell edge (mean-to-variance ratio) plotted against time. Vertical yellow line denotes time of PDGF addition. (Scale bar = 20 μm)

3.3.3 Time lag between peak CDR formation size and the spike in lamellipodia protrusion corresponds to known diffusive time scale of G-actin monomers

To further investigate how CDR formation can lead to increased lamellipodia protrusion, we focused on the spatiotemporal relationship between CDR formation and the subsequent spike in lamellipodia protrusion by examining CDR ring size and lamellipodia protrusion size with respect to time *t* (**Fig. 3.3**). A schematic representation of the cell with localized lamellipodia area after CDR formation (highlighted in blue) and CDR area (highlighted in red) is shown in **Fig. 3.3A**. The distance *d* is the length between the center of the CDR ring during peak CDR formation at time t_1 and the centroid of the localized lamellipodia protrusion area during peak protrusion at time t_2. Peak CDR and lamellipodia protrusions do not occur at the same time, with peak lamellipodia protrusion following temporally after peak CDR formation. This time lag is denoted by $t_2 - t_1$ represented in **Fig. 3.3**. In **Fig. 3.3B**, the phase contrast images of three

representative cells during t_1 and t_2 are shown, with red arrows denoting the location of the CDRs and blue arrows denoting the location of the localized lamellipodia protrusion. From these images, the distance *d* can be obtained for every cell. In the same three representative cells, the temporal changes in normalized CDR and lamellipodia area with respect to their respective peak value throughout the experiment are plotted against time in **Fig. 3.3C**. Here, the CDR and lamellipodia area in each of the three cells are normalized with respect to the largest CDR and lamellipodia area observed in each cell respectively. The resulting values range from 0 to 1 and are color coded with the highest, 1, being red and the lowest, 0, being blue. The time of peak CDR formation t_1 always precedes the time of peak lamellipodia protrusion t_2.

The time lag between peak formations $t_2 - t_1$ can be determined for each cell. The relationship between *d* and $t_2 - t_1$ is graphed on a *log (d)* versus *log* $(t_2 - t_1)$ plot for 26 cells in **Fig. 3.3D**. A linear regression on the data yields an estimated diffusion coefficient of 42.3 $\mu m^2/s$ between sites of CDR and localized lamellipodia protrusion. This value is of the same order of magnitude as the diffusion coefficient of cytosolic G-actin monomers of 30 $\mu m^2/s$ (64). These results suggests a possible relationship by which CDR formation contributes to localized lamellipodia protrusion is by the diffusion and directed movement of G-actin monomers from the transient CDR structures to the nearby site of lamellipodia formation. This movement of G-actin from CDR to lamellipodia is likely carried out through either directed transport where the G-actin is carried directly from the CDR to the lamellipodia, or through pure diffusion, where movement of G-actin from the CDR is undirected, moving outwards in all directions and not only towards the site of lamellipodia formation.

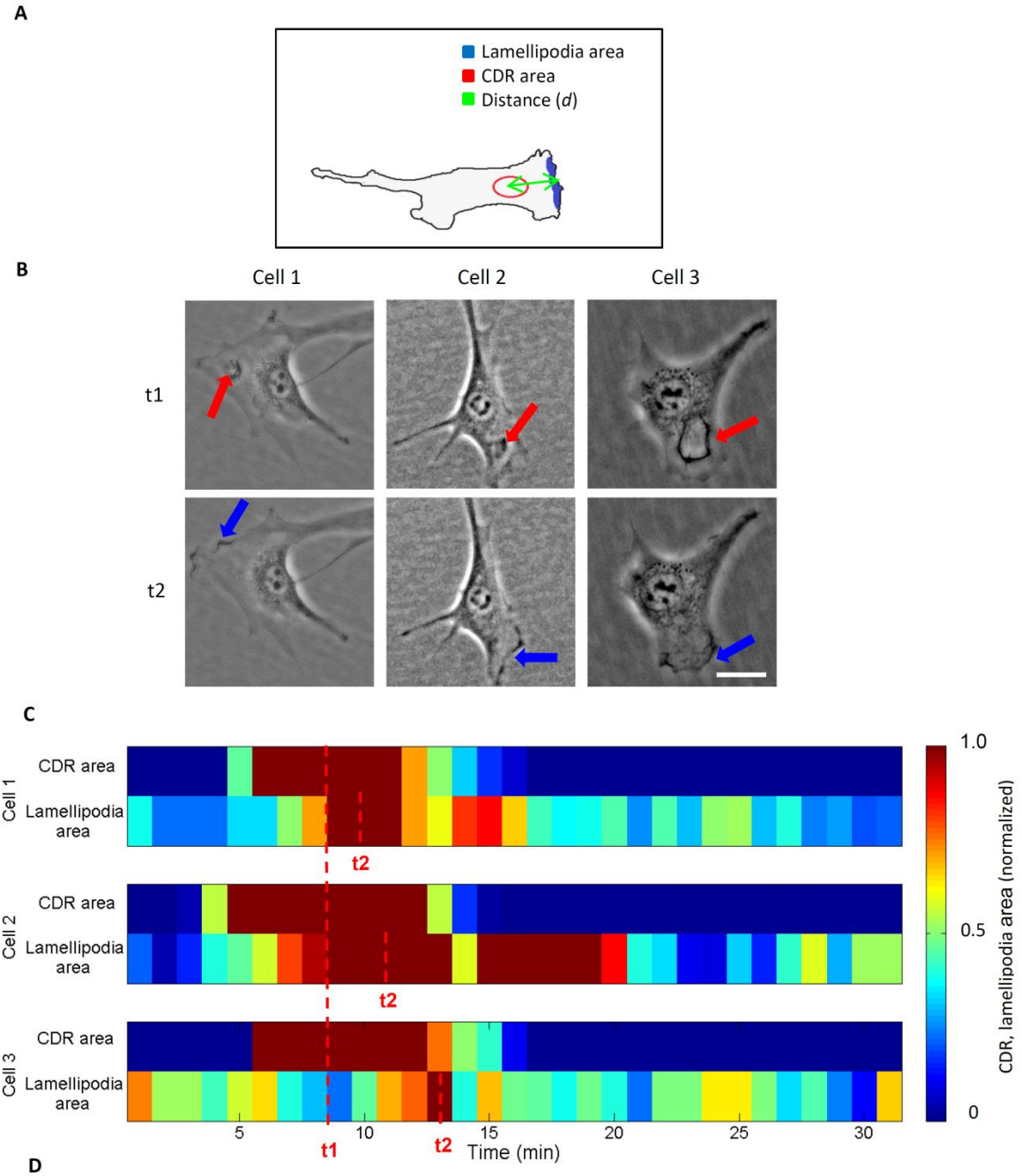
A
Lamellipodia area
CDR area
Distance (d)
B
Cell 1
Cell 2
Cell 3
t1
t2
C
CDR area
Lamellipodia area
Cell 1
Cell 2
Cell 3
t2
t1
5
10
15
20
25
30
Time (min)
1.0
0.5
0
CDR, lamellipodia area (normalized)
D
log(d)
log(t2-t1)
Cell 1
Cell 2
Cell 3
3.6
3.4
3.2
3
2.8
2.6
0
0.5
1
1.5
2

FIGURE 3.3: Time between CDR peak formation (t1) and the spike in lamellipodia protrusion (t2) corresponds to the known diffusive time scale of G-actin monomers. (A) A schematic of the outline of a cell with the lamellipodia and CDR area highlighted in blue and red respectively. The distance between the centroid of the maximum CDR size and lamellipodia protrusion area is denoted as d. (B) Phase contrast images of three cells (red arrows point to CDRs, blue arrows point to area of lamellipodia protrusion after CDR formation) and their (C) corresponding normalized CDR area and lamellipodia area plotted against time after PDGF stimulation for three representative cells. The CDR and lamellipodia area in each cell are normalized using the maximum CDR area (upper color coded bar) and lamellipodia area (lower color coded bar) observed during the experiment respectively. The time of CDR peak formation (t1) and the spike in lamellipodia protrusion (t2) are labeled for each cell. A color coded bar indicates the range of CDR and lamellipodia area from 0 to 1. (D) A linear regression on the data plotted on the log-log graph for the distance between centroid of CDR during peak formation, d, versus t2-t1 shows a diffusion coefficient of 42.3 $\mu m^2/s$, compared to the diffusion coefficient of G-actin (30 $\mu m^2/s$). (n=26, scale bar = 20 μm).

3.3.4 G-actin localizes from CDRs to lamellipodia protruded at cell edge close to CDRs

To determine if G-actin diffuses from the CDRs to the localized lamellipodia which form later, immunofluorescence images of cells transfected with actin-GFP are captured. The actin-rich CDR and lamellipodia structures are clearly visible under the fluorescence microscope with the GFP. FRAP is used to examine the location and timing of the GFP actin for examining CDR and lamellipodia dynamics. For example, if G-actin moves from the CDR to the location of the nearest lamellipodia, the photobleaching of CDRs using FRAP would cause a decrease in the fluorescence intensity of the resulting lamellipodia protrusion, since the photobleached G-actin moves from the CDR to the nearby lamellipodia. By utilizing FRAP, cells expressing actin-GFP

are photobleached at the region where CDRs occur, and the normalized fluorescence intensity of the resulting lamellipodia which protrude after CDR formation is observed (**Fig 3.4**). To obtain the normalized fluorescence intensity of the resulting lamellipodia protrusions, the differential image contrast (DIC) images are compared to the fluorescence images with respect to the lamellipodia area (**Fig. 3.4A** and **3.4B**). The lamellipodia region at each time point is obtained through the DIC images. The total fluorescence intensity for every pixel in the lamellipodia region is obtained and divided by the total number of pixels in the lamellipodia region. In **Fig. 3.4A** and **3.4B**, the DIC and fluorescence images of cells exhibiting CDRs are shown at 0, 2 and 4 min into the experiment. Red arrows denote the location of CDRs and yellow arrows denote the localized lamellipodia in the cells. The cell in **Fig. 3.4A** is not photobleached while the cell in **Fig. 3.4B** has the region containing the CDR photobleached (region denoted by blue dotted box). Photobleaching is carried out 10 s into the experiment. A plot of normalized fluorescence intensity against time in **Fig. 3.4C** shows that after photobleaching the CDR, the resulting lamellipodia protrusion exhibits a significant decrease in actin-GFP fluorescence intensity about 60 s after photobleaching has occurred (FRAP applied). Recovery of this fluorescence intensity takes place about 120 s after photobleaching. This decrease and recovery of actin-GFP fluorescence is in contrast to the cases where no photobleaching of the CDR occurs (no FRAP applied), and when the photobleached region is located away from the site of CDR formation in the cell (control case). In both these cases, no sharp decrease or subsequent recovery of fluorescence intensity is observed. The G-actin from the CDRs appears to relocalize to the lamellipodia protruded at the cell edge closest to the site of CDR formation.

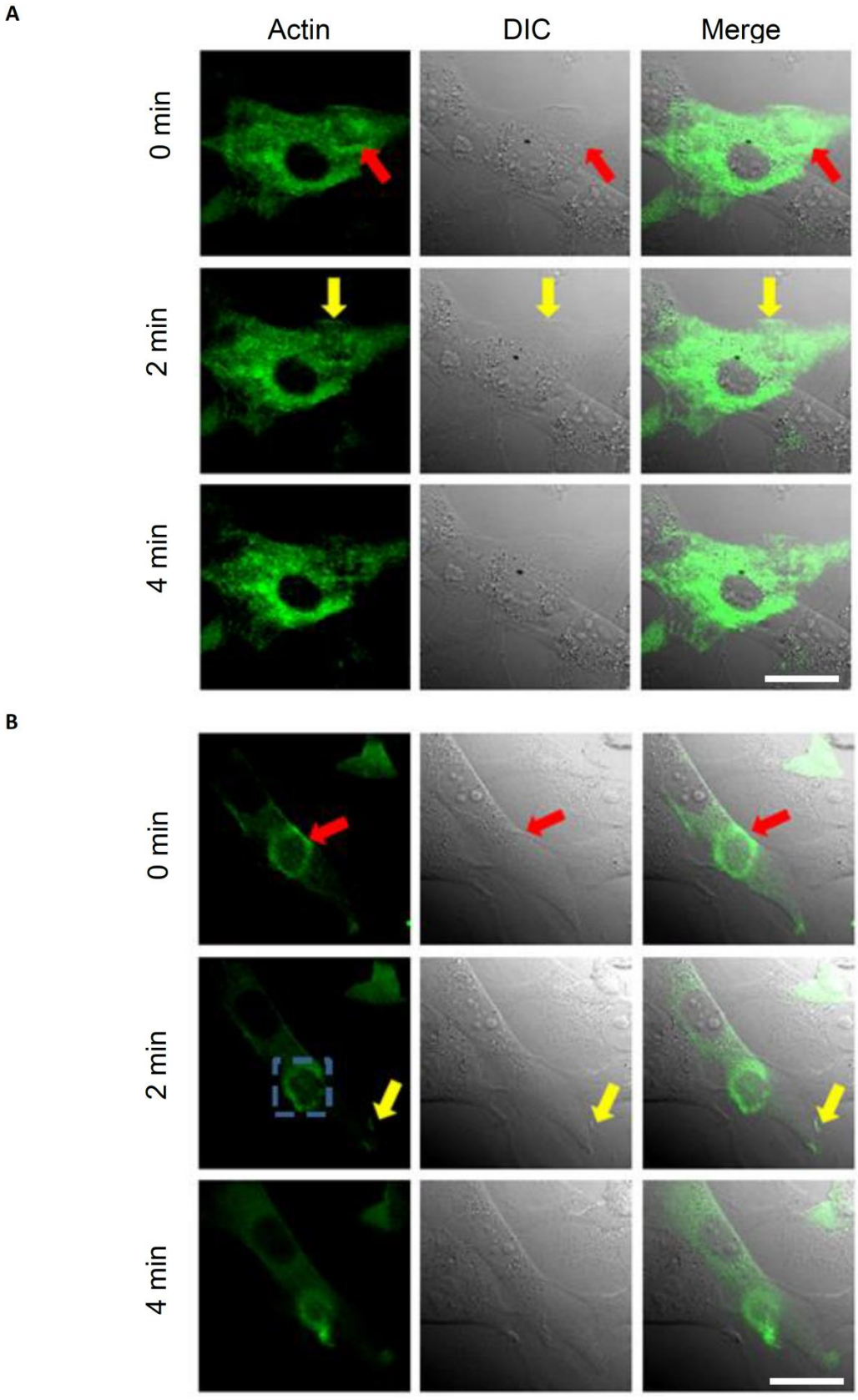
A
Actin
DIC
Merge
0 min
2 min
4 min
B
0 min
2 min
4 min

C

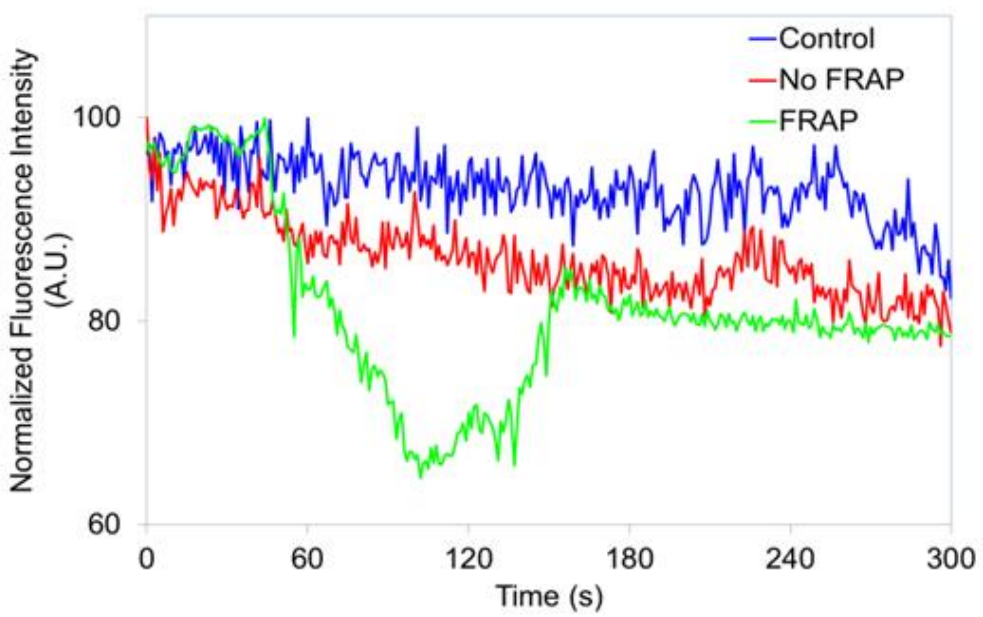

FIGURE 3.4: G-actin localizes from the CDRs to the lamellipodia protruded at the cell edge close to the CDRs based on FRAP analysis. 63X fluorescence images of actin-GFP, DIC images and the resulting merged images of representative cells 0, 2 and 4 min after CDR formation with (A) CDRs which have not been photobleached and (B) CDRs which have been photobleached. Photobleaching of the CDRs is carried out 10 s into the experiment (Red arrows point to CDRs, yellow arrows point to area of lamellipodia localization after CDR formation and the blue box denotes FRAP area). (C) Representative experiments of normalized fluorescence intensity (A.U) of the protruding lamellipodia in cells where CDRs have formed for the control case, where an area of the cell other than the CDR was photobleached, the case where no photobleaching of the CDR occurs, and the case where the CDR is photobleached. When the CDRs are photobleached, there is a decrease in normalized fluorescence intensity of the resulting lamellipodia protrusion followed by recovery. (Scale bar = 20 μm).

These findings provide insight into how the formation of CDRs in cells would result in the increase in directional persistence during cell migration. The CDRs appear to act as a G-actin pool source for the localized lamellipodia protrusions forming at the cell edges near the CDR. Our hypothesis is supported by previous studies which have shown that CDRs almost always form near the leading edge of cells after PDGF stimulation (57). This allows cells to protrude lamellipodia in a localized manner near the leading edge as opposed to equally at all edges of the cell, which would contribute towards directed motility and migrational persistence in the direction of the leading edge.

Although cell migration persistence increases with CDR formation, cell migrational speeds show no significant difference between cells with and without CDRs (**Fig. 3.1D**). A possible explanation for these phenomena is that although cells have been shown to protrude more lamellipodia after CDR formation (57), as verified in **Fig. 3.3B** and **C**, this does not necessarily translate to higher migration speeds. This is because the process of cell migration is not governed by lamellipodia protrusion alone; other factors such as cell trailing edge retraction and cell-substrate traction forces play important roles in the migration process (74).

Although our data suggest that actin from the CDRs moves to the protruding lamellipodia at the cell edge nearest to the site of CDR formation, how actin is transported between these two structures is not clear. Diffusion of actin from CDR to the lamellipodia could be one possibility (123). As the CDR breaks down, the actin components diffuse in the cytosol, in all directions away from the CDR ring, and actin that diffuses towards the site of lamellipodia protrusion eventually becomes part of the lamellipodia. Another possible mechanism that could explain the transport of actin from the CDRs to the lamellipodia is via actin-binding proteins like Myo1c

(124), which have been implicated in transporting G-actin components to the lamellipodia at the leading edge of endothelial cells.

The implication of CDRs in directed cell motility here suggests how a structure formed by the cell which requires the expenditure of energy is involved in carrying out a specific cell function. In this case, the formation of the CDR structure by the cell requires energy for membrane bending and actin polymerization (113), and fulfills a specific function of causing the cell to persist in a migrational direction, as well as other specific cell functions such as macropinocytosis (58). Since CDR formation is triggered by the stimulation of cells with PDGF, the persistence in the direction of migration for cells exhibiting CDRs could be in response to available growth factors in the extracellular environment. This is supported by experiments done by Orth et al. (67), whereby CDRs are found to form near the location of localized extracellular growth factor stimulation administered via a microneedle.

3.4 Conclusion

In this study, the role of CDR formation in the regulation of cell motility of NIH 3T3 fibroblasts was investigated with regards to cell migrational persistence and speed on fibronectin-coated 10 kPa PA substrates. We found that cells exhibiting CDRs show an increase in directional persistence during cell migration but not in migration speed when compared to cells which did not exhibit CDRs. This increase in persistence could be attributed to large scale reorganization of lamellipodia from all around the edges of the cell to the edge closest to where CDR formation takes place, allowing the cell to protrude lamellipodia locally at the leading edge and propel itself forward in that direction. The current study provides the first experimental

evidence of a source of actin for lamellipodia formation. We show that actin from CDRs are being localized to lamellipodia protrusions, suggesting a role for CDR in preparing cells for directional migration. We believe that this highlights a new function of CDRs in the area of cell motility and has implications in the fields of cell mechanics, cell migration and cancer research with respect to how cells explore their surrounding environment.

Chapter 4

Modulating Substrate Stiffness Dynamically through Thin Silicone Membranes

This chapter contains currently unpublished work that is on-going.

4.1 Introduction

The fabrication of cell culture substrates in 2-D with tunable stiffnesses has been an intensively studied field in mechanobiology. Previous studies have revealed that cell motility (127), the reorganization of cellular cytoskeleton (128) and stem cell differentiation (5, 74) are influenced by substrate stiffness and compliance (78, 129). For example, fibroblasts can differentiate into myofibroblasts at the site of a wound where injury has occurred. These myofibroblasts are capable of repairing as well as replacing damaged ECM in damaged organs as well as tissues (130). The stiffness of the extracellular environment increases as ECM is secreted by the myofibroblasts. After some time, the myofibroblasts stop secreting ECM and go through senescence and apoptosis (46, 130). Pathological instances occur, whereby the myofibroblasts do

not get inactivated and continue secreting ECM, increasing the stiffness of the extracellular environment, thus causing fibrosis (131). Elucidating the influence of substrate stiffness in dynamic cellular signaling processes such as those undergone by the myofibroblasts in this instance is crucial for the treatment of fibrotic related diseases (74).

Polymeric substrates which have been used in extracellular substrate stiffness studies include poly(ethylene glycol) (PEG) gels, PDMS, PA and hyaluronic acid-based polymer systems (32, 74, 78, 105, 120, 132). These polymers require the establishment of unique formulations for each gel system, such as tuning the different crosslinker concentrations, to vary the stiffness of the gel system. A major disadvantage and limitation of these systems are that the material properties are fixed and not dynamic. As such, spatially dynamic stiffness gradients within hydrogels have been formulated to overcome these limitations (133, 134). For example, hydrogels with differing stiffnesses on the same substrate have been fabricated by mixing different formulations of PA gels (2). More advanced fabrication techniques have made use of microfluidics to fabricate PA gel gradients (135). PDMS substrates with stiffness gradients have also been fabricated from patterning (136). Although substrate stiffness properties can be dynamically controlled spatially in these cases, the limitation of static temporal stiffness in these systems still exists.

To overcome the limitation in temporal stiffness experienced by existing polymeric systems, Frey and Wang developed a PA photodegradable hydrogel, where the polymer stiffness can be decreased by irradiation with UV light (47). The dynamic modulation of substrate stiffness was used to study the influence of real-time softening environments on 3T3 cell migration and morphology. Kloxin et al. have also developed a photodegradable monomer for the synthesis PEG hydrogels that degrade when irradiated. This polymer system is biocompatible

and can be used to encapsulate cells and study them in 3-D cell cultures (137, 138). However, these systems still face a limitation as the change in stiffness is not reversible spatially or temporally. The stiffness of the substrates can only soften with time. In this work, our motivation is to overcome this limitation and create a polymer system in 2-D which can mimic a dynamically changing, reversible and localized substrate stiffness environment.

The evidence from cells being able to sense the thickness of substrates that they are being seeded on comes from a study quantifying traction forces (125) in 3-D. In the paper, displacement of fluorescent beads embedded in gels exhibit substantial displacements even up to 30 μm below the gel surface. To further probe the influence of cell-substrate interactions on cell behavior and actin dynamics, a 2-D system which introduces a dynamically changing, reversible and localized substrate stiffness environment is constructed here. Cells that are seeded on top of thin PDMS membranes are capable of feeling through the thin layer, experiencing the stiffness of the separate PDMS substrates below the thin membrane. The membranes are carefully re-transplanted on top of other PDMS substrates with differing stiffnesses. This reversible dynamic stiffness system can then be used in the investigation of the influence of reversible dynamic stiffness environments on cell morphology, motility, proliferation and differentiation in various cells types.

In this chapter, the fabrication and characterization of the thin PDMS-underlying substrate systems are carried out. The system with the thin PDMS membrane lying on top of a separate PDMS substrate below will hereon be referred to as the bilayer system. We then focus on measuring the mechanical stiffness of the bilayer system using finite element analysis (FEA) carried out in Autodesk (Autodesk, Inc.). In addition, the possible delamination of the PDMS bilayer system is investigated. Using analytical equations, we determine an optimal set of

physical parameters for the bilayer, such that delamination of the thin membrane away from the underlying PDMS substrate does not occur during cell culture in 2-D. We next use this bilayer system to investigate the effect of dynamically changing substrate stiffness on the morphology of 3T3 cells.

4.2 Materials and Methods

4.2.1 Preparation and characterization of thin PDMS membranes

Previous methods for fabrication of thin PDMS membranes have been described (126). By modifying the fabrication process, square thin PDMS membranes of up to 100 nm in thickness can be fabricated with widths of up to 5 mm (**Fig. 4.1**). Briefly, SU-8 5 (Micro Chem) was spin-coated onto a silicon wafer at 2000 RPM for 30 s. By varying the base/curing agent ratio in the PDMS membranes (Sylgard 184; Dow Corning), the resulting elastic modulus can be modified. Young's modulus values of 500, 750, 1000, and 1600 kPa were obtained using ratios of 25, 20:1, 15:1, and 10:1 silicone elastomer base/curing agent, respectively. In order to obtain PDMS membranes with thicknesses in the order of hundreds of nanometers, the PDMS solution is diluted with hexane (Fisher Scientific) at PDMS:Hexane ratios of 1:5, 1:10, 1:20, 1:30, 1:60 and 1:90 before being spincoated on top of the SU-8 5 layer at 6000 RPM for 150 s to produce PDMS membranes with 1540, 740, 410, 315, 195 and 96 nm thicknesses respectively. The silicon wafer construct is baked at 110 ºC for 15 min. A thick PDMS square window supporting frame with a height of 3 mm, an outer width of 10 mm and an inner window width of 5 mm is placed onto the PDMS membrane and left to bond at room temperature. To detach the PDMS block with the PDMS membrane bonded to it from the silicon wafer, the silicon wafer construct

is placed in SU-8 developer (Micro Chem) for 1-2 min, and the PDMS block with the PDMS membrane bonded to it is carefully removed and rinsed with ethyl alcohol (95%; PHARMCO-AAPER) and deionized H_2O before being sterilized under the UV hood for 1 hr.

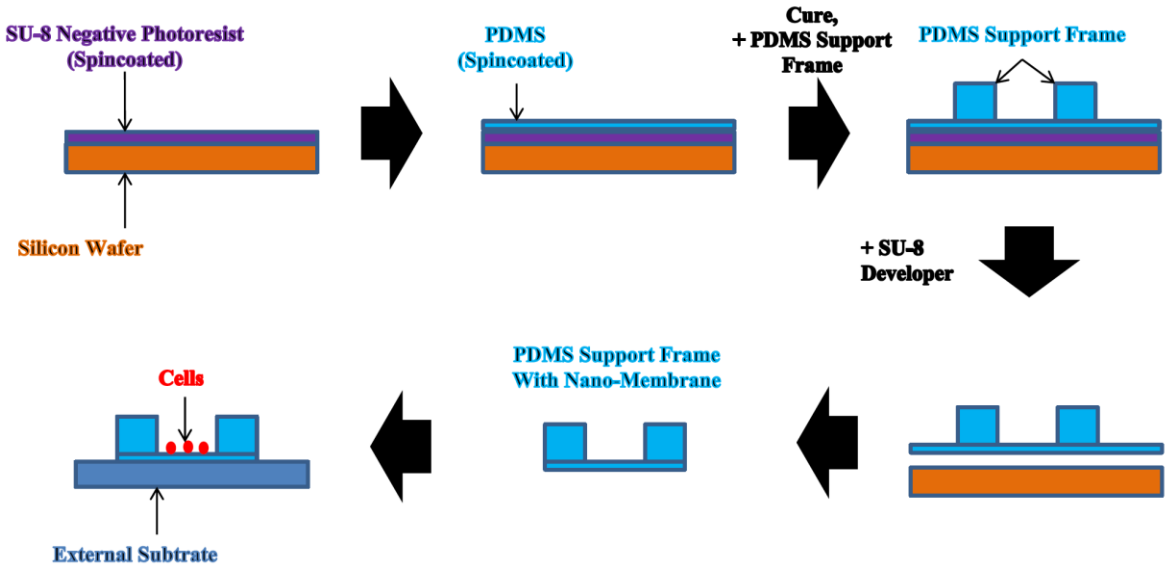

FIGURE 4.1: Steps in the fabrication of thin PDMS membranes attached to PDMS support frames using soft lithography techniques.

4.2.2 Preparation of Underlying PDMS gel substrates

Methods for preparing PDMS substrates with attainable stiffnesses as soft as 5 kPa for use in cell culture have been described (139). Briefly, commercially available PDMS, Sylgard 527 gel and Sylgard 184 elastomer (Dow Corning), were mixed to create PDMS substrates with different mechanical properties. Sylgard 527 was prepared by mixing equal weights of part A and B while Sylgard 184 was prepared by mixing a 10:1 ratio of silicone elastomer base/curing

agent. Three different ratios of the Sylgard 184:527 were evaluated; 1:0, 1:20 and 1:10. Pure Sylgard 527 and 184 polymer mixtures were first created separately as described above before being mixed at the three different ratios and degassed under vacuum to remove any bubbles before curing overnight at 60 ºC. The stiffnesses of the three polymers as measured by Palchesko et al. (139) are 5, 20 and 50 kPa for Sylgard 527:184 ratios of 1:0, 1:20 and 1:10 respectively.

4.2.3 Cell Culture

To prepare PDMS membranes for cell culture, the surfaces were first sterilized using ethyl alcohol (PHARMCO-AAPER). Phosphate-buffered saline (PBS; Fisher Scientific) at a 10× solution was diluted to 1× with deionized H_2O, filtered, and used as a buffer solution. The PDMS substrates were coated with fibronectin (10 mg/mL, PBS; BD Biosciences) for 60 min. NIH 3T3 fibroblasts (National Institutes of Health) were washed once with PBS and then exposed to trypsin-ethylenediamine-tetraacetate (0.05%; Invitrogen) for 5 min to dissociate them from the tissue culture plates. The cells were then seeded onto the PDMS membranes and cultured at 37 ºC and 5% carbon dioxide in growth media consisting of Dulbecco's modified Eagle's medium supplemented with 10% calf serum, glutamine (0.3 mg/mL), streptomycin (100 mg/mL), penicillin (100 U/mL), and 20 mM n-2-hydroxyethylpiperazine-n'-2-ethanesulfonic acid at a pH of 7.4. Cells were incubated for 24 h to allow them to attach and spread.

4.2.4 Modulating Reversible Dynamic Substrate Stiffness Spatially and Temporally

The PDMS membranes with cells seeded on them are transplanted between PA gels with differing stiffnesses to simulate a dynamic substrate stiffness environment (**Fig 4.2**). The temporal stiffening of the cell environment is simulated by transplanting the PDMS membranes from a softer to a stiffer underlying PA substrate and vice versa. The spatial modulation of the substrate stiffness environment is obtained by shifting an underlying hard/soft PA gel substrate interface underneath the PDMS membrane to simulate a spatially changing stiffness environment for the cells on the PDMS membrane.

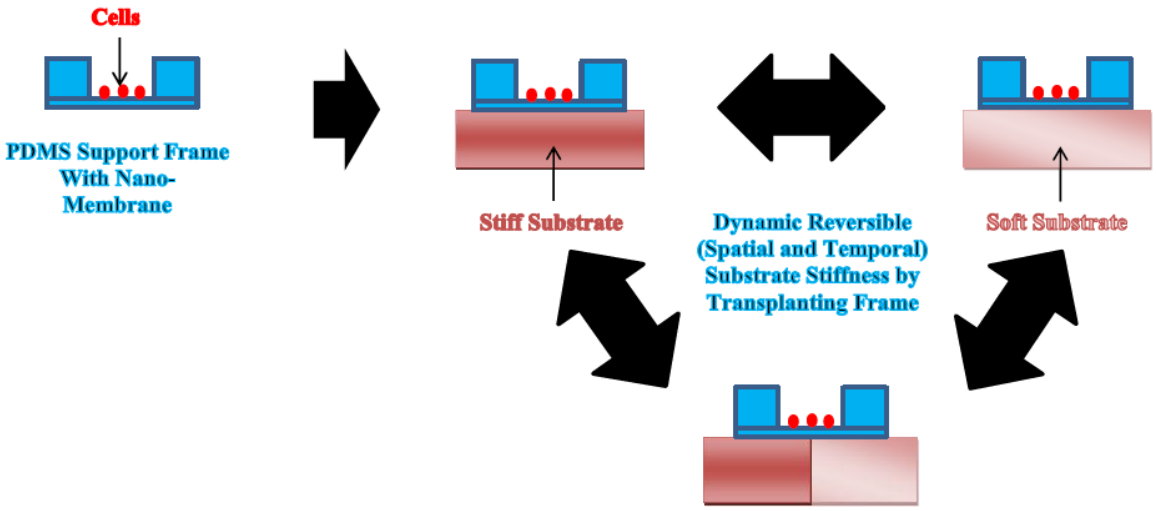

FIGURE 4.2: Steps in the modulation of spatially and temporally dynamic and reversible substrate stiffness based on transplanting the PDMS membrane with cells seeded on top.

4.2.5 Fluorescent Staining and Microscope Visualization

To visualize the cytoskeletal structure of the cells using fluorescent immunostaining, the cells were fixed with 4% paraformaldehyde and treated with 0.1% Triton-X, followed by staining with 6 mM phalloidin-tetramethylrhodamine- mine B isothiocyanate (Sigma-Aldrich) and DAPI (40,6-diamidino-2-phenylindole, dihydrochloride; 2 mg in 1 mL PBS; Invitrogen), which labeled the actin filaments and the nucleus, respectively. After incubating the cells with phalloidin and DAPI, they were mounted on glass coverslips with Fluoromount-G (Southern Biotech). By using an inverted fluorescent microscope (Axiovert 200; Carl Zeiss) with a 63× (1.4 NA) objective, the actin filaments and nucleus of the NIH 3T3 fibroblasts were imaged. Cell sizes and migration speeds were obtained using a 20× (0.3 NA) objective fitted with a temperature control incubator under phase contrast.

4.2.6 Physical Characterization of Stiffness and Thickness

The stiffness of the PA gels and the PDMS membrane-PA gel bilayer constructs were determined using a Hertz indentation method (2) and through FEA simulations carried out using Autodesk (Autodesk, Inc.). The thicknesses of the PDMS membranes were determined using Atomic Force Microscopy (AFM, Dimension 3000 SPM; Digital Instruments) through surface scanning microscopy.

4.2.7 Experimental Setup for Measurement of Work of Adhesion between two PDMS Surfaces

The pull-off force needed to separate a 10mm by 10mm square block of Sylgard 184 PDMS piece, with a thickness of 4mm and a stiffness of 1800 kPa, and PDMS surfaces of 5, 20 and 50 kPa stiffnesses respectively, with a thickness of 5 mm, was measured by suspending the two PDMS surfaces by attachment of the Sylgard 184 block to a piece of thread, and adding water to the petri dish containing the 5, 20 or 50 kPa PDMS substrates until the two surfaces are separated. The pull-off force is calculated as the weight of the water required to separate the two surfaces.

4.2.8 Data Analysis

Cell areas were measured using a program written in MATLAB (The MathWorks). Lamellipodia areas were quantified by observing the darker regions of cells which characterized these structures under phase contrast imaging. FEA simulations were carried out using Autodesk (Autodesk, Inc.) and the results were analysed in MATLAB.

4.3 Results and Discussion

4.3.1 Optimization of PDMS membrane thickness based on PDMS:Hexane formulation

By varying the PDMS: Hexane ratio, we were able to vary the thickness of the PDMS membranes from 500 nm all the way down to 100 nm (**Fig. 4.3**). The thickness of the PDMS membranes were measured using an AFM tapping mode by placing the membrane on a glass

cover slip and scratching the membrane to expose the underlying glass. The difference in topographical height between the membrane surface and the glass coverslip surface is the thickness of the membrane.

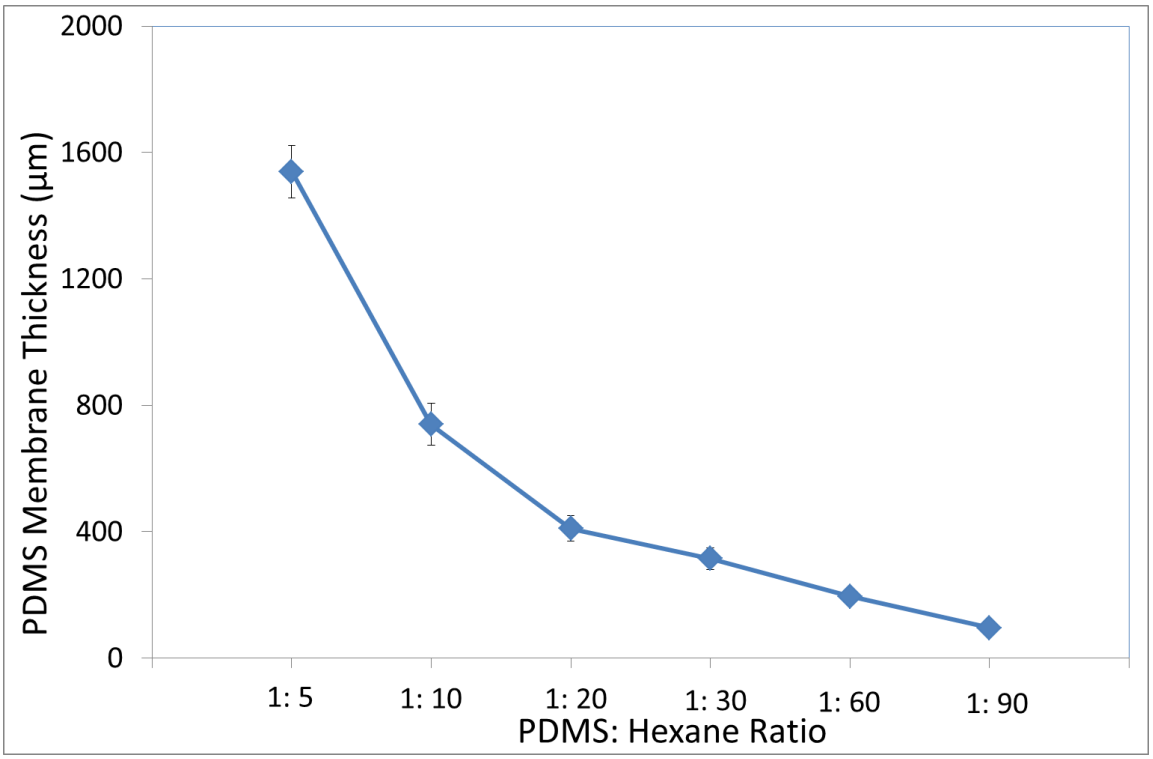

FIGURE 4.3: Optimization of thickness for PDMS thin membrane in experiments based on PDMS:Hexane formulation. (Bars denote standard error. n = 10)

4.3.2 Delamination of the thin PDMS membrane from the underlying PDMS substrate will not occur during cell culture

For an elastic thin film on a compliant substrate, two types of buckling modes can occur due to compressive stress in the film, σ (**Fig. 4.4A**). The first is a buckling of the film without delamination (wrinkling) as shown in **Fig. 4.4A**. The critical stress for wrinkling is (140):

$$\sigma_w = \frac{\bar{E}_f}{4}\left(\frac{3\bar{E}_s}{\bar{E}_f}\right)^{2/3} \quad (8)$$

The plane-strain moduli of the film and substrate are $\bar{E}_f$ and $\bar{E}_s$ respectively. When $\sigma > \sigma_w$, the buckling of the film causes wrinkles to form throughout the surface of the film.

The second mode of buckling for elastic thin films on compliant substrates is the buckling of the film with delamination (buckling-delamination) as shown in **Fig. 4.4A**. The critical stress for the buckling of a independent thin film is (141):

$$\sigma_{B0} = \frac{\pi^2}{12}\left(\frac{h}{b}\right)^2 \bar{E}_f \quad (9)$$

The half width of the delamination and thickness of the film are *b* and *h* respectively. On compliant substrates, the critical stress for buckling-delamination of a film on a compliant substrate, σ_B, can be lower than that of the buckling of a free film σ_{B0}, depending on how compliant the substrate is. An implicit expression of σ_B is (142):

$$\sqrt{\frac{\sigma_{B0}}{\sigma_B}}\tan\left(\pi\sqrt{\frac{\sigma_B}{\sigma_{B0}}}\right) = \frac{\pi h}{12b}\left(\frac{a_{12}^2}{\frac{b}{h}+a_{11}} - a_{22}\right) \quad (10)$$

Where a_{11}, a_{12} and a_{22} are the compliance coefficients of the film-substrate system which are determined numerically through FEA. Equation (10) is then solved semi-analytically using the Newton-Raphson method for σ_B, using σ_{B0} as a first approximation.

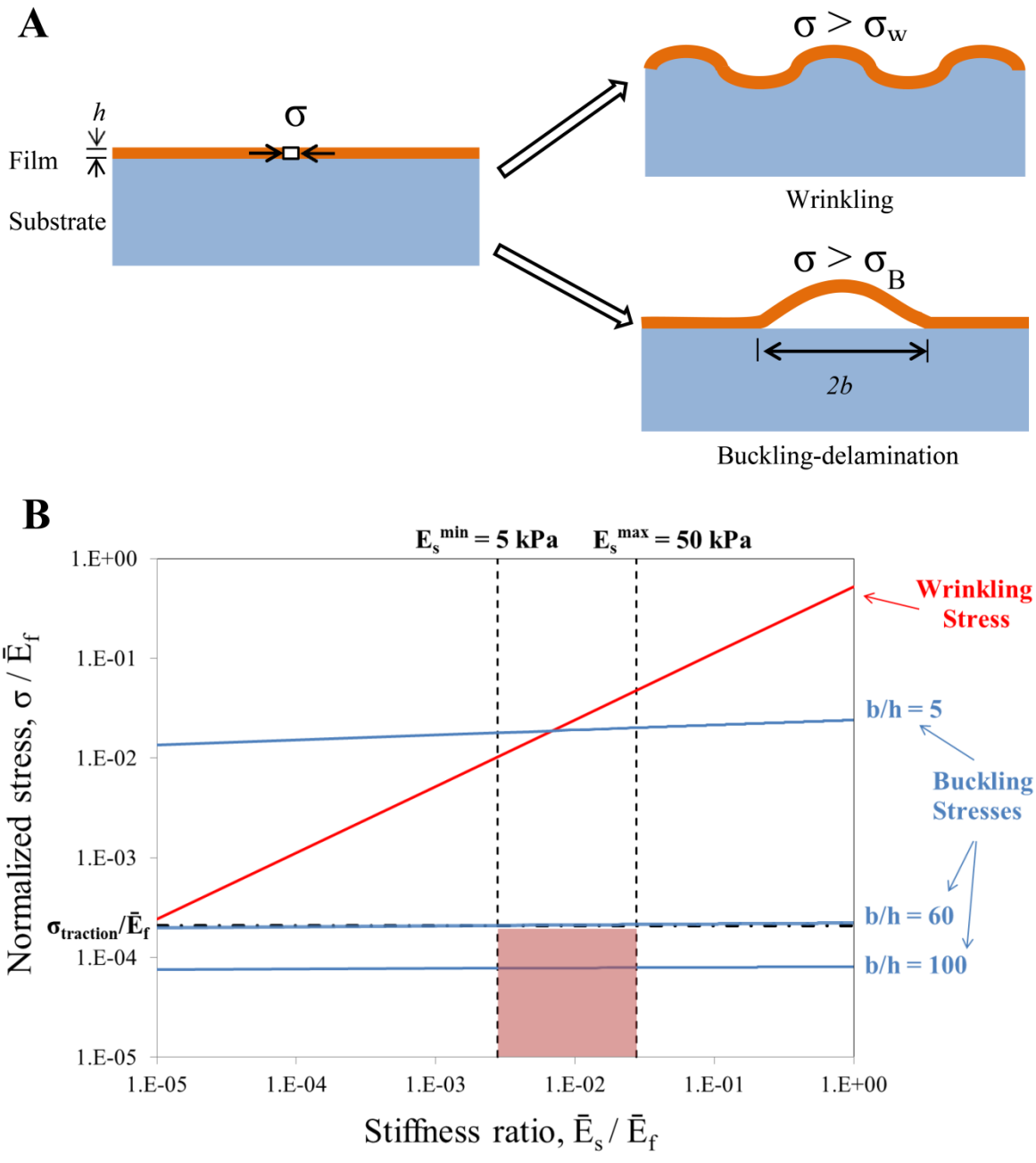

FIGURE 4.4: Wrinkling and delamination modes of buckling in the thin film on substrate system. σ_W and σ_B are the critical stresses for wrinkling and delamination respectively. (b) Critical stresses for wrinkling and buckling delamination for systems with stiffness ratio $\bar{E}_s / \bar{E}_f$. The critical wrinkling stress (red line) and buckling stresses associated with *b/h* ratios of 5, 60 and 100 are plotted. The regime of interest (pink area) in our system is bounded by the dotted vertical lines E_s^{min} = 5 kPa and E_s^{max} = 50 kPa and the dotted horizontal line $\sigma_{traction}/\bar{E}_f$, the known normalized maximum traction force exerted by cells. It can be seen that critical buckling stresses associated with *b/h* ratios of 60 and above can be experienced in our system.

In **Fig. 4.4B**, normalized stresses critical stress, $\sigma/\bar{E}_f$, is plotted against the stiffness ratio $\bar{E}_s / \bar{E}_f$. The plots for wrinkling and buckling delamination for systems with stiffness ratio $\bar{E}_s / \bar{E}_f$ are shown. The critical wrinkling stress (red line) and buckling stresses associated with *b/h* ratios of 5, 60 and 100 are plotted. In our system, we use a Sylgard 184 PDMS membrane with a young's modulus of E_s = 1800 kPa for all the different film-substrate configurations. For the substrate, the properties of Sylgard 527 PDMS was varied to give three different young's modulus values of E_f = 5, 20 and 50 kPa. As such, the region of interest (pink area) in our system as shown in figure 1b is then bounded by the dotted vertical lines E_s^{min} = 5 kPa and E_s^{max} = 50 kPa and the dotted horizontal line $\sigma_{traction}/\bar{E}_f$, the known normalized maximum traction force exerted by cells (143). It can be seen that critical buckling stresses associated with *b/h* ratios of 60 and above can be experienced in our system. In order to prevent buckling-delamination from occuring in our system, we specify a safety factor of 2.5 for the film-substrate system, which translates to satisfying a requirement of $b/h \leq 24$.

4.3.3 Optimization of PDMS thin membrane thickness

Hertz indentation simulations for measuring stiffness were carried out to determine if there were any differences in stiffnesses measured through a PDMS gel bilayer as compared to the measured stiffnesses of the underlying PDMS gel. These differences between the two cases were quantified as a percentage difference in stiffness between the bilayer measurement case and the direct measurement case. **Fig. 4.5, A and B** show the FEA simulations of a steel ball before and after indentation into the underlying substrate in Autodesk Inventor.

To fulfill a requirement of $b/h \leq 24$ for our system, we take b to be bounded and fixed by the maximum radius that a cell can spread on a 2-D substrate (144), which is taken to be 36 μm. Therefore, the only parameter which can be tuned in our system to satisfy the requirement of $b/h \leq 24$ is by increasing h. However, by increasing h, the percentage difference in stiffness of our film-substrate system compared to the stiffness of the substrate (measured by Hertz indentation) increases, as shown in **Fig. 4.5**. We pick a film thickness of $h = 1.5$ μm, thus settling for a maximum percentage difference in stiffness of approximately 6 % for our experiments.

Having chosen all the appropriate film and substrate parameters, which are film material and thickness, substrate material and range of stiffnesses, we now have a system where cell traction-induced wrinkling or buckling-delamination cannot occur, even when transferring the thin film from one underlying substrate to another.

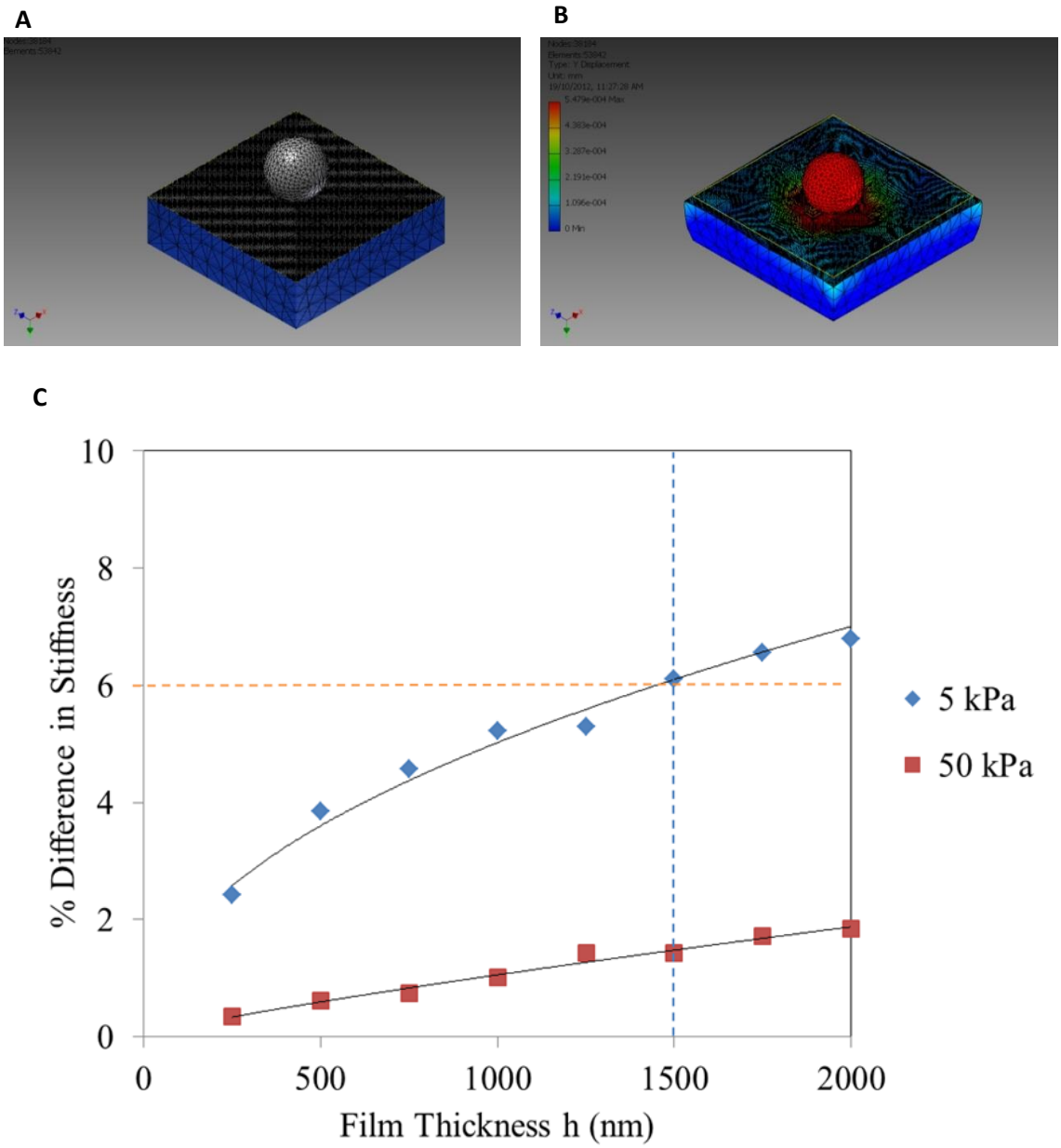

FIGURE 4.5: Hertz indentation FE simulations carried out (A) before and (B) after indentation in Autodesk Inventor. (C) Percentage difference in stiffness of film-substrate systems compared to the stiffness of the substrate, measured by Hertz indentation, plotted against film thickness for film-substrate systems having substrates of 5 kPa and 50 kPa stiffnesses. h = 1500 nm (dotted blue line) and above satisfies the safety factor requirement of 2.5, with respect to a critical buckling

stress associated with a *b/h* ratio of 60 and a maximum allowable *b* of 36 μm based on the maximum known cell spread radius on 2D substrates. The red dotted line denotes the maximum percentage difference in stiffness of our film-substrate system in all cases, which is approximately 6 %.

4.3.4 Stiffnesses of substrate and cell spread area using thin-membrane transplantation method are comparable to those seeded directly on the underlying substrate

Fig. 4.6 compares NIH 3T3 cell characteristics seeded directly on 5, 20 and 50 kPa PDMS substrates with cells seeded on the thin film-PDMS substrate bilayer. **Fig. 4.6A** shows a graph of cell area versus stiffness of the underlying substrate. The control cases when cells were seeded directly on the PDMS substrates for 6 hr are shown by the blue bars. The cell spread area of cells in control cases were compared to those of cells seeded on the thin PDMS films, which were placed on substrates of different stiffnesses for 6 hr (denoted by yellow bars), and those of cells seeded on thin PDMS films which were initially placed on PDMS substrates for 6 hr, then transferred to another substrate with a different stiffness than the initial PDMS substrate after 6 hr (denoted by both red and green bars). A student's t-test was conducted on the datasets, using the cell spread area of cells seeded directly on the 5, 20 and 50 kPa PDMS substrates as controls and the *p*-values of the test are denoted in **Fig. 4.6A**. The cell spread area of cells seeded on the thin PDMS films placed on top of underlying PDMS substrates show no significant difference, based on the *p*-values obtained from the student's t-test at a 90 % confidence level ($p < 0.1$), when compared to the cell spread area of cells which were seeded directly on top of the PDMS substrates. When the cells seeded on top of PDMS films are transferred from one PDMS substrate to another with a different stiffness compared to the original, the cell spread area changes and show no significant difference to those seeded directly on the PDMS substrates

based on the student's t-test at a 90 % confidence level. Cell spread area of cells seeded on the thin membranes and stuck on top of PDMS gels show no significant differences from those seeded directly on top of PDMS substrates. Even when the films are transplanted from one PDMS substrate to another with different stiffness, the cell spread area changes and show no significant different to those seeded directly on the PDMS substrates. This shows that the bilayer system successfully mimics the cell stiffness environment of the PDMS substrate located below the thin PDMS film.

It is noted that the *p*-values of the cell spread area data groups which were compared to the cell spread area of cells seeded directly on 5 kPa PDMS substrates where on average lower than the *p*-values of the cell spread area data groups which were compared to the cell spread area of cells seeded directly on 20 and 50 kPa PDMS substrates respectively, as shown in **Fig. 4.6A**. This means that for cells seeded on the thin PDMS films which were placed on the 50 kPa underlying PDMS substrates, their cell spread area more closely resembled those of cells seeded directly on the 50 kPa PDMS substrates. A reason for this could be that the difference in stiffness of the bilayer system (for thin PDMS films on underlying PDMS substrates) as compared to the stiffness of the underlying PDMS substrates were lower for 50 kPa PDMS substrates than for 5 kPa PDMS substrates, as shown previously in **Fig. 4.5C**. Since cell spread area is known to increase with substrate stiffness, this could explain why cells seeded on the thin PDMS films which were placed on the 50 kPa underlying PDMS substrates had cell spread areas more closely resembled those of cells seeded directly on the 50 kPa PDMS substrates as compared to the 20 and 5 kPa PDMS substrates.

The F-actin structures of cells stained with Alexa-Phallodin for cells seeded on thin PDMS membrane-PDMS substrate bilayers compared to cells seeded directly on 3 PDMS

substrates with differing stiffnesses (1, 20 and 50 kPa) are shown in **Fig. 4.6B**. Stress fibers become more prominent in both cases where the stiffness of the underlying substrates are increased, further demonstrating that the cells can sense the stiffness of their underlying substrate layer below the PDMS membrane.

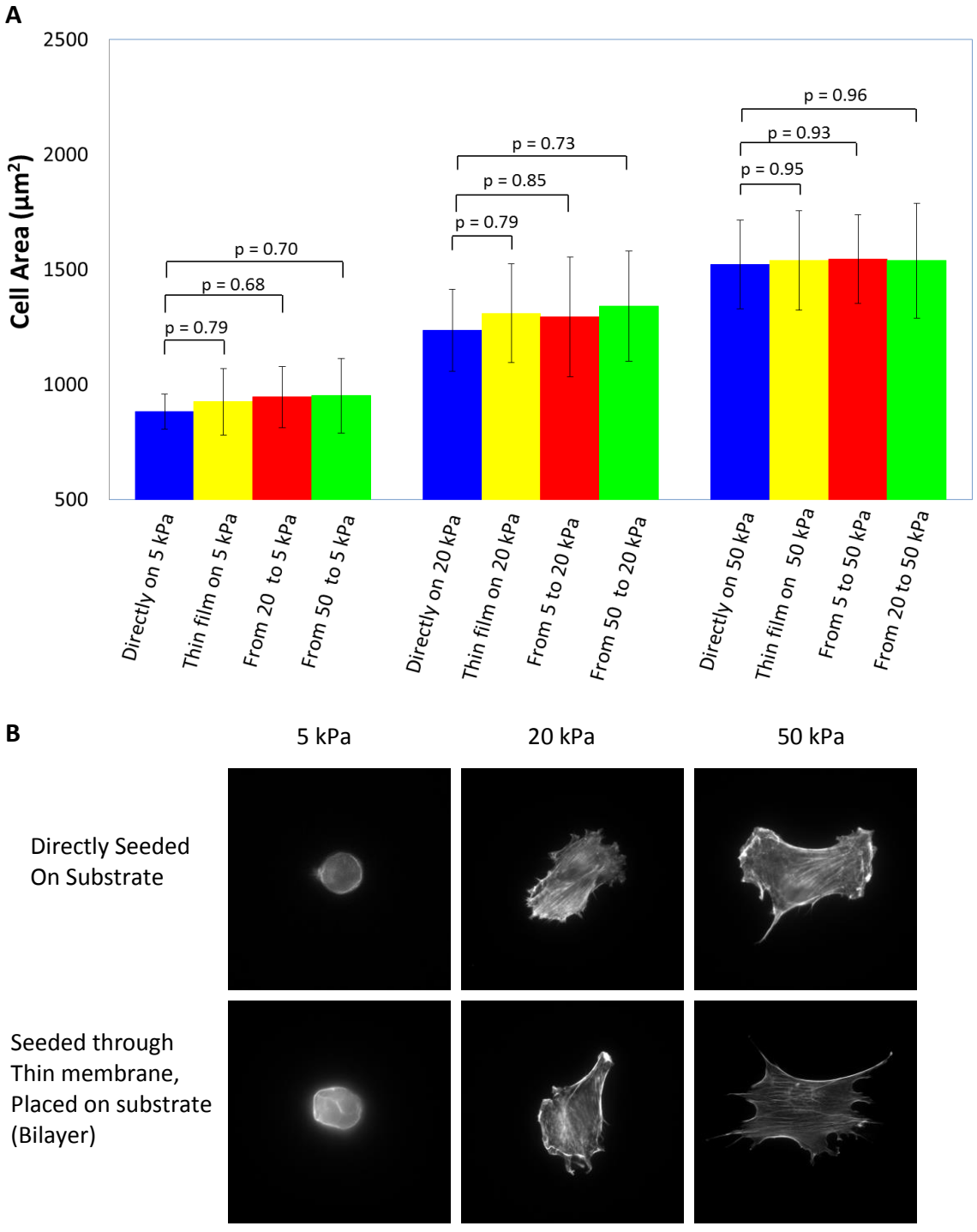

FIGURE 4.6: Comparisons between NIH 3T3 cell characteristics when seeded directly on 5, 20 and 50 kPa PDMS substrates and when seeded through the thin film-

PDMS substrate bilayers. (A) Graph of cell area versus stiffness of the underlying substrate. Control cases when cells were seeded directly on the PDMS substrates for 6 hr (blue) were compared to those seeded on the thin films which were then placed on substrates of different stiffnesses for 6 hr (yellow), and cells seeded on thin films which were placed on PDMS substrates for 6 hr, and then transferred to another substrate with a different stiffness than the original after 6 hr (red, green). It can be seen that cell spread area of cells seeded on the thin membranes placed on top of PDMS substrate (bilayer) show no significant difference, based on the *p*-values obtained from the student's t-test at a 90 % confidence level ($p < 0.1$), from those seeded directly on top of the PDMS gels. When the membranes are transferred from one PDMS substrate to another with a different stiffness, the cell spread area changes and show no significant difference to those seeded directly on the PDMS gels. (B) F-actin staining for 3 stiffnesses for direct versus through membrane cell seeding on PDMS gels. (Bars denoted standard error. n=30)

4.4 Conclusion

In this study, we have demonstrated the ability to modulate substrate stiffness dynamically in 2-D based on the fact the cells can sense through thin and pliable substrates. We fabricated thin PDMS membranes within thicknesses of up to 100 nm based on a novel method utilizing techniques in soft lithography. FEA simulations were done to optimize the PDMS membrane thickness and stiffness parameters that we would proceed to use in the experiments.

Our preliminary results for cell studies using this dynamic stiffness method reveal that cell spread area and stress fiber formation for cells seeded on the PDMS membrane-PDMS gel bilayers were comparable to cells seeded directly on PDMS gel substrates. This system can be used to conduct more novel studies on cell response to dynamic substrate stiffness. For example,

the response of neurite outgrowth as well as myofibroblasts to dynamic and reversible changing stiffness can be investigated, which would potentially provide insight into various conditions such as neural diseases and fibrosis.

Chapter 5

Conclusion and Future Work

5.1 Conclusion

In chapter 1, we looked at how cells interact with their environment. The transmembrane proteins, integrins and cadherins, which link the extracellular environment and other cells respectively to the cell cytoskeleton, are discussed. The various environmental niches for different tissues in the body with differing extracellular stiffnesses and their importance in cell proliferation, differentiation and survival were looked at. The major component of the internal cell structure, the cytoskeleton, which consists in part by actin, and the various actin-rich structures in cells such as lamellipodia, filopodia, podosomes and stress fibers were discussed. How the tuning of extracellular environment stiffness affects cell behavior such as cell migration speed, spread area and stem cell differentiation was looked at. Lastly, we focused specifically on the structure and functions of the actin-rich CDRs within cells, and how they have been implicated in cell migration and macropinocytosis.

In chapter 2, CDR behavior is investigated through varying substrate stiffness and the construction of a mathematical model. The dynamics and mechanism of formation of CDRs are still unknown. It has been observed that CDR formation leads to stress fibers disappearing near the CDRs. Because stress fiber formation can be modified by substrate stiffness, we examined the effect of substrate stiffness on CDR formation by seeding NIH 3T3 fibroblasts on glass and polydimethylsiloxane substrates of varying stiffnesses from 20 kPa to 1800 kPa. We found that increasing substrate stiffness increased the lifetime of the CDRs. We developed a mathematical model of the signaling pathways involved in CDR formation to provide insight into this lifetime and size dependence that is linked to substrate stiffness via Rac-Rho antagonism. From the model, increasing stiffness raised mDia1-nucleated stress fiber formation due to Rho activation. The increased stress fibers present increased replenishment of the G-actin pool, therefore prolonging Arp2/3-nucleated CDR formation due to Rac activation. Negative feedback by WAVE-related RacGAP on Rac explained how CDR actin propagates as an excitable wave, much like wave propagation in other excitable medium, for example, in nerve signal transmission.

In chapter 3, the role of CDR formation in cell motility is investigated for NIH 3T3 fibroblasts seeded on 10 kPa PA substrates. We found that CDR formation increases cell migration directional persistency but did not affect the migration speed. Furthermore, an increase in the localization of lamellipodia protrusion at the cell edge in the vicinity of the CDRs was observed. Relocalization of lamellipodia occurs 1 to 6 min after CDR formation with the structural reorganization of the lamellipodia protrusion increasing at the cell edge closest to the site of CDR formation while decreasing at the opposite side at the cell periphery. The time lag between peak CDR formation and the proceeding peak lamellipodia protrusion is then correlated

with the spatial distance between the CDR and the lamellipodia; this time scale is consistent with the diffusive time scale of cytosolic G-actin. Using FRAP, we confirmed that the increase in localized lamellipodia formation in the cell appears to correlate to the transport of G-actin from the CDRs to the lamellipodia. These findings shed light on the complex interplay between actin structures in cell behavior and have implications in a range of fields including cell motility, actin biophysics, and biological materials.

In chapter 4, we demonstrated the modulation of substrate stiffness dynamically in 2-D based on the fact the cells are able to sense through thin and compliant substrates. The fabrication and characterization of thin PDMS-underlying substrate bilayer systems was demonstrated, as well as the measurement of the mechanical stiffness of the bilayer system using FEA simulated in Autodesk (Autodesk, Inc.). In addition, the possible delamination of the PDMS bilayer system is investigated and an optimal set of physical parameters for the bilayer was determined, such that delamination of the thin membrane from the underlying PDMS substrate does not occur during cell culture in 2-D. The optimal thickness of the thin membrane was selected as 1.5 μm. We investigated the effect of dynamically changing substrate stiffness on the morphology of 3T3 cells using the thin membrane-PDMS substrate bilayer system and found that reveal that cell spread area and stress fiber formation for cells seeded on the PDMS membrane-PDMS gel bilayers were comparable to cells seeded directly on PDMS gel substrates. The potential of this system to study other cell response to dynamic substrate stiffness, such as that of neurite outgrowth and myofibroblasts is discussed, which would have potential is providing further insight into conditions such as neural diseases and fibrosis.

5.2 Future Work

5.2.2 Future work involving migrational persistence of CDRs

In chapter 3, the role of CDRs in increasingly migrational persistence of single 3T3 cells is elucidated. It is interesting to note that the increase in migrational persistence behaviour of single cells exhibiting CDRs as compared to cells not exhibiting CDRs does not extend to that of cells in a scratch wound assay, as shown in **Fig. 5.1**. Confluent 3T3 cells on a petri dish surface were scratched to form a wound healing assay, and PDGF is added to stimulate CDR formation in some of the cells at the leading edge of the wound as shown in **Fig. 5.1A**. The red arrows point to cells which exhibit CDRs after PDGF stimulation. The wound is observed for up to 6 hours till closure as shown in **Fig. 5.1B**, and the migrational speed and persistence are obtained using the methods described in chapter 3. A control wound healing case is also conducted using cells which were not stimulated with PDGF, 0 and 6 hrs after wound formation as shown in **Fig. 5.1C** and **Fig. 5.1D** respectively.

From the data collected from the scratch wound assays, the mean migration speed and persistence of the cells stimulated with PDGF and exhibiting CDRs, stimulated with PDGF but not exhibiting CDRs and the control case are obtained and shown in **Fig. 5.2A** and **Fig. 5.2B** respectively, with 15 cells in each case. It can be seen that mean cell migration speed and cell migrational persistence are not statistically significantly different (using the student's t-test at the $p = 0.1$ confidence level), suggesting that although cell migrational persistence is increased for single cells exhibiting CDRs, this is not the case for cells exhibiting CDRs at the leading edge of a scratch wound assay. Why this is so remains unknown and could be the focus of future work.

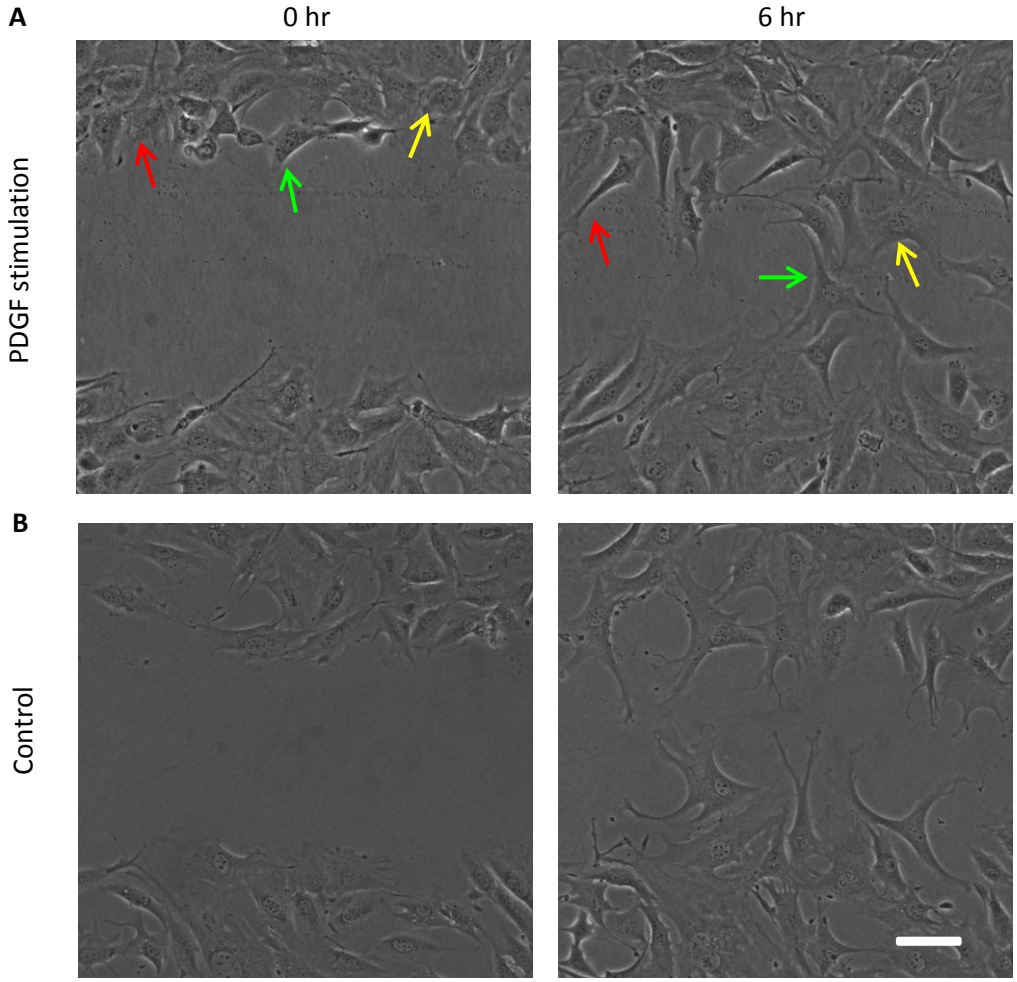

FIGURE 5.1: Phase contrast images of NIH 3T3 cells in scratch wound assays with and without PDGF stimulation. (A) Cells stimulated with PDGF 0 and 6 hr after scratch, with arrows denoted three different individual cells exhibiting CDRs. (B) Cells without PDGF stimulation 0 and hr hr after scratch. (Scale bar = 20 μm)

Since the difference between single cells and cells in a scratch wound assay is the presence of cell-cell mediated contacts, for example, through cadherins, in cells present in scratch wound assays, any future work on why migrational persistence is increased in single cells exhibiting CDRs but not in leading edge cells exhibiting CDRs in a scratch wound assay could focus on

these cell-cell contacts. A first experiment could be conducted in which cadherins are knocked down or inactivated in a scratch wound assay, and the migrational speed and persistence of the cells exhibiting CDRs observed. If the absence of cell-cell contacts causes an increase in migrational persistence of CDR-exhibiting cells as compared to the control cells, it would show that cell-cell contacts such as cadherins are somehow responsible for the CDR-induced migrational persistence in cells.

A

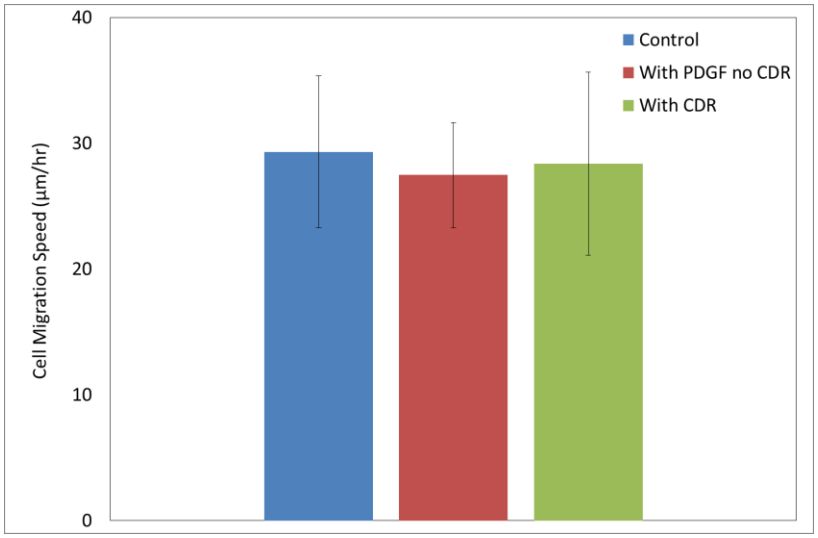

B

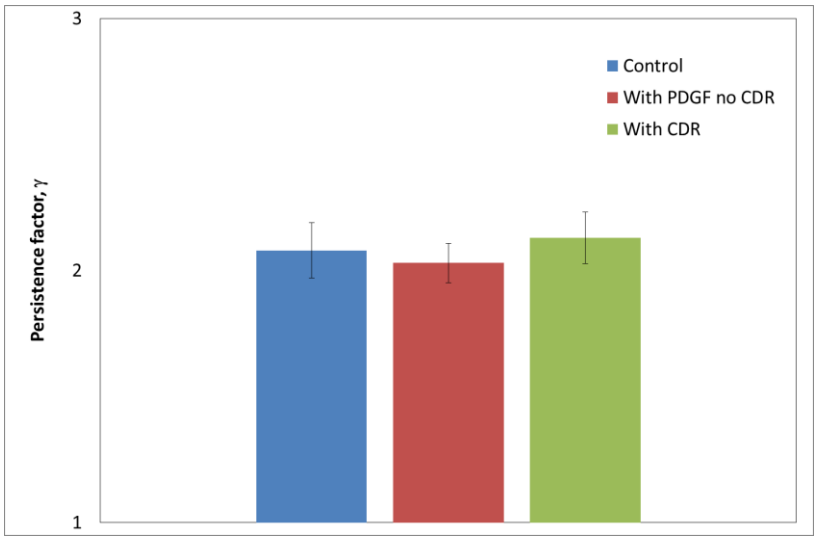

FIGURE 5.2: Mean cell migration speed and migrational persistence, γ, for cells in scratch wound assay. (A) Mean migration speed over a 6 hr period for cells exhibiting CDRs, cells stimulated with PDGF but not exhibiting CDRs and for control cells. (B) Migration persistence, γ, for cells over a 6 hr period exhibiting CDRs, cells stimulated with PDGF but not exhibiting CDRs and for control cells. (Bars denote standard error, n = 15)

5.2.2 Future work involving the modulation of substrate stiffness dynamically for cell studies

Future work could be done involving the modulation of substrate stiffness dynamically through the thin membrane-PDMS substrate system. The characterization of well-known NIH 3T3 cell properties with regards to substrate stiffness could be investigated using the dynamic stiffness membrane system. For example, cell traction forces, mean cell focal adhesion sizes and cell migration speeds could be quantified and compared for cells seeded on the thin membrane-PDMS substrate bilayer and for cells seeded directly on the PDMS substrates. If the differences in these quantities in the two cases are not statistically significant, it can be concluded that the thin membrane-PDMS substrate bilayer system successfully mimics the conditions of cells being seeded directly on the underlying PDMS substrates.

The effects of long stiffness pulses (12 hr intervals), where the stiffness of the substrate is switched from soft to hard and vice versa, on cell properties such as the average cell area in the population, mean focal adhesion sizes and mean migration speed could also be looked at. From the data, the time constants of these three quantities for the response of cells to the long pulse in substrate stiffness could be obtained. The response of these same quantities can be obtained in response to shorter pulses (1, 2 and 3 hr intervals) of changing substrate stiffnesses. The data

from such experiments would provide insight into how quickly the cell as well as their structures such as focal adhesion complexes response to changing stiffness of the environment.

The ability of neurons to respond to their external environment is important in neural outgrowth during neural development as well as regeneration. It has been shown that neurite outgrowth can be affected by the stiffness of the substrates in which differentiating neuroblasts are seeded on (145). These same pulses in changing substrate stiffnesses using the bilayer system as mentioned previously could also be applied to study these neuroblasts, and how their neurite outgrowths are affected by the application of these pulses.

Bibliography

1. Yeung, T., Georges, P. C., Flanagan, L. A., Marg, B., Ortiz, M., Funaki, M., Zahir, N., et al. (2005). Effects of substrate stiffness on cell morphology, cytoskeletal structure, and adhesion. *Cell Motility and the Cytoskeleton*, *60*(1), 24-34.
2. Lo, C. M., Wang, H. B., Dembo, M., & Wang, Y. L. (2000). Cell movement is guided by the rigidity of the substrate. *Biophysical journal*, *79*(1), 144-152.
3. Huang, H., Kamm, R. D., & Lee, R. T. (2004). Cell mechanics and mechanotransduction: pathways, probes, and physiology. *American Journal of Physiology-Cell Physiology*, *287*(1), C1-C11.
4. Wang, J. H. C., & Thampatty, B. P. (2006). An introductory review of cell mechanobiology. *Biomechanics and modeling in mechanobiology*, *5*(1), 1-16.
5. Engler, A. J., Sen, S., Sweeney, H. L., & Discher, D. E. (2006). Matrix elasticity directs stem cell lineage specification. *Cell*, 126(4), 677-689.
6. Butcher, D. T., Alliston, T., & Weaver, V. M. (2009). A tense situation: forcing tumour progression. *Nature Reviews Cancer*, 9(2), 108-122.
7. Bruce A., Alexander J., Julian L., et al. (2007). *Molecular biology of the cell*. New York, NY: Garland Science.
8. Lodish, H. F., Arnold, B., Chris, A.K., et al. (2007). *Molecular Cell Biology*. New York, NY: WH Freeman.
9. Rodriguez, O. C., Schaefer, A. W., Mandato, C. A., Forscher, P., Bement, W. M., & Waterman-Storer, C. M. (2003). Conserved microtubule–actin interactions in cell movement and morphogenesis. *Nature cell biology*, *5*(7), 599-609.
10. Revenu, C., Athman, R., Robine, S., & Louvard, D. (2004). The co-workers of actin filaments: from cell structures to signals. *Nature Reviews Molecular Cell Biology*, *5*(8), 635-646.
11. Wang, J. H. C., Thampatty, B. P., Lin, J. S., & Im, H. J. (2007). Mechanoregulation of gene expression in fibroblasts. *Gene*, *391*(1), 1-15.
12. Nürnberg, A., Kitzing, T., & Grosse, R. (2011). Nucleating actin for invasion.*Nature Reviews Cancer*, *11*(3), 177-187.

13. Buccione, R., Orth, J. D., & McNiven, M. A. (2004). Foot and mouth: podosomes, invadopodia and circular dorsal ruffles. *Nature Reviews Molecular Cell Biology*, *5*(8), 647-657.
14. Nobes, C. D., & Hall, A. (1995). Rho, rac, and cdc42 GTPases regulate the assembly of multimolecular focal complexes associated with actin stress fibers, lamellipodia, and filopodia. *Cell*, 81(1), 53.
15. Hotulainen, P., & Lappalainen, P. (2006). Stress fibers are generated by two distinct actin assembly mechanisms in motile cells. *The Journal of Cell Biology*, 173(3), 383-394.
16. Small, J. V., Stradal, T., Vignal, E., & Rottner, K. (2002). The lamellipodium: where motility begins. *Trends in Cell Biology*, 12(3), 112-120.
17. Sheng, S., Carey, J., Seftor, E. A., Dias, L., Hendrix, M. J., & Sager, R. (1996). Maspin acts at the cell membrane to inhibit invasion and motility of mammary and prostatic cancer cells. *Proceedings of the National Academy of Sciences*, 93(21), 11669-11674.
18. Tarone, G., Cirillo, D., Giancotti, F. G., Comoglio, P. M., & Marchisio, P. C. (1985). Rous sarcoma virus-transformed fibroblasts adhere primarily at discrete protrusions of the ventral membrane called podosomes. *Experimental Cell Research*, *159*(1), 141-157.
19. David-Pfeuty, T., & Singer, S. J. (1980). Altered distributions of the cytoskeletal proteins vinculin and alpha-actinin in cultured fibroblasts transformed by Rous sarcoma virus. *Proceedings of the National Academy of Sciences*, *77*(11), 6687-6691.
20. Marchisio, P. C., Cirillo, D., Naldini, L., Primavera, M. V., Teti, A., & Zambonin-Zallone, A. (1984). Cell-substratum interaction of cultured avian osteoclasts is mediated by specific adhesion structures. *The Journal of Cell Biology*, *99*(5), 1696-1705.
21. Marchisio, P. C., Cirillo, D., Teti, A., Zambonin-Zallone, A., & Tarone, G. (1987). Rous sarcoma virus-transformed fibroblasts and cells of monocytic origin display a peculiar dot-like organization of cytoskeletal proteins involved in microfilament-membrane interactions. *Experimental Cell Research*, *169*(1), 202-214.
22. Spinardi, L., Rietdorf, J., Nitsch, L., Bono, M., Tacchetti, C., Way, M., & Marchisio, P. C. (2004). A dynamic podosome-like structure of epithelial cells. *Experimental Cell Research*, *295*(2), 360-374.
23. Chen, W. T. (1989). Proteolytic activity of specialized surface protrusions formed at rosette contact sites of transformed cells. *Journal of Experimental Zoology*, *251*(2), 167-185.

24. Mueller, S. C., & Chen, W. T. (1991). Cellular invasion into matrix beads: localization of beta 1 integrins and fibronectin to the invadopodia. *Journal of Cell Science*, *99*(2), 213-225.
25. Parri, M., & Chiarugi, P. (2010). Rac and Rho GTPases in cancer cell motility control. *Cell Commun Signal*, *8*, 23.
26. Chhabra, E. S., & Higgs, H. N. (2007). The many faces of actin: matching assembly factors with cellular structures. *Nature Cell Biology*, 9(10), 1110-1121.
27. Georges, P. C., & Janmey, P. A. (2005). Cell type-specific response to growth on soft materials. *Journal of Applied Physiology*, *98*(4), 1547-1553.
28. LeDuc, P. R., & Bellin, R. R. (2006). Nanoscale intracellular organization and functional architecture mediating cellular behavior. *Annals of Biomedical Engineering*, *34*(1), 102-113.
29. Beningo, K. A., & Wang, Y. L. (2002). Flexible substrata for the detection of cellular traction forces. *Trends in Cell Biology*, *12*(2), 79-84.
30. Brown, X. Q., Ookawa, K., & Wong, J. Y. (2005). Evaluation of polydimethylsiloxane scaffolds with physiologically-relevant elastic moduli: interplay of substrate mechanics and surface chemistry effects on vascular smooth muscle cell response. *Biomaterials*, *26*(16), 3123-3129.
31. Balaban, N. Q., Schwarz, U. S., Riveline, D., Goichberg, P., Tzur, G., Sabanay, I., & Geiger, B. (2001). Force and focal adhesion assembly: a close relationship studied using elastic micropatterned substrates. *Nature Cell Biology*, 3(5), 466-472.
32. Chou, S. Y., Cheng, C. M., & LeDuc, P. R. (2009). Composite polymer systems with control of local substrate elasticity and their effect on cytoskeletal and morphological characteristics of adherent cells. *Biomaterials*, *30*(18), 3136-3142.
33. Beningo, K. A., Dembo, M., Kaverina, I., Small, J. V., & Wang, Y. L. (2001). Nascent focal adhesions are responsible for the generation of strong propulsive forces in migrating fibroblasts. *The Journal of Cell Biology*, *153*(4), 881-888.
34. Cassino, T. R., Drowley, L., Okada, M., Beckman, S. A., Keller, B., Tobita, K., LeDuc, P. R., et al. (2012). Mechanical loading of stem cells for improvement of transplantation outcome in a model of acute myocardial infarction: the role of loading history. *Tissue Engineering Part A*, *18*(11-12), 1101-8.

35. Turner, D. C., Lawton, J., Dollenmeier, P., Ehrismann, R., & Chiquet, M. (1983). Guidance of myogenic cell migration by oriented deposits of fibronectin. *Developmental Biology*, *95*(2), 497-504.
36. Nakatsuji, N., & Johnson, K. E. (1984). Experimental manipulation of a contact guidance system in amphibian gastrulation by mechanical tension. *Nature*, *307*(5950), 453-455.
37. Rajnicek, A., Britland, S., & McCaig, C. (1997). Contact guidance of CNS neurites on grooved quartz: influence of groove dimensions, neuronal age and cell type. *Journal of Cell Science*, *110*(23), 2905-2913.
38. Teixeira, A. I., Abrams, G. A., Bertics, P. J., Murphy, C. J., & Nealey, P. F. (2003). Epithelial contact guidance on well-defined micro-and nanostructured substrates. *Journal of cell science*, *116*(10), 1881-1892.
39. Khademhosseini, A., Langer, R., Borenstein, J., & Vacanti, J. P. (2006). Microscale technologies for tissue engineering and biology. *Proceedings of the National Academy of Sciences of the United States of America*, *103*(8), 2480-2487.
40. Walker, G. M., Zeringue, H. C., & Beebe, D. J. (2004). Microenvironment design considerations for cellular scale studies. *Lab Chip*, 4(2), 91-97.
41. Genzer, J., & Groenewold, J. (2006). Soft matter with hard skin: From skin wrinkles to templating and material characterization. *Soft Matter*, 2(4), 310-323.
42. Sniadecki, N. J., Desai, R. A., Ruiz, S. A., & Chen, C. S. (2006). Nanotechnology for cell–substrate interactions. *Annals of Biomedical Engineering*, 34(1), 59-74.
43. Bettinger, C. J., Langer, R., & Borenstein, J. T. (2009). Engineering substrate topography at the micro-and nanoscale to control cell function. *Angewandte Chemie International Edition*, 48(30), 5406-5415.
44. Lim, J. Y., & Donahue, H. J. (2007). Cell sensing and response to micro-and nanostructured surfaces produced by chemical and topographic patterning. *Tissue Engineering*, 13(8), 1879-1891.
45. Tse, J. R., & Engler, A. J. (2010). Preparation of hydrogel substrates with tunable mechanical properties. *Current Protocols in Cell Biology*, 10-16.
46. Hinz, B. (2007). Formation and function of the myofibroblast during tissue repair. *Journal of Investigative Dermatology*, *127*(3), 526-537.

47. Frey, M. T., & Wang, Y. L. (2009). A photo-modulatable material for probing cellular responses to substrate rigidity. *Soft Matter*, *5*(9), 1918-1924.
48. Guvendiren, M., & Burdick, J. A. (2012). Stiffening hydrogels to probe short-and long-term cellular responses to dynamic mechanics. *Nature Communications*, 3, 792.
49. Krekhova, M., Lang, T., Richter, R., & Schmalz, H. (2010). Thermoreversible hydroferrogels with tunable mechanical properties utilizing block copolymer mesophases as template. *Langmuir*, 26(24), 19181-19190.
50. Yamaizumi, M., & Sugano, T. (1994). UV-induced nuclear accumulation of p53 is evoked through DNA damage of actively transcribed genes independent of the cell cycle. *Oncogene*, 9(10), 2775-2784.
51. Mellström, K., Heldin, C. H., & Westermark, B. (1988). Induction of circular membrane ruffling on human fibroblasts by platelet-derived growth factor. *Experimental Cell Research*, *177*(2), 347-359.
52. Mellström, K., Höglund, A. S., Nistér, M., Heldin, C. H., Westermark, B., & Lindberg, U. (1983). The effect of platelet-derived growth factor on morphology and motility of human glial cells. *Journal of Muscle Research & Cell Motility*, *4*(5), 589-609.
53. Tamura, M., & Iwamoto, Y. (1989). The effect of platelet-derived growth factor on phagocytosis of cultured human trabecular cells. *Experimental Eye Research*,*48*(6), 761-770.
54. Araki, N., Egami, Y., Watanabe, Y., & Hatae, T. (2007). Phosphoinositide metabolism during membrane ruffling and macropinosome formation in EGF-stimulated A431 cells. *Experimental Cell Research*, *313*(7), 1496-1507.
55. Arvidsson, A. K., Rupp, E., Nånberg, E., Downward, J., Rönnstrand, L., Wennström, S., ... & Claesson-Welsh, L. (1994). Tyr-716 in the platelet-derived growth factor beta-receptor kinase insert is involved in GRB2 binding and Ras activation. *Molecular and Cellular Biology*, *14*(10), 6715-6726.
56. Dharmawardhane, S., Sanders, L. C., Martin, S. S., Daniels, R. H., & Bokoch, G. M. (1997). Localization of p21-activated kinase 1 (PAK1) to pinocytic vesicles and cortical actin structures in stimulated cells. *The Journal of Cell Biology*, *138*(6), 1265-1278.
57. Krueger, E. W., Orth, J. D., Cao, H., & McNiven, M. A. (2003). A dynamin–cortactin–Arp2/3 complex mediates actin reorganization in growth factor-stimulated cells. *Molecular Biology of the Cell*, *14*(3), 1085-1096.

58. Bereiter-Hahn, J., Strohmeier, R., Kunzenbacher, I., Beck, K., & Vöth, M. (1981). Locomotion of Xenopus epidermis cells in primary culture. *Journal of Cell Science*, *52*, 289-311.
59. Soranno, T., & Bell, E. (1982). Cytostructural dynamics of spreading and translocating cells. *The Journal of Cell Biology*, *95*(1), 127-136.
60. Marchisio, P. C., Capasso, O., Nitsch, L., Cancedda, R., & Gionti, E. (1984). Cytoskeleton and adhesion patterns of cultured chick embryo chondrocytes during cell spreading and Rous sarcoma virus transformation. *Experimental Cell Research*, *151*(2), 332-343.
61. Hedberg, K. M., Bengtsson, T., Safiejko-Mroczka, B., Bell, P. B., & Lindroth, M. (1993). PDGF and neomycin induce similar changes in the actin cytoskeleton in human fibroblasts. *Cell Motility and the Cytoskeleton*, *24*(2), 139-149.
62. Ballestrem, C., Wehrle-Haller, B., & Imhof, B. A. (1998). Actin dynamics in living mammalian cells. *Journal of Cell Science*, *111*(12), 1649-1658.
63. Gu, Z., Noss, E. H., Hsu, V. W., & Brenner, M. B. (2011). Integrins traffic rapidly via circular dorsal ruffles and macropinocytosis during stimulated cell migration. *The Journal of Cell Biology*, *193*(1), 61-70.
64. Falcone, S., Cocucci, E., Podini, P., Kirchhausen, T., Clementi, E., & Meldolesi, J. (2006). Macropinocytosis: regulated coordination of endocytic and exocytic membrane traffic events. *Journal of Cell Science*, *119*(22), 4758-4769.
65. Dowrick, P., Kenworthy, P., McCann, B., & Warn, R. (1993). Circular ruffle formation and closure lead to macropinocytosis in hepatocyte growth factor/scatter factor-treated cells. *European Journal of Cell Biology*, *61*(1), 44
66. Warn, R., Brown, D., Dowrick, P., Prescott, A., & Warn, A. (1993). Cytoskeletal changes associated with cell motility. *Symposia of the Society for Experimental Biology*, *47*, 325-338.
67. Orth, J. D., Krueger, E. W., Weller, S. G., & McNiven, M. A. (2006). A novel endocytic mechanism of epidermal growth factor receptor sequestration and internalization. *Cancer Research*, *66*(7), 3603-3610.
68. Orth, J. D., & McNiven, M. A. (2006). Get off my back! Rapid receptor internalization through circular dorsal ruffles. *Cancer Research*, 66(23), 11094-11096.
69. Ruusala, A., Sundberg, C., Arvidsson, A. K., Rupp-Thuresson, E., Heldin, C. H., & Claesson-Welsh, L. (1998). Platelet-derived growth factor (PDGF)-induced actin

rearrangement is deregulated in cells expressing a mutant Y778F PDGF beta-receptor. *Journal of Cell Science*, *111*(1), 111-120.

70. Hooshmand-Rad, R., Claesson-Welsh, L., Wennström, S., Yokote, K., Siegbahn, A., & Heldin, C. H. (1997). Involvement of phosphatidylinositide 3′-kinase and Rac in platelet-derived growth factor-induced actin reorganization and chemotaxis. *Experimental Cell Research*, *234*(2), 434-441.
71. Moes, M., Boonstra, J., & Regan-Klapisz, E. (2010). Novel role of cPLA2α in membrane and actin dynamics. *Cellular and Molecular Life Sciences*, *67*(9), 1547-1557.
72. Burridge, K., & K.Wennerberg. 2004. Rho and Rac take center stage. *Cell*. 116:167–179.
73. Takai, Y., Sasaki, T., & Matozaki, T. (2001). Small GTP-binding proteins. *Physiological Reviews*, *81*(1), 153-208.
74. Discher, D. E., Janmey, P., & Wang, Y. L. (2005). Tissue cells feel and respond to the stiffness of their substrate. *Science*, *310*(5751), 1139-1143.
75. Yeung, T., Georges, P. C., Flanagan, L. A., Marg, B., Ortiz, M., Funaki, M., Zahir, N., et al. (2005). Effects of substrate stiffness on cell morphology, cytoskeletal structure, and adhesion. *Cell Motility and the Cytoskeleton*, *60*(1), 24-34.
76. Brown, X. Q., Ookawa, K., & Wong, J. Y. (2005). Evaluation of polydimethylsiloxane scaffolds with physiologically-relevant elastic moduli: interplay of substrate mechanics and surface chemistry effects on vascular smooth muscle cell response. *Biomaterials*, *26*(16), 3123-3129.
77. Armani, D., Liu, C., & Aluru, N. (1999). Re-configurable fluid circuits by PDMS elastomer micromachining. *Technical Digest IEEE International MEMS 99 Conference Twelfth IEEE International Conference on Micro Electro Mechanical Systems Cat No99CH36291*, 222-227.
78. Pelham, R. J., & Wang, Y. L. (1997). Cell locomotion and focal adhesions are regulated by substrate flexibility. *Proceedings of the National Academy of Sciences*, *94*(25), 13661-13665.
79. LeDuc, P. R., Messner, W. C., & Wikswo, J. P. (2011). How do control-based approaches enter into biology?. *Annual Review of Biomedical Engineering*, *13*, 369-396.
80. Lin, Y. W., Cheng, C. M., LeDuc, P. R., & Chen, C. C. (2009). Understanding sensory nerve mechanotransduction through localized elastomeric matrix control. *PLoS One*, *4*(1), e4293.

81. Auger, K. R., Serunian, L. A., Soltoff, S. P., Libby, P., & Cantley, L. C. (1989). PDGF-dependent tyrosine phosphorylation stimulates production of novel polyphosphoinositides in intact cells. *Cell*, *57*(1), 167-175.
82. Hawkins, P. T., Eguinoa, A., Qiu, R. G., Stokoe, D., Cooke, F. T., Walters, R., Wennström, S., et al. (1995). PDGF stimulates an increase in GTP-Rac via activation of phosphoinositide 3-kinase. *Current Biology*, *5*(4), 393-403.
83. Gamba, A., de Candia, A., Di Talia, S., Coniglio, A., Bussolino, F., & Serini, G. (2005). Diffusion-limited phase separation in eukaryotic chemotaxis. *Science Signaling*, *102*(47), 16927.
84. Suetsugu, S., Yamazaki, D., Kurisu, S., & Takenawa, T. (2003). Differential roles of WAVE1 and WAVE2 in dorsal and peripheral ruffle formation for fibroblast cell migration. *Developmental Cell*, *5*(4), 595-609.
85. Eden, S., Rohatgi, R., Podtelejnikov, A. V., Mann, M., & Kirschner, M. W. (2002). Mechanism of regulation of WAVE1-induced actin nucleation by Rac1 and Nck. *Nature*, *418*(6899), 790-793.
86. Takenawa, T., & Suetsugu, S. (2007). The WASP–WAVE protein network: connecting the membrane to the cytoskeleton. *Nature Reviews Molecular Cell Biology*, *8*(1), 37-48.
87. Cicchetti, P., Ridley, A. J., Zheng, Y., Cerione, R. A., & Baltimore, D. (1995). 3BP-1, an SH3 domain binding protein, has GAP activity for Rac and inhibits growth factor-induced membrane ruffling in fibroblasts. *The EMBO Journal*,*14*(13), 3127.
88. Richnau, N., & Aspenström, P. (2001). Rich, a rho GTPase-activating protein domain-containing protein involved in signaling by Cdc42 and Rac1. *Journal of Biological Chemistry*, *276*(37), 35060-35070.
89. Soderling, S. H., Binns, K. L., Wayman, G. A., Davee, S. M., Ong, S. H., Pawson, T., & Scott, J. D. (2002). The WRP component of the WAVE-1 complex attenuates Rac-mediated signalling. *Nature Cell Biology*, *4*(12), 970-975.
90. Bustos, R. I., Forget, M. A., Settleman, J. E., & Hansen, S. H. (2008). Coordination of Rho and Rac GTPase function via p190B RhoGAP. *Current Biology*, *18*(20), 1606-1611.
91. Ohta, Y., Hartwig, J. H., & Stossel, T. P. (2006). FilGAP, a Rho-and ROCK-regulated GAP for Rac binds filamin A to control actin remodelling. *Nature Cell Biology*, *8*(8), 803-814.

92. Katoh, K., Kano, Y., & Ookawara, S. (2007). Rho-kinase dependent organization of stress fibers and focal adhesions in cultured fibroblasts. *Genes to Cells*, *12*(5), 623-638.
93. Tomar, A., & Schlaepfer, D. D. (2009). Focal adhesion kinase: switching between GAPs and GEFs in the regulation of cell motility. *Current Opinion in Cell Biology*, *21*(5), 676-683.
94. Friedland, J. C., Lee, M. H., & Boettiger, D. (2009). Mechanically activated integrin switch controls alpha5beta1 function. *Science*, *323*(5914), 642-644.
95. Khatiwala, C. B., Peyton, S. R., & Putnam, A. J. (2006). Intrinsic mechanical properties of the extracellular matrix affect the behavior of pre-osteoblastic MC3T3-E1 cells. *American Journal of Physiology-Cell Physiology*, *290*(6), C1640-C1650.
96. Schneider, I. C., Parrish, E. M., & Haugh, J. M. (2005). Spatial analysis of 3′ phosphoinositide signaling in living fibroblasts, III: Influence of cell morphology and morphological polarity. *Biophysical Journal*, *89*(2), 1420-1430.
97. Tyson, J. J., & Keener, J. P. (1988). Singular perturbation theory of traveling waves in excitable media (a review). *Physica D: Nonlinear Phenomena*, *32*(3), 327-361.
98. Park, C. S., Schneider, I. C., & Haugh, J. M. (2003). Kinetic analysis of platelet-derived growth factor receptor/phosphoinositide 3-kinase/Akt signaling in fibroblasts. *Journal of Biological Chemistry*, *278*(39), 37064-37072.
99. Gamba, A., De Candia, A., Di Talia, S., Coniglio, A., Bussolino, F., & Serini, G. (2005). Diffusion-limited phase separation in eukaryotic chemotaxis.*Proceedings of the National Academy of Sciences of the United States of America*, *102*(47), 16927-16932.
100. Naoki, H., Sakumura, Y., & Ishii, S. (2008). Stochastic control of spontaneous signal generation for gradient sensing in chemotaxis. *Journal of Theoretical Biology*, *255*(2), 259-266.
101. Turner, M. S., Trauger, J. W., Stephens, J., & LoGrasso, P. (2002). Characterization and purification of truncated human Rho-kinase II expressed in Sf-21 cells. *Archives of Biochemistry and Biophysics*, *405*(1), 13-20.
102. Sakumura, Y., Tsukada, Y., Yamamoto, N., & Ishii, S. (2005). A molecular model for axon guidance based on cross talk between rho GTPases.*Biophysical Journal*, *89*(2), 812-822.
103. Lammers, M., Meyer, S., Kühlmann, D., & Wittinghofer, A. (2008). Specificity of interactions between mDia isoforms and Rho proteins. *Journal of Biological Chemistry*, *283*(50), 35236-35246.

104. Besser, A., & Schwarz, U. S. (2007). Coupling biochemistry and mechanics in cell adhesion: a model for inhomogeneous stress fiber contraction. *New Journal of Physics*, *9*(11), 425.
105. Zeng, Y., Lai, T., Koh, C. G., LeDuc, P. R., & Chiam, K. H. (2011). Investigating circular dorsal ruffles through varying substrate stiffness and mathematical modeling. *Biophysical Journal*, 101(9), 2122-2130.
106. Keller, R. (2005). Cell migration during gastrulation. *Current Opinion in Cell Biology*, 17(5), 533-541.
107. Carman, C.V. (2009). Mechanisms for transcellular diapedesis: probing and pathfinding by 'invadosome-like protrusions'. *Journal of Cell Science*. 122, 3025–3035.
108. Martin, P. (1997). Wound healing-aiming for perfect skin regeneration. *Science*, 276(5309), 75-81.
109. Liotta, L. A., Steeg, P. S., & Stetler-Stevenson, W. G. (1991). Cancer metastasis and angiogenesis: an imbalance of positive and negative regulation. *Cell*, 64(2), 327-336.
110. Yang, J., Mani, S. A., Donaher, J. L., Ramaswamy, S., Itzykson, R. A., Come, C., & Weinberg, R. A. (2004). Twist, a master regulator of morphogenesis, plays an essential role in tumor metastasis. *Cell*, 117(7), 927-939.
111. Furuta, Y., Kanazawa, S., Takeda, N., Sobue, K., Nakatsuji, N., Nomura, S., & Tadashi Yamamoto, S. A. (1995). Reduced cell motility and enhanced focal adhesion contact formation in cells from FAK-deficient mice. *Nature*, 377(6549), 539-544.
112. Munevar, S., Wang, Y. L., & Dembo, M. (2001). Traction force microscopy of migrating normal and H-ras transformed 3T3 fibroblasts. *Biophysical Journal*, 80(4), 1744-1757.
113. Rodriguez, L. G., Wu, X., & Guan, J.-lin. (2005). Wound-healing assay. *Methods in Molecular Biology*, *294*, 23-9.
114. Zigmond, S. H., & Hirsch, J. G. (1973). Leukocyte locomotion and chemotaxis new methods for evaluation, and demonstration of a cell-derived chemotactic factor. *The Journal of experimental medicine*, 137(2), 387-410.
115. Carter, S. B. (1967). Haptotaxis and the mechanism of cell motility. *Nature*, 213, 256-260.
116. Friedl, P., & Gilmour, D. (2009). Collective cell migration in morphogenesis, regeneration and cancer. *Nature Reviews Molecular Cell Biology*, *10*(7), 445-457.
117. Abercrombie, M., Joan, E., Heaysman, M., & Pegrum, S. M. (1970). The locomotion of fibroblasts in culture: II."Ruffling". *Experimental Cell Research*, *60*(3), 437-444.

118. Gov, N. S., & Gopinathan, A. (2006). Dynamics of membranes driven by actin polymerization. *Biophysical Journal*, 90(2), 454-469.

119. Peleg, B., Disanza, A., Scita, G., & Gov, N. (2011). Propagating cell-membrane waves driven by curved activators of actin polymerization. *PloS ONE*, 6(4), e18635.

120. Wang, Y. L., & Pelham, R. J. (1998). Preparation of a flexible, porous polyacrylamide substrate for mechanical studies of cultured cells. *Methods in Enzymology*, 298, 489-496.

121. Jackson, J. D., & Fox, R. F. (1999). Classical electrodynamics. *American Journal of Physics*, *67*, 841.

122. Arfken, G. B., Weber, H. J., & Harris, F. E. (2011). *Mathematical methods for physicists: a comprehensive guide*. Academic press.

123. Koestler, S. A., Rottner, K., Lai, F., Block, J., Vinzenz, M., & Small, J. V. (2009). F-and G-actin concentrations in lamellipodia of moving cells. *PLoS ONE*,*4*(3), e4810.

124. Fan, Y., Eswarappa, S. M., Hitomi, M., & Fox, P. L. (2012). Myo1c facilitates G-actin transport to the leading edge of migrating endothelial cells. *The Journal of Cell Biology*, *198*(1), 47-55.

125. Maskarinec, S. A., Franck, C., Tirrell, D. A., & Ravichandran, G. (2009). Quantifying cellular traction forces in three dimensions. *Proceedings of the National Academy of Sciences*, 106(52), 22108-22113.

126. Thangawng, A. L., Ruoff, R. S., Swartz, M. A., & Glucksberg, M. R. (2007). An ultra-thin PDMS membrane as a bio/micro–nano interface: fabrication and characterization. *Biomedical Microdevices*, 9(4), 587-595.

127. Wong, J. Y., Velasco, A., Rajagopalan, P., & Pham, Q. (2003). Directed movement of vascular smooth muscle cells on gradient-compliant hydrogels. *Langmuir*, *19*(5), 1908-1913.

128. Peyton, S. R., Ghajar, C. M., Khatiwala, C. B., & Putnam, A. J. (2007). The emergence of ECM mechanics and cytoskeletal tension as important regulators of cell function. *Cell Biochemistry and Biophysics*, *47*(2), 300-320.

129. Chen, C. S. (2008). Mechanotransduction–a field pulling together?. *Journal of Cell Science*, *121*(20), 3285-3292.

130. Krizhanovsky, V., Yon, M., Dickins, R. A., Hearn, S., Simon, J., Miething, C., Yee, H., et al. (2008). Senescence of activated stellate cells limits liver fibrosis. *Cell*,*134*(4), 657-67.

131. Wells, R. G. (2008). The role of matrix stiffness in regulating cell behavior. *Hepatology*, *47*(4), 1394-1400.
132. Raeber, G. P., Lutolf, M. P., & Hubbell, J. A. (2005). Molecularly engineered PEG hydrogels: a novel model system for proteolytically mediated cell migration. *Biophysical Journal*, *89*(2), 1374-1388.
133. Maskarinec, S. A., & Tirrell, D. A. (2005). Protein engineering approaches to biomaterials design. *Current Opinion in Biotechnology*, *16*(4), 422-426.
134. Genzer, J., & Bhat, R. R. (2008). Surface-bound soft matter gradients. *Langmuir*, *24*(6), 2294-2317.
135. Zaari, N., Rajagopalan, P., Kim, S. K., Engler, A. J., & Wong, J. Y. (2004). Photopolymerization in microfluidic gradient generators: microscale control of substrate compliance to manipulate cell response. *Advanced Materials*, *16*(23-24), 2133-2137.
136. Gray, D. S., Tien, J., & Chen, C. S. (2003). Repositioning of cells by mechanotaxis on surfaces with micropatterned Young's modulus. *Journal of Biomedical Materials Research Part A*, *66*(3), 605-614.
137. Kloxin, A. M., Kasko, A. M., Salinas, C. N., & Anseth, K. S. (2009). Photodegradable hydrogels for dynamic tuning of physical and chemical properties. *Science*, *324*(5923), 59-63.
138. Kloxin, A. M., Benton, J. A., & Anseth, K. S. (2010). *In situ* elasticity modulation with dynamic substrates to direct cell phenotype. *Biomaterials*, *31*(1), 1-8.
139. Palchesko, R. N., Zhang, L., Sun, Y., & Feinberg, A. W. (2012). Development of Polydimethylsiloxane Substrates with Tunable Elastic Modulus to Study Cell Mechanobiology in Muscle and Nerve. *PloS ONE*, *7*(12), e51499.
140. Shield, T. W., Kim, K. S., & Shield, R. T. (1994). The buckling of an elastic layer bonded to an elastic substrate in plane strain. *Journal of Applied Mechanics*, *61*(2), 231-235.
141. Hutchinson, J. W., & Suo, Z. (1992). Mixed mode cracking in layered materials. *Advances in applied mechanics*, *29*(63), 191.
142. Yu, H. H., & Hutchinson, J. W. (2002). Influence of substrate compliance on buckling delamination of thin films. *International Journal of Fracture*, *113*(1), 39-55.

143. Yip, A. K., Iwasaki, K., Ursekar, C., Machiyama, H., Saxena, M., Chen, H., Ichiro, H., Chiam, K.-H., & Sawada, Y. (2013). Cellular Response to Substrate Rigidity Is Governed by Either Stress or Strain. *Biophysical journal*, *104*(1), 19-29.
144. Yeung, T., Georges, P. C., Flanagan, L. A., Marg, B., Ortiz, M., Funaki, M., Zahir, N., et al. (2005). Effects of substrate stiffness on cell morphology, cytoskeletal structure, and adhesion. *Cell Motility and the Cytoskeleton*, *60*(1), 24-34.
145. Chou, S. Y., Cheng, C. M., Chen, C. C., & LeDuc, P. R. (2011). Localized neurite outgrowth sensing via substrates with alternative rigidities. *Soft Matter*, 7(21), 9871-9877.